Title
Investigation of Clathrin-Mediated Endocytosis Using Genome Editing in Somatic and Pluripotent Human Cells

Author
Cheng, Aaron T

Publication Date
2013

Peer reviewed|Thesis/dissertation

Investigation of Clathrin-Mediated Endocytosis Using Genome Editing in Somatic and Pluripotent Human Cells

by

Aaron T. Cheng

A dissertation submitted in partial satisfaction of the
requirements for the degree of
Doctor of Philosophy
in
Molecular and Cell Biology
in the
Graduate Division
of the
University of California, Berkeley

Committee in charge:
Professor David G. Drubin, Chair
Professor Matthew Welch
Professor David Bilder
Professor Daniel Fletcher

Spring 2013

Investigation of Clathrin-Mediated Endocytosis
Using Genome Editing in Somatic and Pluripotent Human Cells

By

Aaron T. Cheng

ABSTRACT

Investigation of Clathrin-Mediated Endocytosis Using Genome Editing
in Somatic and Pluripotent Human Cells
by
Aaron T. Cheng
Doctor of Philosophy in Molecular and Cell Biology
University of California, Berkeley
Professor David G. Drubin, Chair

Clathrin-mediated endocytosis (CME) is the best-studied and predominant pathway by which portions of the plasma membrane and extracellular material are internalized. Traditional methods using ectopically overexpressed endocytic fluorescent protein fusions indicated that mammalian CME is a dynamic but inefficient and heterogeneous process. Here, I present three studies that utilize genome editing to probe the dynamics of endocytic proteins expressed from their endogenous loci.

First, I describe a proof-of-principle study establishing the feasibility and utility of zinc finger nucleases (ZFNs) for integration of fluorescent markers at user-specified genomic sites for the study of protein dynamics. Together with use of live-cell fluorescence microscopy, we monitored two key components of the endocytic machinery, clathrin and dynamin. Genome-edited somatic cells exhibited enhanced endocytic function, dynamics, and efficiency when compared with previously studied cells, indicating that CME is highly sensitive to protein levels. This work also establishes genome editing as a robust tool to faithfully report protein localization and dynamics.

Genome-edited cells display stable fluorescent marker integration and uniform protein fusion expression across a cell population. This allowed us to perform global analyses on live cells to probe the requirement for actin in CME. We monitored dynamin dynamics and found that, like yeast, endocytosis is highly regular at late stages despite heterogeneity in clathrin lifetime. Impairment of actin dynamics by small molecule inhibitors revealed that F-actin turnover is critical for the robust recruitment of dynamin. Additionally, dynamin recruitment is dependent on its own concentration. Together, these data more clearly define the mechanisms that underlie CME.

Previous work using somatic cell lines suggested that endocytic dynamics vary among different cell types. The ability to monitor protein fusions at endogenous levels afforded me the opportunity to establish a cell-based developmental system using human pluripotent stem cells (hPSCs) to directly probe if and how endocytic dynamics change upon cellular differentiation. I engineered hPSCs to express CLTA-RFP at endogenous levels and found that these cells displayed long-lived CLTA-RFP structures at the plasma membrane that co-localized with adhesions, implying that components of adhesion complexes and/or the actin cytoskeleton that it engages may influence clathrin dynamics. Strikingly, upon differentiation into fibroblast-like cells, CLTA-RFP behavior became highly dynamic. Collectively, these data show that endocytic dynamics can and do change upon cellular differentiation and suggest a role for endocytosis in defining cell function and fate.

TABLE OF CONTENTS

LIST OF FIGURES

LIST OF TABLES

DEDICATION

To my wife, Mariska,
my daughter, Violet,
and our dog, Summer,
for your unwavering support.
I will forever love you all.

ACKNOWLEDGEMENTS

This body of work is the culmination of the efforts of many people. Foremost, I would like to thank my advisor, David Drubin, for welcoming me into his lab, for fostering an environment conducive to originality, exploration, independence, and collegiality, and for his unwavering support. My graduate tenure has been immensely rewarding as a result and, for that, I am deeply grateful.

I would also like to thank the members of the Drubin Barnes lab for enriching my doctoral experience. Specifically, I would like to acknowledge Jeff Doyon and Jackie Cheng for allowing me to share in the adventure of genome editing. I would also like to thank Alexandre Grassart who worked intimately with me during the last few years on investigating the role of actin in endocytosis. Lastly, I would like to extend my appreciation to Yidi Sun who, as my lab baymate, has watched me (perhaps a little too closely) mature academically and who has provided much needed daily comedic interruption and constructive discussions on a variety of subjects, both academic and non-academic.

I am most indebted to my family, whom have always encouraged, challenged, and supported me to be considerate and committed in my life pursuits. Much love to my wife, Mariska, who embarked on this doctoral journey with me, and whom I am deeply happy to be alongside to share in completion of this lfie chapter.

CHAPTER 1: General Introduction

OVERVIEW

The cell is the basic structural and functional unit of all known living organisms. Separating a cell, physically, from its environment is the plasma membrane, which acts as a permeability barrier. A consequence of this barrier, however, is that for molecules too large or polar to pass directly through the hydrophobic bilayer, an active mechanism is required for their entry into the cell. Clathrin-mediated endocytosis (CME) is the best-studied and predominant pathway by which portions of the plasma membrane, along with extracellular material, are internalized (for a comprehensive review, see McMahon and Boucrot, 2011).

Life Cycle of Clathrin-mediated Endocytosis

CME occurs in all eukaryotic cells, and is characterized by the assembly of clathrin triskelia (comprised of clathrin heavy and light chains) into polygonal cages that form a coat and mediate membrane invagination (Brodsky *et al*., 2001). The pathway begins with the recruitment of FCH domain only (FCHO) proteins, EGFR pathway substrate 15 (Eps15), and intersectins to the plasma membrane and proceeds with concentration of transmembrane receptors and their bound ligands into 'coated pits' (Koh *et al.,* 2004; Stimpson *et al*., 2009; Henne *et al*., 2010). Facilitating cargo selection and clathrin assembly is the heterotetrameric adaptor protein complex AP-2 (Boll *et al*., 1996; Schmid *et al*., 2006; Traub, 2009). During late stages of membrane invagination, the multi-domain mechanochemical enzyme dynamin is recruited to the necks of pits. While the precise mechanism is still unclear, it is believed that dynamin then undergoes a GTP hydrolysis-dependent conformational change to mediate vesicle scission (Hinshaw and Schmid, 1995; Sweitzer and Hinshaw, 1998; Merrifield *et al*., 2002). Other proteins implicated in CME include, but are not limited to, AP180/CALM, epsin, cargo-selective adaptor proteins (e.g. Numb, Dab2, β-arrestins, ARH), kinases (e.g. AAK1), and actin/actin-binding partners (Ford *et al*., 2002; Santolini *et al*., 2000; Eden *et al*., 2007; Santini *et al*., 2002; He *et al*., 2002; Eden *et al*., 2002; Conner *et al*., 2002; Kaksonen *et al*., 2006).

Dynamics of Clathrin-mediated Endocytosis

Through use of GFP (as well as other fluorescent proteins) and live-cell microscopy, the endocytosis field has made tremendous progress toward elucidating the mechanisms that govern clathrin-coated pit initiation, maturation, and vesicle scission. In 1980, John Heuser was one of the earliest to propose, using thin-section electron micrographs of fibroblasts, that clathrin-coated vesicles form from an ordered sequence of events that begins with small, membrane buds and proceeds through large, deeply invaginated clathrin-coated pits (Heuser, 1980). While the method hinted at the dynamic nature of the endocytic pathway, it provided only snapshots of the process, and could not resolve highly transient steps of vesicle creation and scission. It would take another two decades before the first glimpse of assembling clathrin-coated structures, in cells expressing clathrin light chain fused to GFP, was made (Gaidarov *et al*., 1999). The use of total internal fluorescence (TIRF) microscopy, a powerful

approach that is naturally suited to observe fluorescent events at the cell-coverslip interface, has allowed for direct observation of the assembly and departure of fluorescently-labeled clathrin from the membrane (Merrifield, 2002). This technique has also revealed that clathrin internalization occurs immediately after a burst of dynamin recruitment and is accompanied by actin assembly (Merrifield, 2002).

A substantial body of work has documented a large degree of heterogeneity in the lifetime, size, and behavior of CME events in mammalian cells (Gaidarov *et al*., 1999; Ehrlich *et* al., 2004; Merrifield et al., 2002, 2005; Rappoport *et al*., 2006; Saffarian *et al*., 2009). Clathrin lifetime appears to correlate proportionally with cargo-receptor occupancy and particle size, suggesting that coated pits collapse unless stabilized by cargo capture (Ehrlich *et al*., 2004). Statistical analyses of clathrin lifetimes, moreover, have been used to argue that the majority of endocytic events are abortive (i.e., clathrin assemblies that fail to bud), but direct evidence supporting such inefficiency is lacking. Rather, in budding yeast, nearly all endocytic sites proceed to completion (Kaksonen, 2003). Many groups have also observed wide variance in the size of clathrin-GFP fluorescence. Clathrin-GFP presents as diffraction-limited punctae, corresponding to single clathrin-coated pits (CCPs), or larger structures (termed clathrin-coated structures (CCSs)), that are likely aggregates of CCPs or flat clathrin lattices, the distribution and frequency of which varies among different cell lines (Gaidarov *et al*., 1999; Ehrlich *et* al., 2004; Merrifield et al., 2002, 2005; Rappoport *et al*., 2006; Saffarian *et al*., 2009). Why different 'classes' of clathrin-mediated events exist is to date still unknown.

Current Methods for Live-Cell Study of Protein Dynamics

Current methods expressing tagged genes for live-cell studies in mammalian cells are largely unchanged from those first used nearly two decades ago, which dictate that fluorescent protein fusions be overexpressed from exogenously introduced transgenes (Chalfie *et al*., 1994; Inouye and Tsuji, 1994; Stearns, 1995; Pines, 1995). This method presents several critical challenges, however, as it (1) fails to preserve protein expression at native levels, which can result in protein mis-localization, aggregation, and altered signaling, and (2) forces overexpression of a single protein isoform, which can result in unintended down-regulation of related proteins (Ward *et al*., 1995; Jensen *et al*., 1995; Miyama *et al*., 1999; Luo *et al*., 2001; Kuma *et al*., 2007; Ferguson *et al*., 2008; Knoops *et al*., 2008; Liu *et* al., 2009). Chapter 2 describes a study in which we implement genome editing technology to overcome these challenges and, by comparing genome-edited cells to cells stably overexpressing transgenes, directly test the effect of protein overexpression on endocytic function.

Genome Editing with Zinc Finger Nucleases

Zinc finger nucleases are designed, sequence-specific endonucleases that can be customized to cleave a user-chosen DNA target with high specificity (for a comprehensive review, see Urnov *et al*., 2010). This engineered endonuclease combines the DNA-binding domain of transcription factors – zinc finger proteins – with the nuclease domain of the *FokI* restriction enzyme to confer DNA binding and cleaving abilities, respectively. ZFN recognition of sites dictated by the fingers and subsequent

nuclease activity creates a DNA double-stranded break (Urnov *et al*., 2005; Carroll, 2008). It is this event that is harnessed to mediate genome editing. By co-delivering ZFNs with a donor DNA bearing homology to the target region, exogenous sequences can be inserted at or near the ZFN cleavage site by homology-directed repair. To date, genome editing technology has been successfully applied to a multitude of organisms and cell types including zebrafish, plants, rats, and embryonic stem cells, for both editing of actively expressed and non-expressed genes (Lombardo *et al*., 2007; Doyon *et al*., 2008; Shukla *et al.,* 2009; Geurts *et al*., 2009; Hockemeyer *et al*., 2009). In this dissertation, I use ZFN-mediated genome editing to study aspects of the endocytic pathway that were previously intractable to investigation.

Actin and Clathrin-mediated Endocytosis

Studies of endocytic dynamics found that the majority (~80%) of clathrin-coated invaginations coincided with the recruitment of actin and proteins involved in actin polymerization (e.g., N-WASP, cortactin, Arp2/3)(Merrifield *et al.,* 2002, Merrifield *et al*., 2004 and Yarar *et al.,* 2005; Benesch et al., 2005). Functional studies revealed roles for actin polymerization in clathrin-mediated endocytosis by using the G-actin-sequestering drug latrunculin, including clathrin-coated pit formation, disappearance, merging, and splitting (Blanpied *et* al., 2002; Merrifield et al., 2005, Moskowitz et al., 2003 and Yarar et al., 2005). Discovery of huntingtin interacting protein 1R (Hip1R), a protein linking clathrin directly with F-actin, provided further evidence supporting actin's participation in CME. Knockdown of Hip1R expression by siRNA led to a reduction in CME efficiency and the stable association between the endocytic and actin machineries (Engqvist-Goldstein *et al*., 2004). From these observations, and from studies in budding yeast, which established an unequivocal requirement for actin in endocytosis, it has been proposed that actin aids endocytic internalization and coat disassembly (Kaksonen *et al*., 2003). Indeed, analysis of fibroblasts derived from conditional knockout mice and that lack dynamin showed that actin assembles at the base of arrested endocytic clathrin-coated pits, where it supports growth of long tubular necks (Ferguson *et al*., 2009). Nevertheless, detractors argue that actin polymerization may be induced only under artificially forced conditions (Boulant *et al*., 2011). Most recently, Merrifield and colleagues showed that actin serves as a dynamic scaffold that concentrates dynamin at sites of scission, and that dynamin in turn, can control its own recruitment to scission sites by modulating the kinetics of actin (Taylor *et al*., 2012). Chapter 3 describes a study that uses genome-edited cells, expressing fluorescent protein fusions of endocytic components and actin machinery, to further dissect the mechanisms that underlie the interdependency between actin and dynamin in CME.

Malignant Cell Lines and Human Pluripotent Stem Cells

Much of our knowledge about CME dynamics has relied on the use of malignant cell lines for live-cell studies (Gaidarov *et al.,* 1999; Merrifield *et al.,* 2002; Ehrlich *et al.,* 2004; Saffarian *et al*., 2009, Liu *et al*., 2009). These include cell lines that are viral-transformed, cancerous, and/or aneuploid. For example, the most widely used cell line for studies of CME, BSC-1, carries an average of 60 chromosomes, with 3 copies of

clathrin and dynamin genes (Merrifield *et al*., 2005; Loerke *et al*., 2009; Saffarian *et al*., 2009; Liu *et al*., 2009; Nunez *et al.,* 2011; Doyon *et al*., 2011). Since the effect of these malignancies on the function and regulation of CME remains unclear and because defects in endocytosis have also been linked to human disease, including cancer, myopathies, neuropathies, and metabolic and genetic syndromes, continued use of diseased cell lines limits our ability to fully and faithfully understand CME (Attree *et al.,* 1999; Zuchner *et al*., 2005; Pennington *et al*., 2007; Dalgliesh *et al*., 2010).

In contrast, human pluripotent stem cells (hPSCs) possess normal karyotype and are unique in their inexhaustible ability to divide and renew, and under the appropriate conditions, differentiate and change into virtually any cell type in the body. The first hPSCs were embryonic stem cells derived from human blastocysts (Thomson *et al*., 1998). Researchers now have the ability to artificially derive pluripotent stem cells by forced expression of transcription factors (such as Oct-3/4, SOX2, c-Myc, and Klf4) in adult somatic cells (Takahashi *et al*., 2007; Yu *et al*., 2007). Because of their promise, stem cell lines have now been successfully used to derive a variety of functional cell types and tissues, to model human genetic disorders, and for use as cell therapies against human disease. Chapter 4 describes a study that harnesses the differentiating capacity of hPSCs, together with use of ZFN-mediated genome editing, to specifically address the question of how endocytosis behaves in pluripotent cells and if and how it may change upon cellular differentiation.

CHAPTER 2:
Zinc finger nuclease mediated genome editing in somatic cells reveals rapid and efficient clathrin-mediated endocytosis[1]

[1] Doyon *et al*. 2011. Rapid and efficient clathrin-mediated endocytosis revealed in genome-edited mammalian cells. *Nature Cell Biology* 13(3):331-37.

INTRODUCTION

Clathrin-mediated endocytosis (CME) is characterized by the recruitment of clathrin triskelia, composed of heavy and light chains, to the plasma membrane and their assembly into polygonal cages that mediate membrane invagination. During late stages of this process the GTPase dynamin is recruited to the necks of these invaginations, where it mediates vesicle scission and the subsequent internalization of plasma-membrane molecules, extracellular fluid and specific ligands from the environment (Merrifield *et al*., 2002; Roux *et al*., 2006; Pucadyil and Schmid, 2008). Three decades of evidence directly connect perturbation of CME to a broad range of pathophysiological outcomes, including atherosclerosis, disorders of the peripheral and central nervous system and infection by the hepatitis C virus (Goldstein & Brown, 1977; Zuchner *et al*., 2005; Moradpour *et al*., 2007).

The study of CME has been greatly advanced through the use of fluorescent fusion proteins (Brodsky *et al*., 2001). In yeast, direct genomic tagging of pairs of genes with different fluorescent tags has allowed researchers to define a very regular series of spatiotemporal events for CME in living cells (Kaksonen *et al*., 2005). Conversely, in mammalian cells these events have been described as being much more heterogeneous and inefficient, but the inability to do precise genome editing has forced researchers to rely heavily on overexpression of fusion proteins (Ehrlich *et al*., 2004; Merrifield *et al*., 2004; Soulet *et al*., 2005; Rappoport *et al*., 2006; Saffarian *et al*., 2009; Loerke *et al*., 2009). Furthermore, these fusion proteins are often derived from a different cell type or species from the cell type being studied, and encode non-native splice variants. An accurate description of endocytic dynamics is the foundation for understanding the mechanism and regulation of this crucial process. Because evidence from fields ranging from developmental and cell biology to plant physiology has shown that overexpression can result in protein mislocalization, aggregation and altered signalling, we sought to re-examine the highly dynamic process of CME using fluorescent fusion proteins expressed from their native loci (Ward *et al*., 1995; Jensen *et al*., 1995; Miyama *et al*., 1999; Luo *et al*., 2001; Kuma *et al*., 2007; Knoops *et al*., 2008).

RESULTS

ZFN-mediated editing as an efficient and accurate method for generating stable cell lines expressing fluorescent protein fusions from native loci

To engineer precise gene fusions at endogenous loci, we used zinc finger nucleases (ZFNs) designed to cleave their target genes near the stop codons (Urnov *et al*., 2010). The resulting double-strand breaks were mended by homology-directed repair using an exogenously supplied DNA donor that encodes a fluorescent tag (Figure 2.1a). In all cases, ZFNs and donor constructs were co-transfected into the cells. The high-editing efficiency and accuracy of the open reading frame (ORF) addition process, coupled with the expression of proteins bearing fluorescent markers, allowed us to obtain the desired cells simply by using fluorescence-activated cell sorting (FACS) without drug selection (Figure 2.2a and Table 2.1, top). Single-cell derived clones were then generated by limiting dilution. We found that ZFN treatment had a negligible impact on cell survival (Figure 2.2b), suggesting that the editing strategy is an ideal method for generating stable cell lines. The complete panel of cells engineered in this study is described in Table 2.2.

ZFN-mediated insertion of RFP at the *CLTA* locus in monkey cells

We designed ZFNs targeting the 3′-terminus of clathrin light chain A (CLTA; Figure 2.1a and Table 2.3) and first used them in African green monkey kidney epithelial cells (BSC-1), which have been used for many important studies of endocytic dynamics (Saffarian *et al*., 2009; Loerke *et al*., 2009; Mettlen *et al*., 2009, 2010). We generated a cell line, mkCLTA^{EN}, in which one *CLTA* allele was tagged with red fluorescent protein (RFP; Table 2.2, Figure 2.2c and Table 2.1, bottom). Genotyping and western blot analysis confirmed the accurate addition of the tag to the *CLTA* locus (Figure 2.1b, c). As expected, mkCLTA^{EN} cells demonstrated punctate plasma membrane and perinuclear CLTA–RFP distribution (Figure 2.1d and Figure 2.3a), and complete co-localization of CLTA–RFP with clathrin heavy chain (CHC; Figure 2.3b), indicating that the endogenously tagged CLTA is correctly incorporated into clathrin-coated pits (CCPs).

Genome-edited CLTA-RFP monkey cells exhibit increased CME dynamics and function relative to overexpression lines

Numerous reports have documented striking heterogeneity in the size, dynamics and productivity of CCPs, yet the nature of this heterogeneity and its functional implications have not been established (Ehrlich *et al*., 2004; Saffarian *et al*., 2009; Loerke *et al*., 2009). Because determining the time required to form coated pits and vesicles is critical for gaining a mechanistic and regulatory understanding of CME, we sought to quantitatively analyse clathrin dynamics in mkCLTA^{EN} cells using total internal reflection fluorescence (TIRF) microscopy and semi-automated particle tracking (Liu *et al*., 2008; Loerke *et al*., 2009; Mettlen *et al*., 2009, 2010). Analysis of a well-studied BSC-1-derived cell line (rCLTA^{X}, Table 2.2), which overexpresses rat brain CLTA fused to green fluorescent protein (GFP) from a randomly integrated transgene, yielded an

Figure 2.1

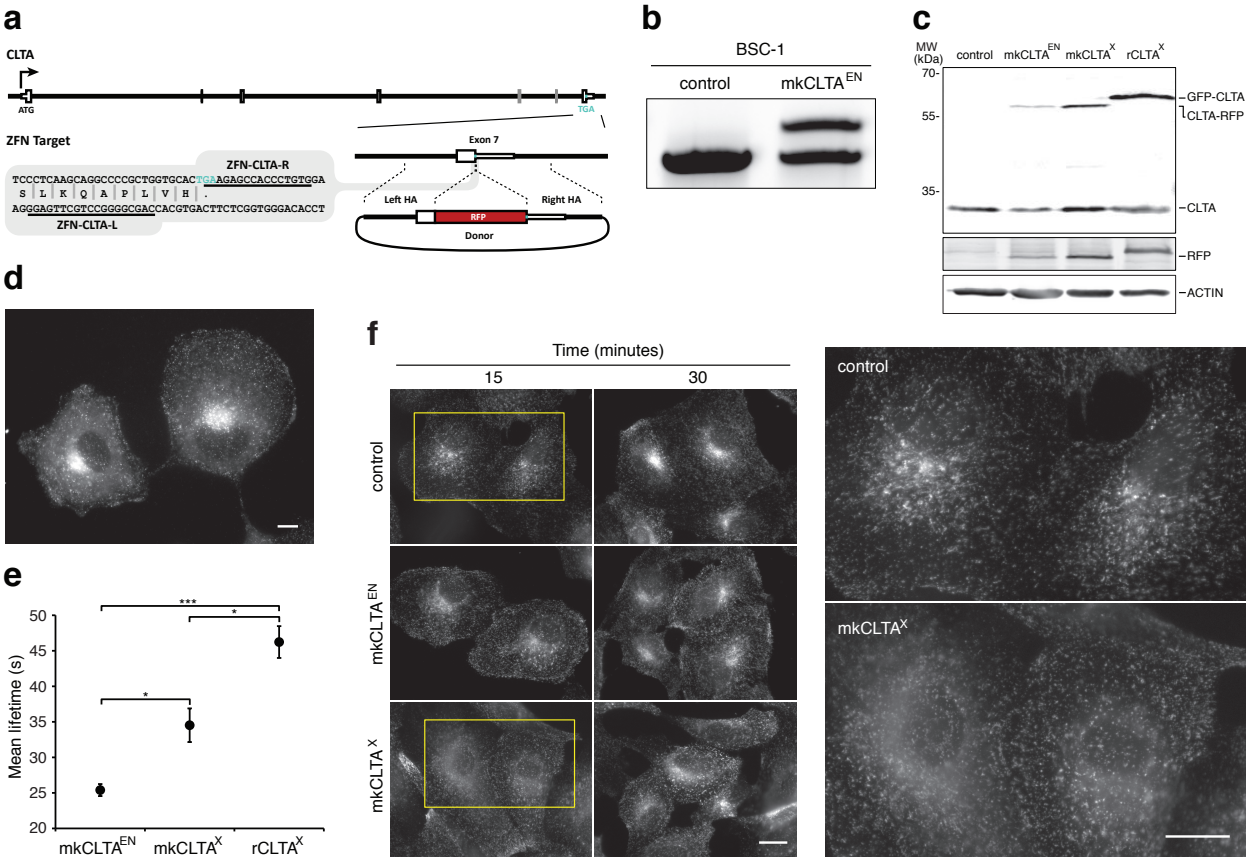

Figure 2.1 Editing of CLTA using ZFNs in BSC-1 cells. (a) Schematic overview depicting the targeting strategy for integration of RFP at the CLTA locus. White boxes, exons of CLTA. HA, donor plasmid region of homology to CLTA sequence. Blue letters, stop codon. (b) Out-out PCR showing targeted integration of RFP. Control, parental cell line; mkCLTA^{EN}, single-allele CLTA-RFP tagged genome-edited line. (c) Western blot analysis of cell lysates immunoblotted for CLTA, RFP, and actin. Note RFP antibody cross-reactivity with GFP. mkCLTA^{X}, stable CLTA-RFP overexpression line; rCLTA^{X}, stable GFP-CLTA (rat brain-derived) overexpression line. (d) Epifluorescence image of mkCLTA^{EN} expressing endogenous CLTA-RFP. Scale bar, 10 μm. (e) CCP mean lifetimes (± S.E.M.) of BSC-1 cell lines (tracks = 30,734 to 50,250; n = 5, 11, or 15 cells (mkCLTA^{X}, mkCLTA^{EN}, or rCLTA^{X}, respectively); ***P < 0.0001, *P < 0.05). (f) Time course of Alexa Fluor 488-conjugated human transferrin uptake in BSC-1 cell lines. Areas enclosed by yellow boxes are enlarged for better visualization. Scale bar, 10 μm.

Figure 2.2

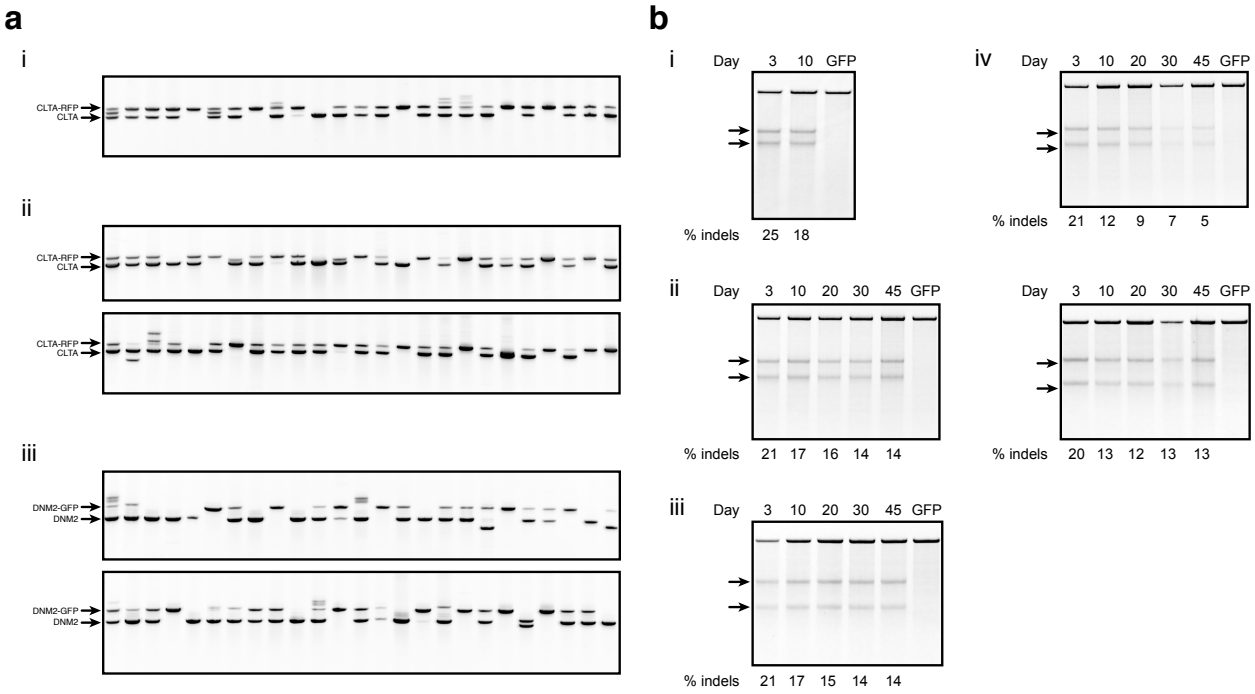
a
i
CLTA-RFP
CLTA
ii
CLTA-RFP
CLTA
CLTA-RFP
CLTA
iii
DNM2-GFP
DNM2
DNM2-GFP
DNM2
b
i
Day 3 10 GFP
% indels 25 18
ii
Day 3 10 20 30 45 GFP
% indels 21 17 16 14 14
iii
Day 3 10 20 30 45 GFP
% indels 21 17 15 14 14
iv
Day 3 10 20 30 45 GFP
% indels 21 12 9 7 5
Day 3 10 20 30 45 GFP
% indels 20 13 12 13 13

Figure 2.2 (continued)

c

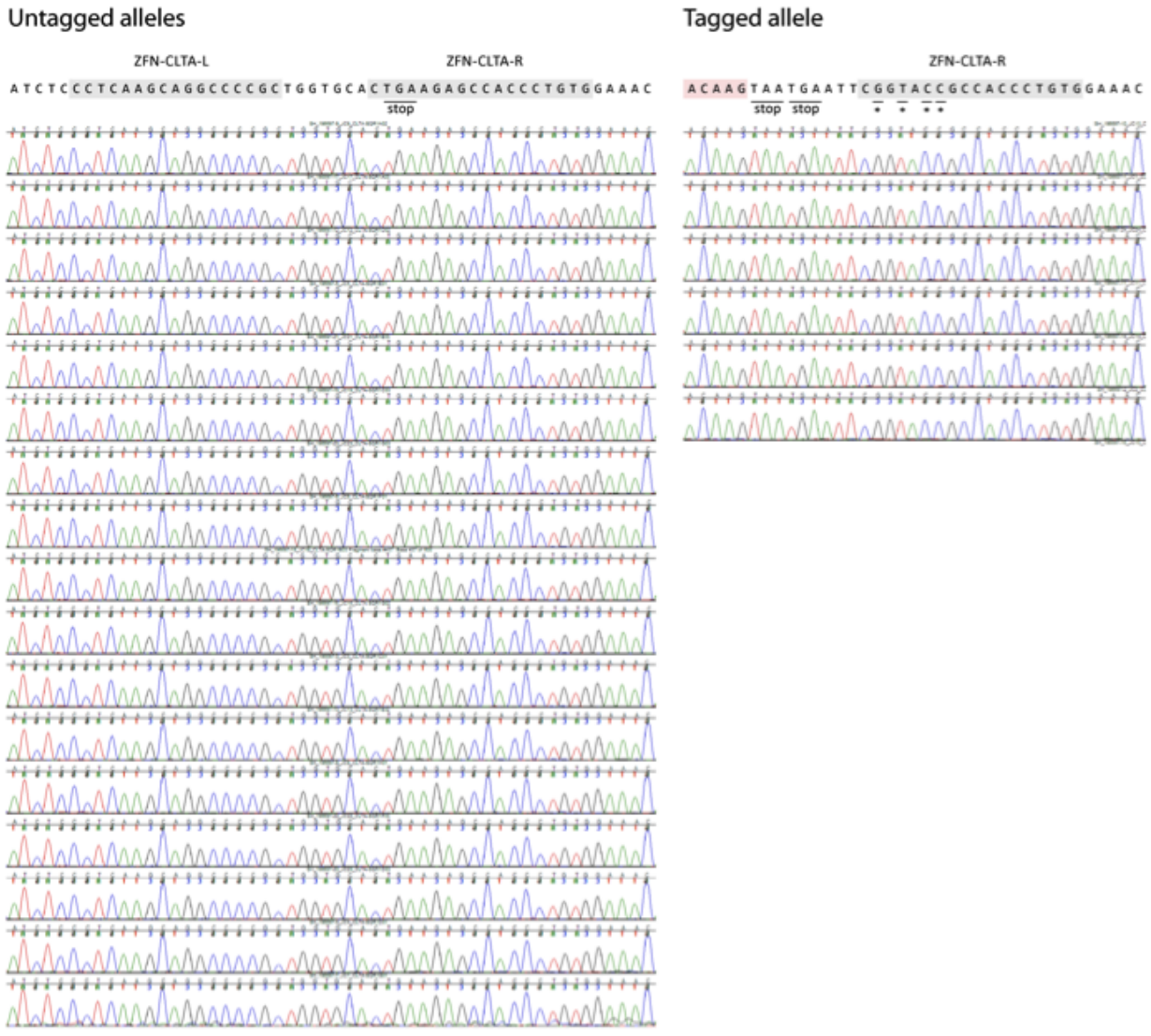

Figure 2.2 (continued)

d

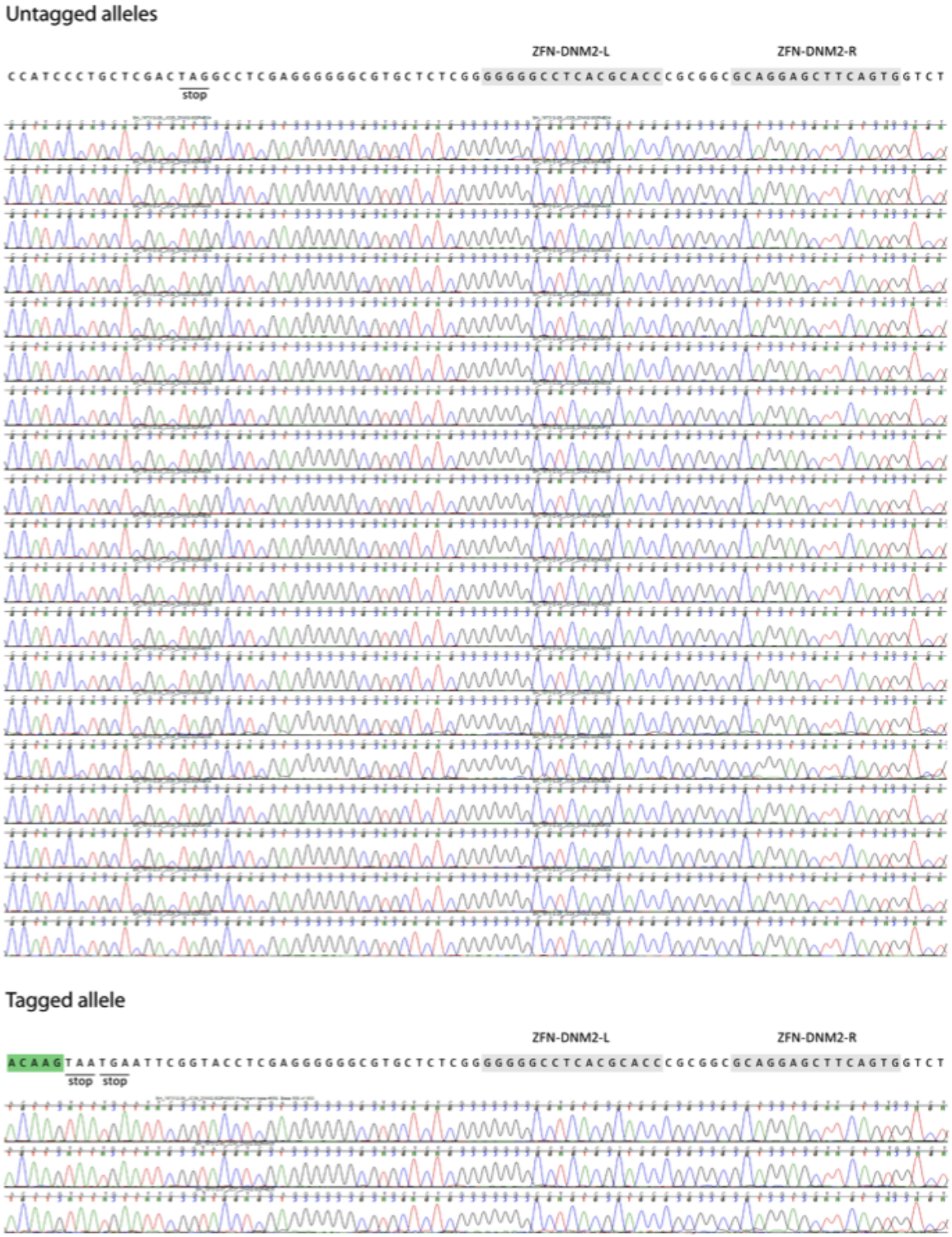

Figure 2.2 Genotypic analysis of genome-edited cell lines. (a) Representative editing efficiency using FACS enrichment. RFP-positive (i) BSC-1 or (ii and iii) SK-MEL-2 cells were enriched by FACS and individual clones were selected from colonies in 96-well plates. After ~4 weeks, clones were analyzed by out-out PCR for CLTA and DNM2 using the oligos listed in Table 2.5 as "TI." (i) 25 randomly chosen clones of the total 26, or (ii) 50 randomly chosen clones of the total 73 that were genotyped are shown. (iii) GFP-positive SK-MEL-2 clones were analyzed by out-out PCR for DNM2. (b) Stability of ZFN-modified BSC-1 and SK-MEL-2 cells. (i) BSC-1 cells were transfected with CLTA ZFNs, harvested at the indicated days post transfection, and processed for PCR and the Cel-1 cleavage assay using primers as described in Table 2.5. (ii to iv) SK-MEL-2 cells were transfected with (ii) CLTA ZFNs, (iii) DNM2 ZFNs, or (iv) both (top panel, CLTA; lower panel, DNM2), and processed similarly. GFP, ZFN transfection control. Arrows indicate the expected position of the Cel-1 cleavage products. % indels was calculated using the fraction of the cleaved signal. (c and d) Representative sequence genotyping for two genome-edited clones. (c) BSC-1 CLTA-RFP clone mkCLTA^{EN} was processed by out-out PCR (as in Fig. 2.1b) and the resulting amplicons were cloned into pCR2.1. 24 colonies were sequenced using CLTA-SQ-R (Table 2.5). Of the 23 clones that produced legible sequence, 17 perfectly matched WT CLTA near the ZFN cleavage site, and six matched the expected sequence of the RFP donor. "Stop" denotes the position of the endogenous or donor-provided stop codons. An asterisk (*) marks the location of SNPs in the ZFN-binding site of the donor. Red shading indicates the RFP coding sequence provided by the donor. (d) SK-MEL-2 DNM2-GFP clone hDNM2^{EN-1} was processed as in (c). 24 colonies were sequenced using DNM2-SQ-R (Table 2.5). Of the 22 clones that produced legible sequence, 19 perfectly matched WT DNM2 near the ZFN cleavage and donor insertion sites, and three matched the expected sequence of the GFP donor (note that the transgenic allele is a less efficient substrate both for cloning and for amplification). "Stop" denotes the position of the endogenous or donor-provided stop codons. Green shading indicates the GFP coding sequence provided by the donor.

Table 2.1

Target	Cell line	Clones genotyped	Correctly targeted clones		Imprecise or Ambiguous	Untagged
			1 or 2 copies tagged	All copies tagged		
CLTA	BSC-1	26	12 (46.2)	8 (30.8)	5 (19.2)	1 (3.8)
CLTA	SK-MEL-2	73	34 (46.6)	22 (30.1)	7 (9.6)	10 (13.7)
DNM2	SK-MEL-2	73	25 (34.2)	13 (17.8)	12 (16.4)	23 (31.5)

Designation	Clone	Cell line	Tagged Gene(s)	Topo clones sequenced	# of reads (allele)	
					untagged	tagged
mkCLTA^{EN}	26	BSC-1	CLTA	23	17 (WT)	6 (WT)
hCLTA^{EN-1}	96	SK-MEL-2	CLTA	15	11 (WT)	4 (WT)
hCLTA^{EN-all}	66	SK-MEL-2	CLTA	19	0	19 (WT)
hDNM2^{EN-1}	20	SK-MEL-2	DNM2	23	20 (WT)	3 (WT)
hDNM2^{EN-all}	95	SK-MEL-2	DNM2	24	0	31 (Δ13)*
hCLTA^{EN}/DNM2^{EN}	13	SK-MEL-2	CLTA	21	16 (WT)	5 (WT)
			DNM2	24	0	24 (+3)*

Table 2.1 Summary of genome-editing statistics. Top panel: The number of genotyped clones is given for each target in each cell type, along with the number (percentage) of correctly tagged clones having at least one (but less than all) allele tagged, or all alleles tagged. Clones that had smaller, larger, or unexpected combinations of out-out PCR products are classified as “Imprecise or Ambiguous”. Note that in all cases, cells were enriched by FACS for the cognate fluorescent marker prior to limiting dilution and genotyping. Lower panel: Summary of genotypes for genome-edited clones. Each clone was processed by out-out PCR (as in Figures 2.1b, 2.5a, 2.6b, and 2.7a), and the number of topo clones representing tagged or untagged alleles is given. The genotype of these alleles is shown in parenthesis. An asterisk (*) denotes alleles containing the indicated short insertion/deletion (number in parentheses) at the predicted cleavage site for DNM2 ZFN pair, which is located 43 bp downstream of the DNM2 stop codon in the 3’ UTR.

Table 2.2

Cell lines with marker ORFs added to the endogenous locus

Designation	Cell line	Species	Gene	Marker
mkCLTA^{EN}	BSC-1	*C. aethiops*	monkey *CLTA* (clathrin light chain A)	RFP
hCLTA^{EN}	SK-MEL-2	*H. sapiens*	human *CLTA* (clathrin light chain A)	RFP
hDNM2^{EN}	SK-MEL-2	*H. sapiens*	human *DNM2* (dynamin 2)	GFP
hCLTA^{EN}/DNM2^{EN}	SK-MEL-2	*H. sapiens*	human *CLTA*, *DNM2*	RFP/GFP

Cell lines carrying overexpressed, randomly integrated marker ORFs

Designation	Cell line	Species	Gene	Marker
rCLTA^{X}	BSC-1	*C. aethiops*	rat brain *CLTA* (clathrin light chain A)	GFP
mkCLTA^{X}	BSC-1	*C. aethiops*	monkey *CLTA* (clathrin light chain A)	RFP
hCLTA^{X}	SK-MEL-2	*H. sapiens*	human *CLTA* (clathrin light chain A)	RFP
hDNM2^{X}	SK-MEL-2	*H. sapiens*	human *DNM2* (dynamin 2)	GFP

Table 2.2 Cell lines used in this study, and their designations.

Table 2.3

Gene	ZFN Binding Sequence (underlined)	ZFN	Finger 1	Finger 2	Finger 3	Finger 4	Finger 5	Finger 6
CLTA	CCTCAAgCAGGCCCCGCTGgtgcactGAAGAGcCACCCTGTG	CLTA-R	RSDSLSV	HNDSRKN	DQSNLRA	RSANLAR	QSGNLAR	-
	GGAGTTcGTCCGGGGCGACcacgtgaCTTCTCgGTGGGACAC	CLTA-L	RSDHLSA	SYWSRTV	RSDALSV	DSSHRTR	RSDHLSE	NSRNRKT
DNM2	GGGGGCCTCaCGCACCcgcggcGCAGGAGCTTCAGTG	DNM2-R	RSDSLLR	QSADRTK	QSSDLRR	QSGHLQR	QSGDLTR	-
	CCCCCGGAGtGCGTGGgcgccgCGTCCTCGAAGTCAC	DNM2-L	DRSTLRQ	DRSDLSR	RSDNLTR	RSDDLTR	TSGHLSR	-

CLTA-R:

VPAAMAERPFQCRICMRNFS**RSDSLSV**HIRTHTGEKPFACDICGRKFA**HNDSRKN**HTKIHTGEKPFQCRICMRKFA**DQSNLRA**HTKIHTHPRAPIPKPFQCRICMRNFS**RSANLAR**HIRTHTGEKPFACDICGRKFA**QSGNLAR**HTKIHLRGS

CLTA-L:

VPAAMAERPFQCRICMRNFS**RSDHLSA**HIRTHTGEKPFACDICGRKFA**SYWSRTV**HTKIHTHPRAPIPKPFQCRICMRNFS**RSDALSV**HIRTHTGEKPFACDICGRKFA**DSSHRTR**HTKIHTGSQKPFQCRICMRNFS**RSDHLSE**HIRTHTGEKPFACDICGRKFA**NSRNRKT**HTKIHLRGS

DNM2-R:

VPAAMAERPFQCRICMRNFS**RSDSLLR**HIRTHTGEKPFACDICGRKFA**QSADRTK**HTKIHTGSQKPFQCRICMRKFA**QSSDLRR**HTKIHTGEKPFQCRICMRNFS**QSGHLQR**HIRTHTGEKPFACDICGRKFA**QSGDLTR**HTKIHLRGS

DNM2-L:

VPAAMAERPFQCRICMRKFA**DRSTLRQ**HTKIHTGEKPFQCRICMRNFS**DRSDLSR**HIRTHTGEKPFACDICGRKFA**RSDNLTR**HTKIHTHPRAPIPKPFQCRICMRNFS**RSDDLTR**HIRTHTGEKPFACDICGRKFA**TSGHLSR**HTKIHLRGS

Table 2.3 ZFN target sites and designed zinc finger helix sequences (top panel). Bases in lower-case are skipped from a DNA recognition perspective by the zinc finger proteins (ZFPs). The amino acid sequences of the ZFPs are in the bottom panel, with the recognition alpha-helices underlined.

.

Figure 2.3

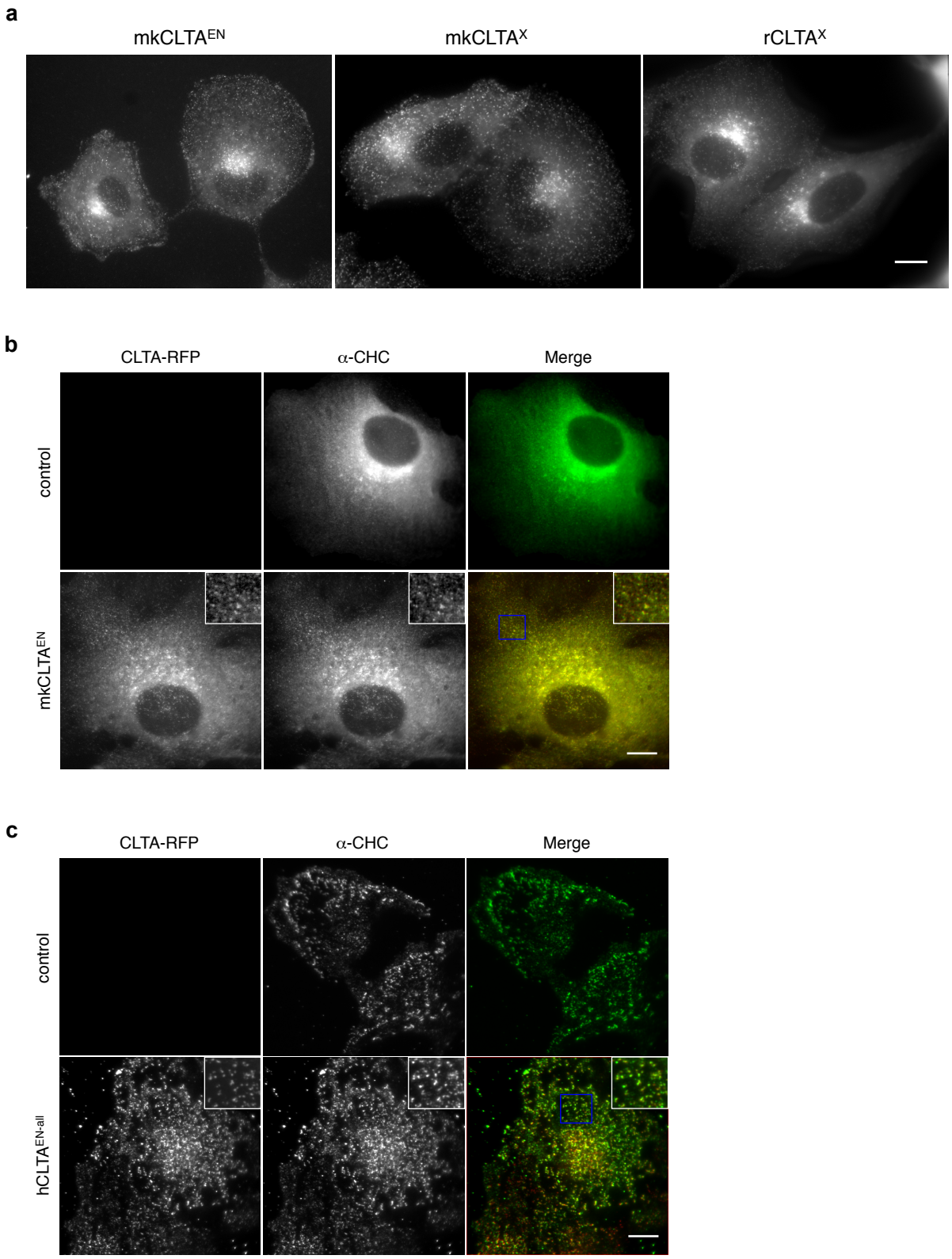
a
mkCLTA^EN
mkCLTA^X
rCLTA^X
b
CLTA-RFP
α-CHC
Merge
control
mkCLTA^EN
c
CLTA-RFP
α-CHC
Merge
control
hCLTA^EN-all

Figure 2.3 Fluorescence microscopy analysis of genome-edited cell lines. (a) Epifluorescence images of BSC-1 cell lines. mkCLTA^{EN}, single-allele tagged CLTA-RFP genome-edited cell line; mkCLTA^{X}, stable CLTA-RFP (monkey-derived) overexpression cell line; rCLTA^{X}, stable GFP-CLTA (rat brain-derived) overexpression cell line. Scale bar, 10 μm. (b and c) Immunostaining analysis of genome edited cell lines. Fixed (b) BSC-1 mkCLTA^{EN} and (c) SK-MEL-2 hCLTA$^{EN\text{-}all}$ cell lines were stained for clathrin heavy chain (CHC) and visualized by epi-fluorescence and TIRF microscopy, respectively. Scale bar, 10 μm.

overall mean lifetime for the fusion protein at the plasma membrane of 46 ± 2.2 s (Figure 2.1e, Figure 2.4a, and Table 2.4), similar to previously reported values of 39 and 46 s (Ehrlich *et al*., 2004; Loerke *et al*., 2009). Strikingly, analysis of the endogenously tagged mkCLTA^{EN} cell line revealed a significantly shorter mean lifetime (25 ± 0.9 s, $P <$ 0.0001; Figure 2.1e, Figure 2.4a, and Table 2.4).

Our single-allele tagged, genome-edited cell lines exhibited considerably dimmer fluorescent structures than the stable overexpression cell lines. As such, we were concerned that this decreased fluorescence might affect our ability to faithfully quantify endocytic protein dynamics. To address this concern, we conducted two tests of the effects of low fluorescence signal on our lifetime measurements. First, we determined whether the measured lifetime for an overexpression line is affected by decreasing the exposure time. Whether the rCLTA^{X} cell line was analyzed with an exposure time of 900 ms (as used in this study) or 30 ms (to simulate low fluorescence), similar mean lifetimes of 46 ± 2.2 s and 51 ± 6.3 s, respectively, were obtained. Second, we predicted that if we are faithfully measuring the lifetimes of low-fluorescence structures in the single-allele edited lines, then their arrival and disappearance at individual endocytic sites should be coincident with those of the same protein fused to a different tag, and expressed in the same cell. Indeed, when we transiently overexpressed human CLTA fused to GFP in the hCLTA^{EN-1} cell line (expressing CLTA–RFP), we found that, despite the low fluorescence of the endogenous CLTA–RFP, its arrival and disappearance were coincident with those of CLTA–GFP (data not shown). These data collectively demonstrate that the observed shorter mean lifetimes of our single-allele genome-edited lines, compared with all-allele edited and overexpression lines, were not the result of a decreased ability to detect clathrin for its entire membrane lifetime.

To address whether the species (rat versus monkey) and splice variant of rCLTA^{X} could account for the discrepancy in CCP lifetimes, we generated a stable overexpression BSC-1 cell line (mkCLTA^{X}; Table 2.2) in which the major endogenously expressed mkCLTA splice variant was fused to RFP. Relative to the endogenously tagged mkCLTA^{EN} cell line, CLTA was overexpressed 3.5-fold in mkCLTA^{X} and 5.7-fold in rCLTA^{X} cells (Figure 2.1c). mkCLTA^{X} cells had an average CLTA–RFP lifetime of 35 ± 2.4 s—a value significantly longer than that of the mkCLTA^{EN} line ($P < 0.05$; Figure 2.1e, Figure 2.4a, Table 2.4)—indicating that protein overexpression increases CCP lifetime. Moreover, mkCLTA^{EN} cells showed robust uptake of transferrin (a CME cargo), similar to that of control cells, with intense perinuclear accumulation. By contrast, the transferrin distribution was more diffuse in mkCLTA^{X} cells, suggesting a diminished rate of internalization (Figure 2.1f). These results indicate that overexpression of CLTA can also negatively impact endocytic function and are consistent with previous studies implicating clathrin light chains as negative regulators of CME (Brodsky *et al*., 2001; Huang *et al*., 2004; Mettlen *et al*., 2009). Collectively, these findings demonstrate a more faithful representation of CME than was achieved using previous methods requiring overexpression and highlight the importance of studying the dynamics of proteins at physiological expression levels.

Figure 2.4

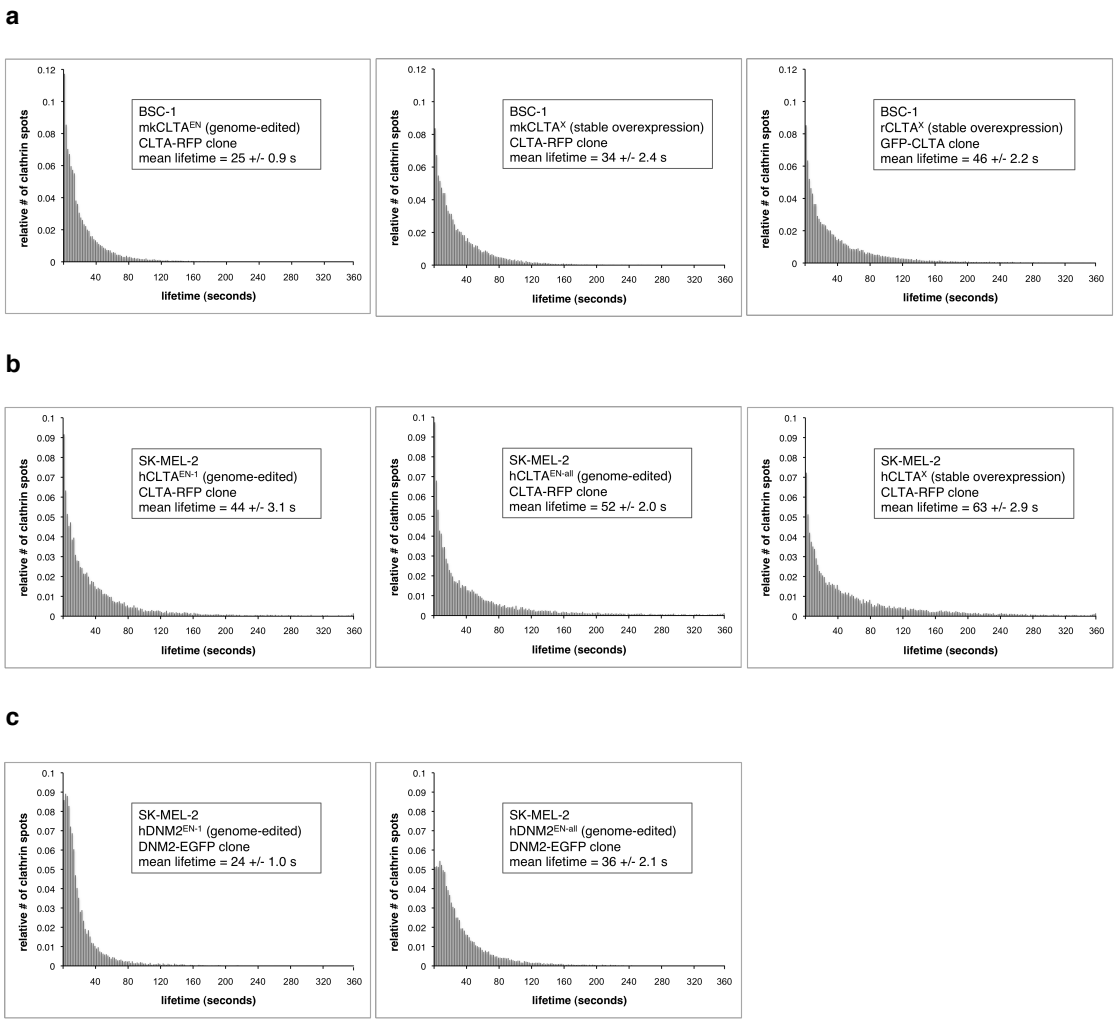

Figure 2.4 Endocytic protein lifetime distribution of genome-edited cell lines. Lifetime distribution for endocytic proteins was determined by the elapsed time between the appearance and disappearance of fluorescent structures present in the time series (6 min) from TIRF microscopy time-lapse videos of (a) BSC-1, (b) SK-MEL-2 CLTA-RFP and (c) SK-MEL-2 DNM2-GFP cell lines. Exposure time: 900 ms; Acquisition: 2 s/frame.

Table 2.4

BSC-1

Designation	Description	Lifetime (seconds) mean	25th percentile	median	75th percentile	% > 358	SD	SEM	n = # tracks; k = # cells
rCLTA^{X}	GFP-CLTA stable overexpression (rat brain)	46.2	10	26	60	0.74	8.68	2.24	n=32,366 k=15
mkCLTA^{EN}	Clone 26 - genome-edited CLTA-RFP (african green monkey kidney)	25.4	6	14	32	0.03	2.81	0.85	n=50,250 k=11
mkCLTA^{X}	Clone OE 89 - stable overexpression CLTA-RFP (african green monkey kidney)	34.5	8	22	46	0.18	5.30	2.37	n=30,734 k=5

SK-MEL-2

Designation	Description	Lifetime (seconds) mean	25th percentile	median	75th percentile	% > 358	SD	SEM	n = # tracks; k = # cells
hCLTA^{EN-1}	Clone 96 - genome-edited CLTA-RFP (human skin)	43.8	8	24	54	1.45	8.77	3.10	n=14,868 k=8
hCLTA^{EN-all}	Clone 66 - genome-edited CLTA-RFP (human skin)	52.1	8	24	68	3.81	7.27	2.02	n=19,525 k=13
hCLTA^{X}	Clone OE 20 - stable overexpression CLTA-RFP (human skin)	62.9	12	36	86	3.86	9.54	2.88	n=19,190 k=11
hDNM2^{EN-1}	Clone 20 - genome-edited DNM2-EGFP (human skin)	23.8	6	14	28	0.06	3.29	1.04	n=14,726 k=10
hDNM2^{EN-all}	Clone 95 - genome-edited DNM2-EGFP (human skin)	36.3	10	22	46	0.14	7.60	2.11	n=29,681 k=13
hCLTA^{EN}/DNM2^{EN}	Clone 13 - genome-edited CLTA-RFP (human skin)	44.5	8	26	64	0.75	2.42	0.99	n=6,799 k=6
	Clone 13 - genome-edited DNM2-EGFP (human skin)	31.5	10	22	40	0.03	7.28	3.26	n=3,944 k=5

Table 2.4 Lifetime analysis of endocytic proteins in various cell lines.

Genome-edited CLTA-RFP human cells exhibit increased CME dynamics and function

To test the generality of these results, we used the same ZFN pair to generate a human skin melanoma cell line, SK-MEL-2, in which *CLTA* was tagged with RFP at its native locus. Genotyping and western blot analysis confirmed the precise addition of the tag to the *CLTA* locus, yielding both single-allele tagged ($hCLTA^{EN-1}$) and all-allele tagged ($hCLTA^{EN-all}$) cell lines (Figure 2.5a, b and Table 2.2). Importantly, $hCLTA^{EN-all}$ cells showed complete co-localization of CLTA–RFP with CHC (Figure 2.3c). Analysis of $hCLTA^{EN-1}$ revealed a mean CLTA–RFP lifetime (44 ± 3.1 s) that was significantly shorter than the lifetime in a cell line overexpressing the same CLTA–RFP fusion ($hCLTA^{X}$; 63 ± 2.9 s, $P < 0.001$; Figure 2.5c, Figure 2.4b, Table 2.4). Notably, analysis of the homozygous $hCLTA^{EN-all}$ cell line revealed large, stable clathrin-coated structures at the plasma membrane that were not seen in the isogenic heterozygous line. We also observed diffraction-limited CCPs in $hCLTA^{EN-all}$ cells, and their analysis yielded an intermediate CLTA–RFP mean lifetime of 52 ± 2.0 s (Figure 2.5c, Figure 2.4b, Table 2.4). Finally, we found that $hCLTA^{EN}$ cells maintain robust transferrin uptake, similar to control cells, whereas the overexpression $hCLTA^{X}$ cell line exhibited diminished endocytic function (Figure 2.5d, e). Taken together, our data from isogenic cells in two different species support two major conclusions: CME in mammalian cells is a significantly more dynamic process than previously thought, and increasing fusion protein levels has a detrimental effect on CCP dynamics and endocytic function.

ZFN-mediated insertion of GFP at the *DNM2* locus in human cells reveals unprecedented dynamics

We next sought to address whether overexpression might affect the native dynamics of another CME factor, dynamin-2 (DNM2). Previous studies on the dynamics of dynamin fluorescent protein fusions required examination of cells with a low level of overexpression, shortly after transfection (14–16 h), because high levels of overexpression at longer intervals resulted in the appearance of large, stationary structures (Ehrlich *et al*., 2004; Liu *et al*., 2008). We created SK-MEL-2 cell lines in which one ($hDNM2^{EN-1}$) or all ($hDNM2^{EN-all}$) endogenous *DNM2* alleles were tagged with GFP (Figure 2.6a, Table 2.2 and Figure 2.2a, d) and compared them with a cell line overexpressing the identical DNM2–GFP fusion that was generated from a randomly integrated transgene ($hDNM2^{X}$; Table 2.2). The $hDNM2^{EN}$ lines were shown by genotyping and phenotypic analysis to express physiological levels of fusion protein (Figure 2.6b, c) that localized as punctate structures on the plasma membrane (Figure 2.6d).

Consistent with previous reports, our attempts to generate stable overexpression $hDNM2^{X}$ cell lines by random transgene insertion resulted in cells that exhibited bright, irregular and highly stable dynamin structures (Ehrlich *et al*., 2004; Liu *et al*., 2008). This made it impossible, as previously reported, to implement a global and unbiased analysis of DNM2 plasma membrane dynamics in these lines (Ehrlich *et al*., 2004; Liu *et al*., 2008; Loerke *et al*., 2009; Mettlen *et al*., 2010). In striking contrast, the genome-edited lines exhibited highly dynamic DNM2–GFP localization, allowing us to globally quantify

Figure 2.5

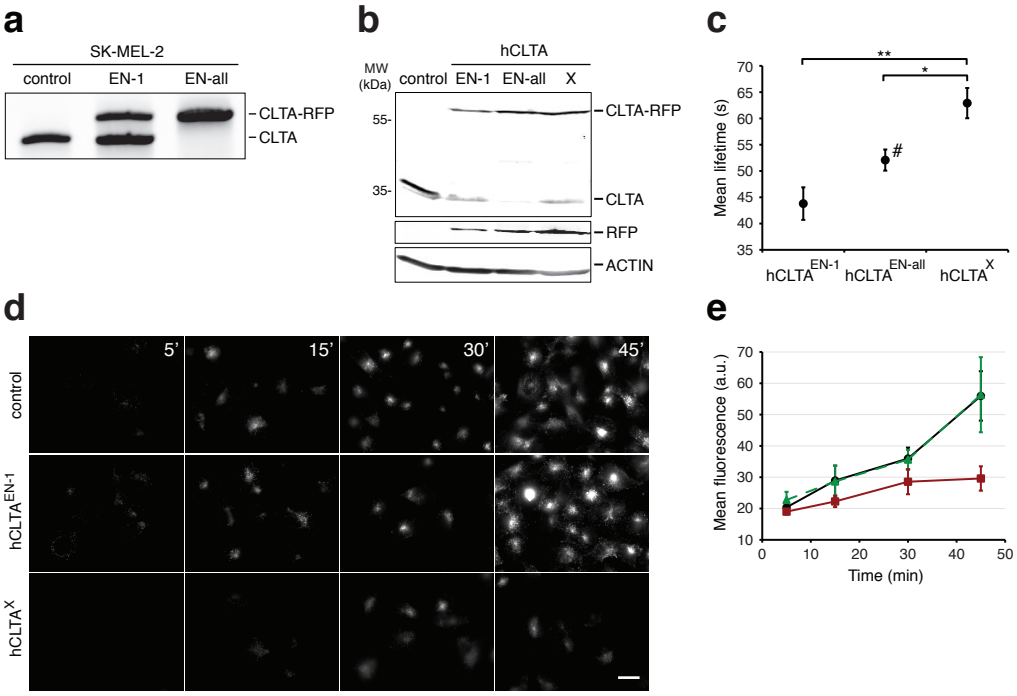

Figure 2.5 Editing of CLTA using ZFNs in SK-MEL-2 cells. (a) Out-out PCR showing targeted integration of RFP. Control, parental cell line; hCLTA^{EN-1}, single-allele CLTA-RFP tagged genome-edited line; hCLTA^{EN-all}, all-allele tagged genome-edited line. (b) Western blot analysis of cell lysates immunoblotted for CLTA, RFP, and actin. hCLTA^{X}, stable CLTA-RFP overexpression line. (c) CCP mean lifetimes (± S.E.M.) of CLTA-RFP cell lines (tracks = 14,868 to 19,525; n = 8, 13, or 11 cells (hCLTA^{EN-1}, hCLTA^{EN-all}, or hCLTA^{X}, respectively); **P < 0.001, *P < 0.05). A number sign (#) denotes analysis of diffraction-limited CCPs only, despite the presence of larger, stable clathrin structures. (d and e) Time course of Alexa Fluor 488-conjugated human transferrin uptake in SK-MEL-2 cell lines. Scale bar, 10 μm. (e) Quantification of the mean (± S.D.) cell fluorescence of hCLTA^{EN-1} cells (green curve; n = 40) as compared to parental (black curve; n = 45) and hCLTA^{X} (red curve; n = 21) cell lines.

Figure 2.6

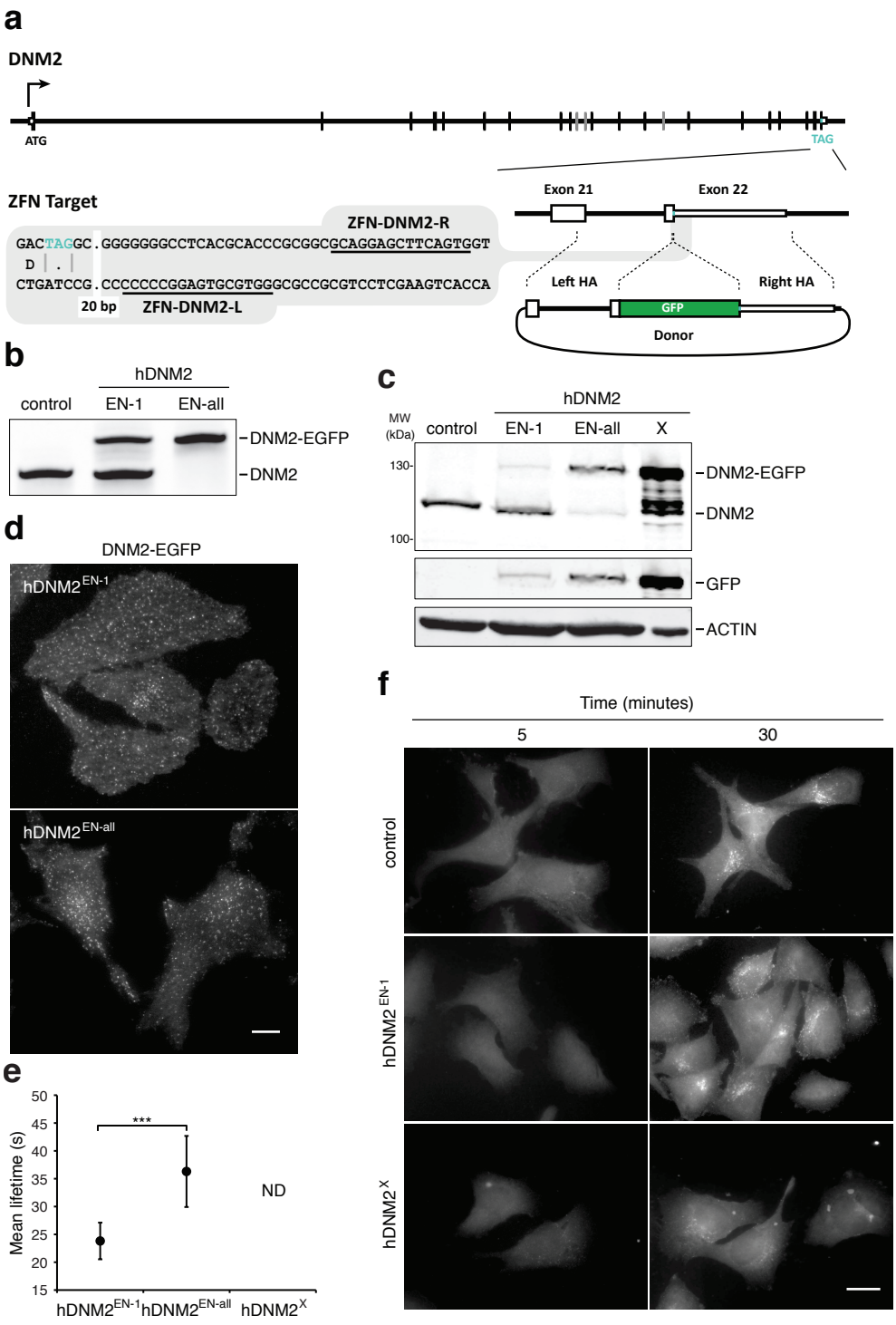
a
DNM2
ATG
TAG
ZFN Target
ZFN-DNM2-R
GACTAGGC.GGGGGGGCCTCACGCACCCGCGGCGCAGGAGCTTCAGTGGT
D
CTGATCCG.CCCCCCCGGAGTGCGTGGGCGCCGCGTCCTCGAAGTCACCA
20 bp
ZFN-DNM2-L
Exon 21
Exon 22
Left HA
Right HA
GFP
Donor
b
hDNM2
control
EN-1
EN-all
DNM2-EGFP
DNM2
c
hDNM2
MW (kDa)
control
EN-1
EN-all
X
130-
100-
DNM2-EGFP
DNM2
GFP
ACTIN
d
DNM2-EGFP
hDNM2EN-1
hDNM2EN-all
e
Mean lifetime (s)
50
45
40
35
30
25
20
15
***
ND
hDNM2EN-1
hDNM2EN-all
hDNM2X
f
Time (minutes)
5
30
control
hDNM2EN-1
hDNM2X

Figure 2.6 Editing of DNM2 using ZFNs in SK-MEL-2 cells. (a) Schematic overview depicting the targeting strategy for integration of EGFP at the DNM2 locus. (b) Out-out PCR showing targeted integration of EGFP. Control, parental cell line; $hDNM2^{EN-1}$, single-allele tagged genome-edited line; $hDNM2^{EN-all}$, all-allele tagged genome-edited line. (c) Western blot analysis of cell lysates immunoblotted for DNM2, GFP, or actin. $hDNM2^{X}$, stable overexpression DNM2-EGFP cell line. (d) TIRF microscopy images of genome-edited $hDNM2^{EN}$ cell lines expressing DNM2-EGFP. Scale bar, 10 μm. (e) DNM2-EGFP mean lifetimes (± S.E.M.) of SK-MEL-2 cell lines (tracks = 14,726 or 29,681; n = 10 or 13 cells ($hDNM2^{EN-1}$ or $hDNM2^{EN-all}$, respectively); ***$P < 0.0001$). Not determined (ND) denotes an inability to perform lifetime analysis due to the presence of stable, non-diffraction limited dynamin structures. (f) Time course of Texas Red-conjugated human transferrin uptake in SK-MEL-2 cell lines. Scale bar, 10 μm.

their lifetimes. The single-allele-tagged hDNM2^{EN-1} cell line exhibited significantly shorter average lifetimes than isogenic hDNM2^{EN-all} cells: 24 ± 1.0 s versus 36 ± 2.1 s ($P < 0.0001$; Figure 2.6e, Table 2.4). Furthermore, hDNM2^{X}-overexpressing cells had diminished endocytic function when compared with the endogenously tagged cell lines (Figure 2.6f). Thus, similarly to CLTA, DNM2 dynamics and function are highly sensitive to protein expression level and tagging.

Simultaneous tagging of *CLTA* and *DNM2* reveals that mammalian CME is highly efficient

In budding yeast, direct genomic tagging of pairs of genes encoding endocytic proteins with different fluorescent tags has implicated > 60 proteins in CME and has allowed researchers to define, in detail, a very regular series of spatiotemporal events (Kaksonen *et al.*, 2005). To generate mammalian cells possessing tagged forms of CLTA and DNM2 in a single cell, we co-delivered ZFNs and donors for both *CLTA* and *DNM2* and used FACS to isolate a pool of double-marker-positive cells. We isolated a single-cell-derived clone with one copy of *CLTA* tagged with RFP and all copies of *DNM2* tagged with GFP (hCLTA^{EN}/DNM2^{EN}; Figure 2.7a, b, Table 2.2). To our knowledge, this represents the first example in human somatic cell genetics of a cell carrying tags at two distinct endogenous non-allelic loci. Similarly to the individually tagged cell lines (Table 2.4), the measured lifetimes of CLTA and DNM2 in this dual-tagged cell line were 45 ± 1.0 s and 32 ± 3.3 s, respectively. As expected, DNM2 was robustly recruited to clathrin-intense plasma membrane puncta in the final moments of CCP maturation (Figure 2.8a, b) (Merrifield *et al.*, 2002).

Clathrin-coated structures have been classified as either abortive, in which clathrin assembly does not lead to an endocytic event, or productive, in which clathrin assembly leads to scission and internalization. Previous efforts to define the percentage of productive clathrin-coated structures have relied on inference-based statistical analysis of population lifetimes in several overexpression cell lines, yielding CME efficiency estimates of 40% (Loerke *et al.*, 2009; Mettlen *et al.*, 2009, 2010). As dynamin is required for clathrin-coated vesicle scission at the plasma membrane, the hCLTA^{EN}/DNM2^{EN} line allowed us to monitor clathrin and dynamin dynamics simultaneously in a global and unbiased manner and to use dynamin as a marker to directly measure CCP productivity. To our surprise, 91% (n = 276 CCPs) of disappearing clathrin puncta in our genome-edited cells displayed bright peaks of dynamin recruitment, suggesting that most CME events are productive (Figure 2.8c, left panel). By contrast, cells overexpressing both CLTA–RFP and DNM2–GFP displayed extensive, large stationary dynamin-containing clathrin-coated structures (Figure 2.8c, right panel). This result suggests that CME efficiency in mammals and yeast is more similar than was previously appreciated.

Figure 2.7

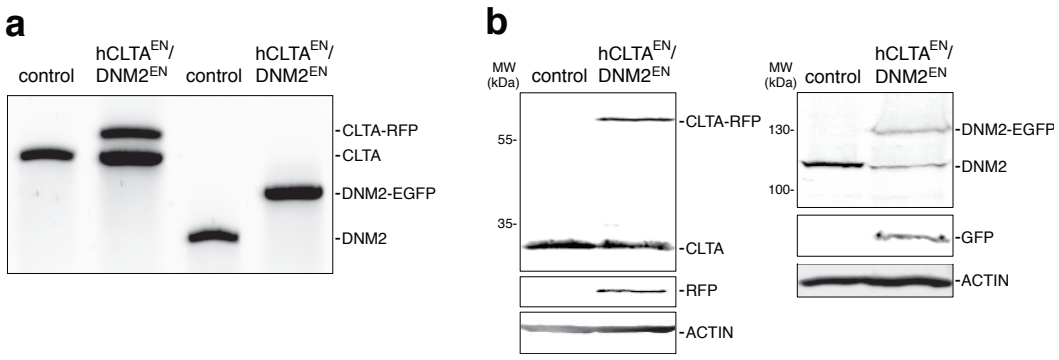

Figure 2.7 Simultaneous editing of both CLTA and DNM2 using ZFNs in SK-MEL-2 cells. (a) Out-out PCR showing targeted integration of RFP and EGFP into CLTA and DNM2 loci, respectively. Control, parental cell line; hCLTA^{EN}/hDNM2^{EN}, single-allele tagged CLTA-RFP and all-allele tagged DNM2-GFP genome-edited line. (b) Western blot analysis of cell lysates immunoblotted for CLTA, DNM2, GFP, RFP, or actin.

Figure 2.8

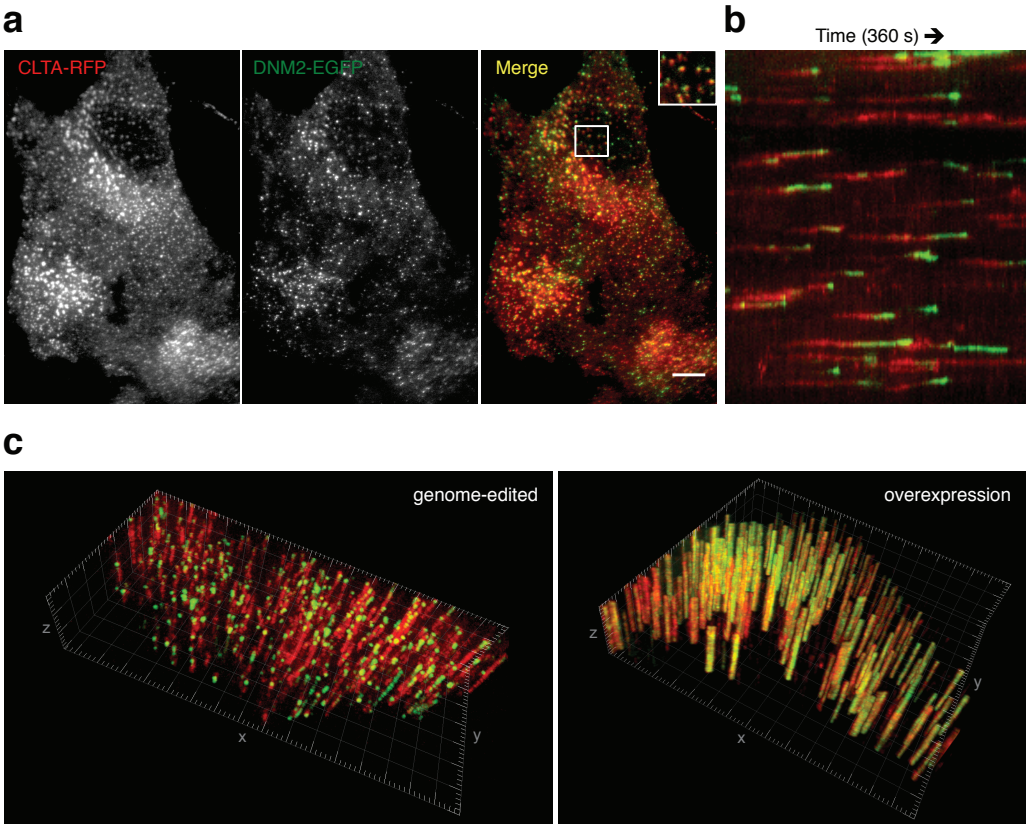

Figure 2.8 Fluorescence microscopy analysis of the hCLTAEN/hDNM2EN cell line. (a) TIRF microscopy image of hCLTA^{EN}/hDNM2^{EN} cell line expressing both CLTA-RFP and DNM2-EGFP. Scale bar, 10 μm. (b and c) Kymograph analyses of CLTA-RFP and DNM2-EGFP fluorescence over time. (c) Three-dimensional kymograph analysis of the genome-edited hCLTA^{EN}/hDNM2^{EN} cell line as compared to a SK-MEL-2 cell transiently overexpressing CLTA-RFP and DNM2-GFP. x-y plane (2.5 μm2 grid), cell plasma membrane; z-axis, time (240 s, 2 s/slice).

Table 2.5

Oligo	Sequence
BSC-1 CLTA Cel-1 F	GCAGCAGAAGAAGCCTTTGT
BSC-1 CLTA Cel-1 R	TTACTCCTCCCCTTCCTCTC
SK-MEL-2 CLTA Cel-1 F	GCAGCAGAAGAAGCCTTTGT
SK-MEL-2 CLTA Cel-1 R	TTCCTCCTCTCCCTCCTCTC
SK-MEL-2 DNM2 Cel-1 F	CCCTCCCCACCTGTCTTTAT
SK-MEL-2 DNM2 Cel-1 R	GAGACTCCATCCCCCAAAGT
BSC-1 CLTA TI F	AAAACTGGCTTTGGGTCCTAGC
BSC-1 CLTA TI F	CATCACCTAAAACGAGCCAGGT
SK-MEL-2 CLTA TI F	ATTCTGGGCTGCACCTTATCAA
SK-MEL-2 CLTA TI R	CATCACCTAAAACGAGCCAGGT
SK-MEL-2 DNM2 TI F	GCTCAACATCATCGGTGACATC
SK-MEL-2 DNM2 TI R	GATTTCCTGGCCCCTCTACTGT
BSC-1 CLTA-HA-F	GTCCTTTCCGGCTGTAGCTCC
BSC-1 CLTA-HA-R	CATGTGCCTGGTAAATACTGCATTGG
SK-MEL-2 CLTA-HA-F	GGTGGGCTGACCTTGAT
SK-MEL-2 CLTA-HA-R	TCTATAACCTGTGCTATCCGAG
BSC-1 CLTA-QC-F	GCCCCGCTGGTGCACGGTACCGCCACCCTGTGGAAAC
BSC-1 CLTA-QC-R	GTTTCCACAGGGTGGCGGTACCGTGCACCAGCGGGGC
SK-MEL-2 CLTA-QC-F	CAAGCAGGCCCCGCTGGTGCACGGTACCGCCACCCTGTGGAAACACTACATCTGC
SK-MEL-2 CLTA-QC-R	GCAGATGTAGTGTTTCCACAGGGTGGCGGTACCGTGCACCAGCGGGGCCTGCTTG
BSC-1 RFP-Kpn-F	GACGTCGAGGGTACCAGCGGCGGAAGCATGGTGTCTAAGGGCGAAGAGCTG
BSC-1 RFP-Kpn-R	GACGTCGAGGGTACCGTGCACCAGCGGGGCCTGCTTGAGGG
SK-MEL-2 RFP-Kpn-F	GGTACCAGCGGCGGAAGCATGGTGTCTAAGGGCGAAGAGC
SK-MEL-2 RFP-Kpn-R	GGTACCGAATTCATTACTTGTACAGCTCGTCCATGC
DNM2-HA-F	TGTTTGCCAACAGTGACCTC
DNM2-HA-R	GTGCAGGGGGTCAGAGAATA
DNM2-QC-F	CCAGCCGAACCATCCCTGCTCGACGGTACCTCGAGGGGGGCGTGCTCT
DNM2-QC-R	AGAGCACGCCCCCCTCGAGGTACCGTCGAGCAGGGATGGTTCGGCTGG
GFP-Kpn-F	GGTACCAGCGGCGGAAGCATGGTGAGCAAGGGCGAG
GFP-Kpn-R	GGTACCGAATTCATTACTTGTACAGCTCGTCCATGC
CLTA-SQ R	ATGCCAGGGAGAACACAGT
DNM2-SQ R	GCCAGCGTTAAGGAAGAGG

Table 2.5 Sequences of oligos used in the PCR, Cel-1, and sequencing reactions.

DISCUSSION

Significant advances in our understanding of endocytosis have been made by generating cell lines carrying overexpressed transgenes encoding fluorescent protein fusions (Merrifield *et al*., 2002, 2004, 2006; Ehrlich *et al*., 2004; Huang *et al*., 2004; Soulet *et al*., 2005; Rappoport *et al*. 2006; Le Clainche *et al*., 2007; Liu *et al*., 2008; Pucadyil and Schmid, 2008; Kirchhausen, 2009; Loerke *et al*., 2009; Mettlen *et al*., 2009a, 2009b, 2010; Saffarian *et al*., 2009). Although such studies have provided unique and powerful insights into understanding endocytic mechanisms and regulation, the impact of fusion protein overexpression on proper endocytic function was unclear. We found that the dynamics and function of both clathrin and dynamin in two different species (monkey and human) are significantly impaired by overexpression. We expect the same phenomenon to be true for many other proteins, including those that have multiple interaction partners and/or regulate rate- limiting steps in biosynthetic or signalling pathways.

In this study, we performed ZFN-mediated genome editing in mammalian cells to create precise, in-frame fluorescent protein fusions at the genomic loci of endocytic proteins. In yeast cells, where construction of precise protein fusions at genomic loci has long been routine for expression of fluorescent protein fusions at endogenous levels, endocytosis has been described as a very regular process. The predictable timing and ordering of endocytic protein recruitment in yeast have allowed for detailed descriptions of the timing of events in the endocytic pathway and for extensive mutant analysis of the contributions of individual proteins to CME dynamics (Kaksonen *et al*., 2005). By contrast, reports of variability in the size and dynamic behaviour of clathrin structures in mammalian cells have raised questions about the underlying biological significance of the different populations and about the regulatory mechanisms responsible for this heterogeneity. Furthermore, this heterogeneity has limited the ability to perform a global analysis of protein dynamics to detect the phenotypes that are caused when endocytic protein functions are impaired. Our data suggest that conventional overexpression-based methods in mammalian cells contribute to heterogeneity in the size and dynamics of clathrin-coated structures, thus warranting the use of genome-edited cells for re-examination of the effects of cargo, cell physiology and function- perturbing manipulations on endocytic dynamics and productivity.

ZFN-mediated genome editing has several advantages over conventional methods for generating cell lines that stably express fluorescent fusion proteins. First, conventional methods require selection of a single splice variant for study and, consequently, dominant expression of a single isoform. Moreover, these methods result in transgene overexpression, leading to total protein levels (comprising both tagged and untagged forms) that are significantly higher than in wild-type cells. Although transient overexpression methods can generate cells that express a fusion protein closer to physiological levels, they often result in heterogeneous cell-to-cell protein expression levels, necessitating experimental bias in the selection of ‘low-expression’ cells for study. By contrast, a ZFN-mediated strategy allows for creation of single- or multiple-allele tagged cell lines for greater control of a tagged protein’s expression level. Furthermore, our tagging strategy preserves native RNA splicing, enabling the analysis

of protein isoforms at physiological stoichiometry and levels. Although such an approach precludes an analysis of individual splice variants, alternative ZFNs and donors could be readily designed to achieve exclusive expression of a desired isoform at endogenous levels.

Although the need to perturb a biological process to observe it is a general shortcoming of experimental research, we believe that our studies strike a balance between modifying a cell to faithfully report on its biology and retaining its natural state. In particular, the ability to engineer isogenic human cells using ZFN technology in a manner that has been the gold standard in budding and fission yeast for decades has the potential to transform the way that researchers study dynamic processes (Urnov *et al*., 2010; DeKelver *et al*., 2010; Hockemeyer *et al*., 2009).

SUMMARY

In mammalian cells, fluorescent fusions of clathrin and other endocytic proteins have been used to establish a widely accepted view of clathrin-mediated endocytosis as a dynamic yet heterogeneous and inefficient process. Much has been made of the inefficiency and heterogeneity, as these features have suggested complexity in regulation of the process. However, the basis for this heterogeneity and its functional implications are not known. In contrast, in yeast, where GFP fusions are expressed from their own promoters at endogenous levels, the endocytic process is uniform, rapid and efficient. Use of current gene expression methods in mammalian cells has dictated that the fluorescent fusion proteins used for these (and all mammalian cell biology) studies be overexpressed. Furthermore, researchers have typically expressed splice variants and isoforms derived from a species that differs from that of the target cell under investigation. While there is widely appreciated concern that protein mis-expression may perturb the processes being investigated in mammalian cells, the impact of mis-expression has so far been impossible to directly test.

Here, to express RFP and GFP fusions of clathrin light chain A and dynamin-2 at physiological levels, we used zinc-finger nucleases and gene editing technology to precisely tag genomic loci in mammalian cells. Previously, gene-editing technology had been used for studies of gene expression and to inactivate genes, but not to create in-frame fusion proteins for real-time dynamics analysis. Using the cell lines generated for this study, we have re-examined the dynamics of clathrin-mediated endocytosis, and found that the process is considerably more rapid, efficient, and regular than had been found previously. Whereas previous studies using overexpression cell lines relied on inference-based statistical analyses to estimate endocytic productivity, a genome-edited cell line that expressed tagged forms of both clathrin and dynamin-2 allowed us to observe and examine productivity directly, in a global and unbiased manner. We show that ~91% of clathrin coated structures were joined by the vesicle scission factor dynamin before their disappearance, indicating that the efficiency of clathrin-mediated endocytosis in mammalian cells is much higher than previously appreciated, and is in fact similar to the efficiency observed in yeast where fluorescent protein fusions are routinely expressed at physiological levels from the normal genomic loci. Collectively, these findings suggest that the source of mammalian CCP heterogeneity, a long-standing unknown, is at least in part due to overexpression.

Overall, this study demonstrates novel use of genome editing, allowing for the first time the analysis of a dynamic process in real-time using fluorescent protein fusions expressed at endogenous levels using normal splice variants of endogenous genes, and shows that there is a serious, yet easily solved problem with how cell biology studies in mammalian cells are currently being conducted.

MATERIALS AND METHODS

ZFN design, screening, and characterization. ZFNs designed to target +/- 50 bp of the stop codons of CLTA and DNM2 were assembled using an archive of pre-validated zinc finger modules (Isalan *et al*., 2001; Urnov *et al*., 2005; DeKelver *et al*., 2010). All ZFNs carried enhanced obligate heterodimer (eHF) alleles of the FokI endonuclease: Q486E/I499L/N496D and E490K/I538K/H537R (Doyon *et al*., 2011). ZFNs were prescreened for activity in K562 and SK-MEL-2 cells using Surveyor nuclease (Cel-1, Transgenomic, Omaha, NE) to detect indels (Urnov *et al*., 2005). Briefly, Accuprime Taq HiFi (Invitrogen, Carlsbad, CA) was used with the Cel-1 primers listed in Table 2.5 to amplify a short region surrounding the ZFN- target site in a 28-cycle PCR. Resulting amplicons were denatured, slowly re-annealed, and treated with Cel-1 for 20 min at 42°C, then separated on 10% criterion gels (Bio-Rad, Hercules, CA) and visualized by ethidium bromide staining.

Out-out PCR to detect targeted integration at CLTA and DNM2. PCR was used to screen BSC-1 and SK-MEL-2 clones that were RFP- (CLTA) and/or GFP- (DNM2) positive after FACS enrichment. For the initial pre-screening of clones, 2 µl of genomic DNA prepared using QuickExtract (Epicentre Biotechnologies, Madison, WI) was amplified in a 35-cycle Accuprime Taq HiFi (Invitrogen, Carlsbad, CA) PCR with the TI primers listed in Table 2.5. An extension time of 10 min was used to minimize bias against the tagged allele(s) of the targeted gene. PCR products were analyzed on 5% criterion gels (Bio-Rad, Hercules, CA) that were run for 3-4 h at 150 V and visualized with ethidium bromide. Positive clones were then reanalyzed independently using genomic DNA prepared with the Masterpure kit (Epicentre Biotechnologies, Madison, WI) in 30-cycle PCRs with 100 ng template DNA. The resulting amplicons were analyzed by PAGE as described above. Clones suitable for further analysis were identified by cloning the out-out PCR products into pCR2.1 TOPO (Invitrogen, Carlsbad, CA) and conventional sequencing.

Cell culture. SK-MEL-2 cells and BSC-1 cells were purchased from the ATCC. BSC-1 GFP-LCa (rCLTA^{X}) cells were kindly provided by Tomas Kirchhausen, Harvard Medical School. All cells were maintained under 5% CO2 at 37°C in DMEM/F-12 (Invitrogen, Carlsbad, CA) supplemented with 10% FBS (HyClone, Logan, UT), except for BSC-1 GFP-CLTA cells, for which the media was supplemented with 0.5 mg/ml G418 (Invitrogen, Carlsbad, CA) for selection.

Plasmid construction. Human clathrin light chain A (CLTA) was amplified by PCR from a plasmid that was kindly provided by Lois Greene, NIH (Wu *et al*., 2001). This CLTA sequence is identical to the CLTA expressed in SK-MEL-2 cells. The African green monkey CLTA gene was amplified by RT-PCR from poly-A mRNA of BSC-1 cells and subcloned into a pEGFP-N1 vector (Clontech, Mountain View, CA) in which EGFP was replaced with TagRFP-T (RFP) (Shaner *et al*., 2008). TagRFP-T was a kind gift from Roger Tsien, UC San Diego. A GTSGGS linker was placed between CLTA and RFP.

Dynamin-2 (DNM2) was amplified by RT-PCR from poly-A mRNA of SK-MEL-2 cells and subcloned into a pEGFP-N1 vector with a GTSGGS linker between DNM2 and GFP.

Donor Design. Approximately 1.5 kb of genomic DNA sequence surrounding the CLTA (monkey or human for BSC-1 and SK-MEL-2, respectively) and DNM2 stop codons was amplified using the "HA" primers listed in Table 2.5 and cloned into pCR8-TOPO (Invitrogen, Carlsbad, CA). Next, a unique KpnI site was introduced via Quikchange (Agilent Technologies, Santa Clara, CA) site-directed mutagenesis with the "QC" primers. Finally, RFP or GFP was amplified using the "KpnI" primers, which encode an N-terminal GTSGGS linker and cloned into the KpnI site of the CLTA or DNM2 homology arm constructs, respectively.

Generation of stable overexpression cell lines. Human CLTA-RFP and DNM2-EGFP plasmids were transfected into SK-MEL-2 cells using Lipofectamine 2000 (Invitrogen, Carlsbad, CA), following the manufacturer's protocol. After 72 hours, transfected SK-MEL-2 cells were selected in DMEM/F-12 containing 10% FBS and 1 mg/ml G-418. African green monkey CLTA-RFP plasmid was transfected into BSC-1 cells using Fugene 6 (Roche, Basal, Switzerland), following a standard protocol. After 72 h, transfected BSC-1 cells were selected in DMEM/F-12 containing 10% FBS and 0.4 mg/ml G418. Single cell clones were selected and amplified by dilution cloning in 96-well plates.

Generation of genome-edited cell lines. ZFN and donor plasmids were transfected into cells using a single cuvette Amaxa Nucleofector device (Lonza, Basal, Switzerland), as per the manufacturer's protocol. In brief, cells grown to ~80% confluency were harvested by trypsinization, and 1-1.5 x 106 BSC-1 or SK-MEL-2 cells were resuspended in Nucleofector solution L or R and transfected using Nucleofector program A-020 or T-020, respectively. After transfection, cells were subjected to cold shock treatmentby incubation at 30ºC for 48 h before being transferred to 37ºC, 5% CO_2 (Doyon *et al*., 2010). Depending on the experiment, recovered cells were sorted for RFP-positive, GFP-positive or RFP- and GFP-positive signals using a DAKO-Cytomation MoFlo High Speed Sorter, either directly into 96-well plates or grown for 1 week and then cloned by limiting dilution.

Western immunoblotting. For the preparation of lysates, cells were briefly washed in PBS, incubated with 0.5 mM EDTA for 5 min, and pelleted at 1000 rpm for 2 min. The supernatant was subsequently removed, and hot 2X protein sample buffer (125 mM Tris-HCl, pH 6.8, 10% glycerol, 10% SDS, 130 mM DTT, 0.05% bromophenol blue, 12.5% β-mercaptoethanol) was immediately added. After pellet resuspension by pipet, samples were heated to 95ºC, for 3 min, separated by 8% or 12% SDS-PAGE, and transferred to Immobilon-FL PVDF (IPFL-00010, Millipore, Billerica, MA) or nitrocellulose membrane in transfer buffer (25 mM Trizma base, 200 mM glycine, 20% methanol, 0.025% SDS) at 50 V at 4ºC for 1 hour. The membrane was subsequently

rinsed in TBS and incubated in Odyssey blocking buffer (diluted 1:1 in PBS) at room temperature for 1 hr. Primary antibodies were diluted in blocking buffer and incubated with the membrane at 4ºC overnight. The membrane was incubated in the following primary antibodies: anti-CLTA (H-55; 1:100; Santa Cruz Biotechnology), anti-DNM2 (C-18; 1:1000; Santa Cruz Biotechnology), anti-actin (C4; 1:20,000; MP Biomedicals), anti-GFP (B2; 1:2000; Santa Cruz Biotechnology), or anti-tRFP (AB233; 1:500; Evrogen). Blots were subsequently incubated in the dark for 1 hr at room temperature with secondary IRDye 680 or 800CW antibodies (LI-COR Biosciences, Lincoln, NE) diluted at 1:5000 in Odyssey blocking buffer/PBS solution containing 0.1% Tween-20. After washing with TBST, the membrane was incubated in TBS and scanned on an Odyssey infrared imager (LI-COR Biosciences, Lincoln, NE). Quantification of protein bands was performed using the Odyssey Infrared Imaging System (version 3.0).

Total internal reflection fluorescence (TIRF) microscopy and live-cell imaging. TIRF microscopy images were captured using Metamorph software on an Olympus IX-81 microscope using a 60x/NA1.49 objective and an ORCA-R2 camera (Hamamatsu, Japan). The system was maintained at 37°C using a WeatherStation chamber and temperature controller (PrecisionControl, Tacoma, WA). At 16-24 hours prior to imaging, cells were seeded onto uncoated glass coverslips in growth medium. During imaging, cells were maintained in DMEM without phenol red that was supplemented with 5% FBS and 10 mM HEPES. A 488 nm solid-state laser (Melles Griot, Albuquerque, NM) and a 561 nm diode-pumped solid-state laser (Melles Griot, Albuquerque, NM) were used to excite GFP and RFP fluorophores, respectively. For lifetime analysis, images were acquired every 2 s for 6 min, with an exposure time of 900 ms. Simultaneous two-color TIRF images were obtained using a DV2 image splitter (MAG Biosystems, Santa Fe, NM) to separate GFP and RFP emission signals.

Transferrin uptake assay. Cells were grown on glass coverslips in 6-well plates overnight. The cells were serum-starved at 37ºC for 1 hr in starving medium (DMEM containing 20 mM HEPES, pH 7.4 and 5 mg/ml BSA). They were then incubated in starving medium containing 25 mg/ml Alexa Fluor 488- or Texas Red-conjugated human transferrin (Invitrogen, Carlsbad, CA) at 37ºC for 0-45 min before fixation in 4% PFA at room temperature for 20 min. After three washes with PBS, the coverslips were mounted onto glass slides using ProLong Gold antifade reagent (Invitrogen, Carlsbad, CA). The degree of transferrin uptake was quantified using ImageJ software (NIH, V1.44e). In brief, cell outlines were traced by using polygon or freehand selection tools, and the mean fluorescence intensity (arbitrary units) was measured for individual cells.

Immunofluorescence staining. Cells were grown on glass coverslips in 6-well plates overnight before fixation in 4% PFA at room temperature for 20 min. After three washes with PBS, the coverslips were quenched with 1 mg/ml $NaBH_4$ for 15 min twice, and the cells were permeabilized in 0.1% saponin/PBS or 0.1% Triton X-100/PBS. After brief washing with PBS, the coverslips were incubated with anti-clathrin HC antibody (MA1-065, Thermo Scientific) at 1:500 overnight at 4ºC. The coverslips were then washed with

PBS for 15 min before incubation with anti-mouse secondary antibody conjugated to Alexa Fluor 488 (A21202, Invitrogen) or Alexa Fluor 568 (A10037, Invitrogen) at 1:1000 dilution for 2 hr at room temperature. After three washes with PBS, the coverslips were mounted on glass slides using ProLong Gold antifade reagent (Invitrogen, Carlsbad, CA).

Particle detection, tracking, and image analysis. Particle detection and tracking were performed using Imaris 7.1 software (Bitplane Scientific, Zurich, Switzerland). Prior to particle detection, images were first subjected to background subtraction. The Spots module of Imaris was then used to automatically detect point-like particles with an estimated spot diameter of 500 nm (~5 pixels). After automatic detection, detected spots were filtered based on satisfying minimum 'intensity standard deviation' and 'quality' control parameters. Only spots with values higher than the set threshold values were considered for analyses. Quality is defined as the intensity at the center of the spot, Gaussian filtered by ¾ of the spot radius. Appropriate threshold values were confirmed by visual inspection of correct particle detection. To trace objects through sequential frames of time data, a Brownian motion particle-tracking algorithm was applied. A maximum search distance of 350 nm was defined to disallow connections between a Spot and a candidate match if the distance between the predicted future position of the Spot and the candidate position exceeded the maximum distance. A gap-closing algorithm was also implemented to link track segment ends to track segment starts to recover tracks that were interrupted by the temporary disappearance of particles. The maximum permissible gap length was set equal to 7 frames. Track outputs were then visually inspected and, as necessary, edited to correct for tracking errors. Only tracks that appeared and disappeared during the lifetime of the acquisition (i.e., 181 frames, 6 minutes) were subjected to lifetime analyses.

Statistical analysis. One-way ANOVAs were used to assess the effect of genome editing on the mean lifetime of endocytic proteins at the plasma membrane. Significant results were followed by post-hoc Tukey–Kramer HSD tests. All tests were performed using JMP 8.0.2 (SAS Institute, Cary, NC). Data are presented as mean ± S.E.M.

CHAPTER 3:
Dynamin and actin function in clathrin-mediated endocytosis

INTRODUCTION

Clathrin-mediated endocytosis (CME) is a key universal process in all higher eukaryotes, and the best-understood pathway by which portions of the plasma membrane, along with extracellular material, are internalized. This process is characterized by the recruitment and cooperation of clathrin triskelia, together with cargo, adaptors, and accessory proteins, to mediate formation of membrane invaginations called clathrin-coated pits (CCPs). Through live-cell imaging, pharmacological, and biochemical studies, over 40 proteins have now been implicated in this exquisitely choreographed process.

Absolutely essential to this pathway are the actions of the multidomain GTPase dynamin. During growth of a CCP, dynamin has been reported to slowly assemble at endocytic sites where it is believed to act as a regulator and/or fidelity monitor of rate-liming steps in CCP maturation (Sever *et al*., 2000; Loerke *et al.,* 2009; Mettlen *et al*., 2009). But as the invagination matures and grows inward, dynamin robustly and rapidly accumulates to the necks of CCPs to mediate membrane fission and vesicle release (Merrifield *et al*., 2002; Doyon *et al*., 2001; Taylor *et al*., 2011, 2012). Interestingly, live-cell studies show that dynamin recruitment and actin polymerization occur over a similar time course, suggesting a link between dynamin and actin interaction and function (Merrifield *et al.,* 2002; Taylor *et al*., 2012). Whether dynamin and actin coordinate in endocytosis is not well understood.

For cellular processes outside of endocytosis, a body of work conclusively supports a role for dynamin in actin cytoskeleton remodeling. In vivo, dynamin localizes to and functions within actin meshworks at structures including lamellopodia, membrane ruffles, and invadopodia (Baldassare *et al*., 2003; Kreuger *et al*., 2003; Schlunck *et al*., 2004). Recent in vitro studies also show that dynamin can bind to F-actin directly and, together with its binding partner cortactin, remodel actin filaments by enhancing sensitivity of filaments to severing by the actin depolymerizing factor, cofilin (Mooren *et al*., 2009). Intriguingly, dynamin has been reported to promote actin polymerization *in vitro* through direct interaction with short actin filaments (Gu *et al*., 2010). Collectively, these data illustrate that dynamin and actin can function together and raises the question of whether dynamin might coordinate with actin for clathrin-mediated endocytosis. Merrifield and colleagues recently showed evidence supporting a model in which actin serves as a scaffold to concentrate dynamin at sites of membrane scission (Taylor *et al*., 2012). However, dynamin and actin have not yet been simultaneously visualized in real-time and the specific mechanisms that govern these interactions remain unclear.

To gain insight into the proposed interdependency between actin and dynamin in endocytosis, we employed genome editing to engineer mammalian cells expressing fluorescent protein fusions of these proteins. These cells allowed us to directly and concurrently monitor endogenous beta-actin (ACTB) and dynamin-2 (DNM2) dynamics and perform global analyses of the effect of perturbations on their endocytic behaviors. Our data indicate that dynamin is regulated by actin and that it regulates its own function at endocytic sites.

RESULTS

Dynamin dynamics in genome-edited SK-MEL-2 cells

To define the contribution of actin to dynamin recruitment in clathrin-mediated endocytosis, we first sought to analyze the steady-state protein dynamics of endogenously expressed fluorescent fusion of dynamin-2 (DNM2) in a genome-edited SK-MEL-2 cell line (hCLTA^{EN}/hDNM2^{EN}) co-expressing a C-terminal genomic fusion of Tag-RFP-t to clathrin light chain A (CLTA-RFP; Doyon *et al*., 2011). Analysis of plasma membrane endocytic events using total internal reflection fluorescence microscopy (TIRF-M) revealed a high degree of co-localization between DNM2-GFP and CLTA-RFP punctae, supporting previous observations that dynamin functions in clathrin-mediated endocytosis (Figure 3.1A). The stable integration of fluorescent tags via genome editing provided uniform fluorescent protein expression across the entire cell population, thus affording us the ability to perform global analyses on protein recruitment and disassembly kinetics. By simultaneously following clathrin and dynamin, we observed that DNM2-GFP was recruited to clathrin punctae near the end of their lifetimes, consistent with dynamin's role in catalyzing membrane scission (Figure 3.1b). Moreover, dynamin's recruitment to clathrin punctae was robust, displaying as a bright burst of GFP coincident with a sharp decrease in CLTA-RFP fluorescence, the latter indicative of CCP internalization.

Since the lifetimes of clathrin punctae in mammalian cells have been well documented to be wide ranging, we next investigated whether dynamin was differentially recruited to clathrin tracks of varying lifetimes. An unbiased automated global analysis of clathrin and dynamin punctae showed that dynamin punctae overwhelmingly (91 ± 2.7%) overlapped with clathrin punctae having lifetimes greater than 20 seconds, which comprised 56% of CCPs, but rarely (~5.9 ± 1.1%) with punctae with shorter lifetimes (*$P < 0.0001$; Figures 3.1c - e).

Since the lifetimes of clathrin punctae are heterogeneous, we next sought to probe dynamin variability at endocytic sites (Figure 3.1f). By tracking DNM2-GFP punctae, we found that dynamin lifetimes distributed in a Gaussian manner, with an average lifetime of 18 ± 1.6 seconds (Figure 3.1g). Moreover, analysis of individual endocytic events having lifetimes > 20 seconds revealed that DNM2-GFP displayed highly regular recruitment/de-recruitment kinetics independent of clathrin recruitment dynamics (Figure 3.1h). Collectively, these data show that late stage recruitment of dynamin to endocytic sites is highly regular despite high clathrin lifetime heterogeneity, suggesting that the scission step of endocytosis is forward-feeding and terminal.

Acute actin perturbation affects dynamin behavior

Studies examining the effects of actin-perturbing drugs on CME provided evidence for actin functions in mammalian endocytosis (Lamaze *et al*., 1997; Fujimoto *et al*., 2000; Yarar *et al*., 2005; Boulant *et al*., 2011; Taylor *et al*., 2012). Yet, a clear understanding of how actin contributes to CCP maturation and endocytic productivity still remain elusive. Additionally, a thorough analysis of the effects of actin drugs on

Figure 3.1

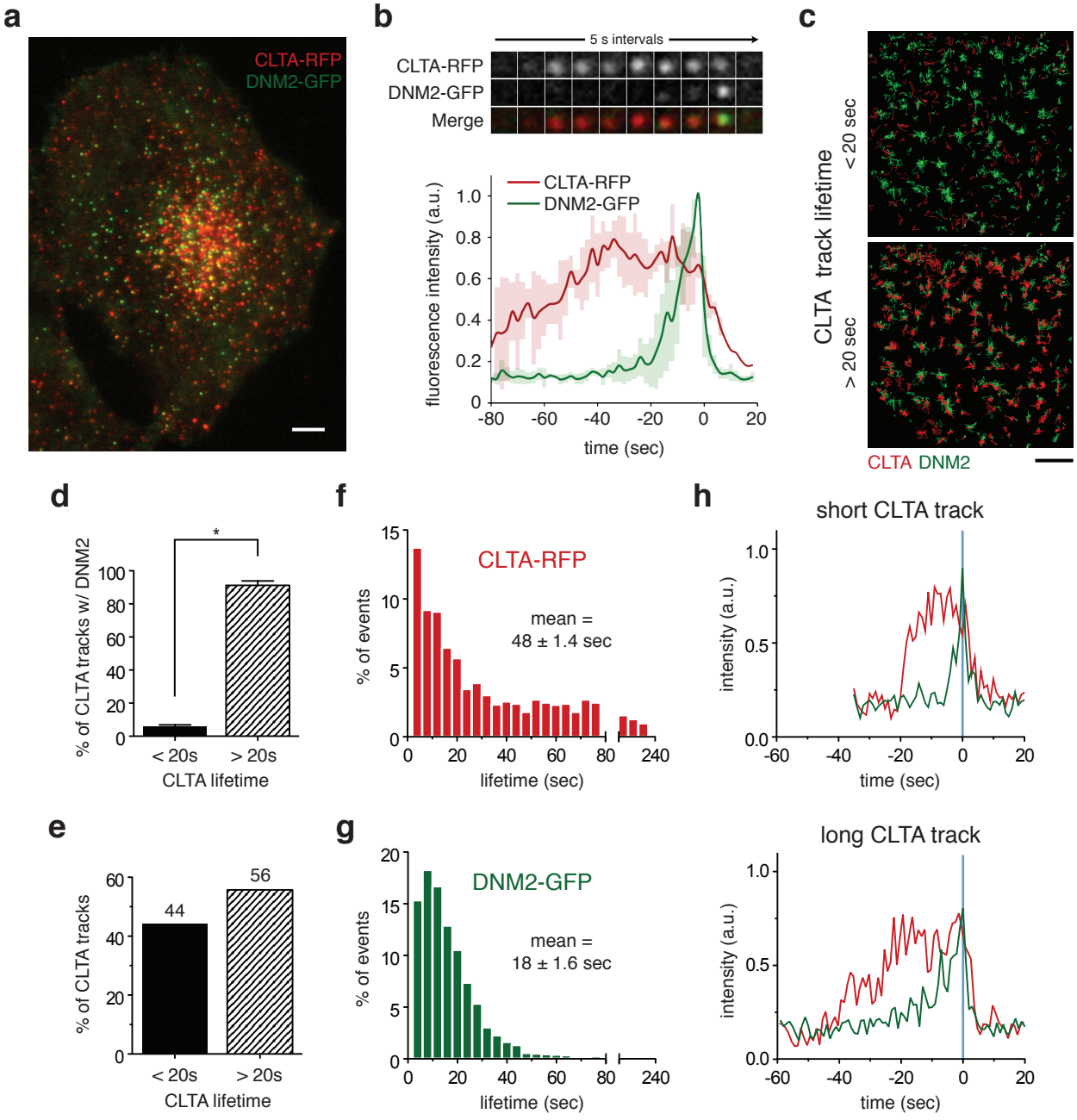
a
CLTA-RFP
DNM2-GFP
b
5 s intervals
CLTA-RFP
DNM2-GFP
Merge
fluorescence intensity (a.u.)
time (sec)
c
CLTA track lifetime
< 20 sec
> 20 sec
CLTA DNM2
d
% of CLTA tracks w/ DNM2
< 20s
> 20s
CLTA lifetime
e
% of CLTA tracks
44
56
f
CLTA-RFP
mean =
48 ± 1.4 sec
% of events
lifetime (sec)
g
DNM2-GFP
mean =
18 ± 1.6 sec
h
short CLTA track
long CLTA track
intensity (a.u.)
time (sec)

Figure 3.1 Dynamin recruitment to sites of endocytosis. (a) TIRF microscopy image of a representative SK-MEL-2 hCLTA^{EN}/hDNM2^{EN} cell expressing both CLTA-RFP and DNM2-EGFP. Scale bar, 5μm. (b) Representative montage (top) and average fluorescence intensity profile (bottom) of an endocytic event (tracks = 42; n = 3 cells). Shaded bars represent standard error of the mean (S.E.M.) (c) Representative overlays of a cropped region (10μm x 10μm) of cell imaged for 120 frames (240s) in which all DNM2-GFP tracks (in green) are displayed (identically in both images), while CLTA-RFP tracks (in red) are segmented by lifetime and displayed as tracks < 20s or > 20s on top or bottom images, respectively. Scale bar, 2μm. (d) The mean percentage of CLTA punctae (± S.E.M), of <20s or >20s duration, that display robust dynamin recruitment (tracks = 903 or 815, respectively; n = 5 cells; *P < 0.0001). (e) The percentage of CLTA punctae having lifetimes <20s or >20s (tracks = 21,455; n = 5 cells). (f and g) Global lifetime distribution of CLTA-RFP and DNM2-GFP punctae (mean = 48 ± 1.4 sec or 18 ± 1.6 sec, respectively; tracks = 21,455 or 1706, respectively; n = 5 or 3 cells, respectively). (h) Representative fluorescence intensity profiles of short (top) and long-lived (bottom) endocytic events. Blue line denotes time of maximum DNM2-GFP fluorescence.

endocytic proteins other than clathrin is lacking. To gain a more precise understanding of actin's mode of action, we took advantage of the two-color hCLTA^{EN}/hDNM2^{EN} genome-edited cell line and probed the effects of various actin drugs on both clathrin and dynamin dynamics.

Addition of the F-actin stabilizing drug, jasplakinolide (1μM), to cells resulted in an immediate (2 - 4 sec) and dramatic decrease in the fluorescence intensity of DNM2-GFP membrane punctae (Figure 3.2a and b). Consistent with previous reports, clathrin punctae lifetimes increased dramatically, suggesting a stalling of clathrin-coated pit progression (Figure 3.2b; Yarar *et al*., 2005; Boulant *et al*., 2011; Taylor *et al*., 2012). Analysis of DNM2-GFP membrane punctae after drug exposure also showed a global prolonging of dynamin membrane lifetime (Figure 3.2c). Moreover, the number of dynamin punctae per unit membrane area decreased (by 63%), which is likely due, at least in part, to an observed significant decrease (66% reduction) in the rate of DNM2-GFP initiation (Figures 3.2e and f; *P = 0.0005 and 0.0001, respectively).

In contrast to jasplakinolide treatment, which decreased the fluorescence of DNM2-GFP punctae, exposure of cells to increasing concentrations of cytochalasin D (CytoD) and latrunculin A (LatA), drugs that block actin polymerization, caused DNM2-GFP punctae to maintain their intensities and increase their lifetimes in a dose-dependent manner (Figure 3.2g). With increasing drug concentration, the kinetic profiles for DNM2-GFP became increasingly irregular (Figure 3.2h). Additionally, we measured a progressive increase in the average time from dynamin punctae nucleation to disassembly and a decrease in both the rates of dynamin recruitment and de-recruitment (Figures 3.2i - k). Together, these experiments demonstrate a dependency of CME on actin dynamics. Moreover, the differential effects of actin stabilizing versus actin-destabilizing drugs on dynamin recruitment reveal a requirement for actin filament turnover in regulation of dynamin function and coated-pit maturation.

Dynamics of actin expressed at endogenous levels

To directly observe actin associated with sites of CME, we designed ZFNs targeting the 5′-terminus of the beta-actin gene (ACTB) and used them in previously genome-edited SK-MEL-2 cells bearing CLTA-RFP (SK-MEL-2 hCLTA^{EN-1}) or DNM2-GFP (hDNM2^{EN-1})(see Chapter 1; Doyon *et al*., 2011). We generated two cell lines, hCLTA^{EN}/hACTB^{EN} and hDNM2^{EN}/hACTB^{EN}, in which one ACTB allele was tagged with TagGFP or TagRFP-t, respectively (Figure 3.3a). Genotyping and western blot analysis confirmed the accurate integration of these tags at the ACTB locus (data not shown). As expected, hACTB^{EN} cells displayed fluorescent structures that co-localized with phalloidin-stained stress fibers and lamellapodia. This result demonstrates that fluorescent fusions of ACTB are readily incorporated into a variety of actin structures, and therefore at least partially functional (Figure 3.4a). In fixed cells, fluorescent fusions of ACTB co-localized with phalloidin cortical punctae, and a subset of CLTA-RFP and DNM2-GFP punctae, supporting a role for actin in CME (Figure 3.3b and Figure 3.4b).

Given the partial overlap of fluorescently-labeled ACTB with clathrin and dynamin, we sought to elucidate the extent and precise timing of actin recruitment and de-recruitment at endocytic sites using live-cell TIRF-M microscopy. Analysis of

Figure 3.2

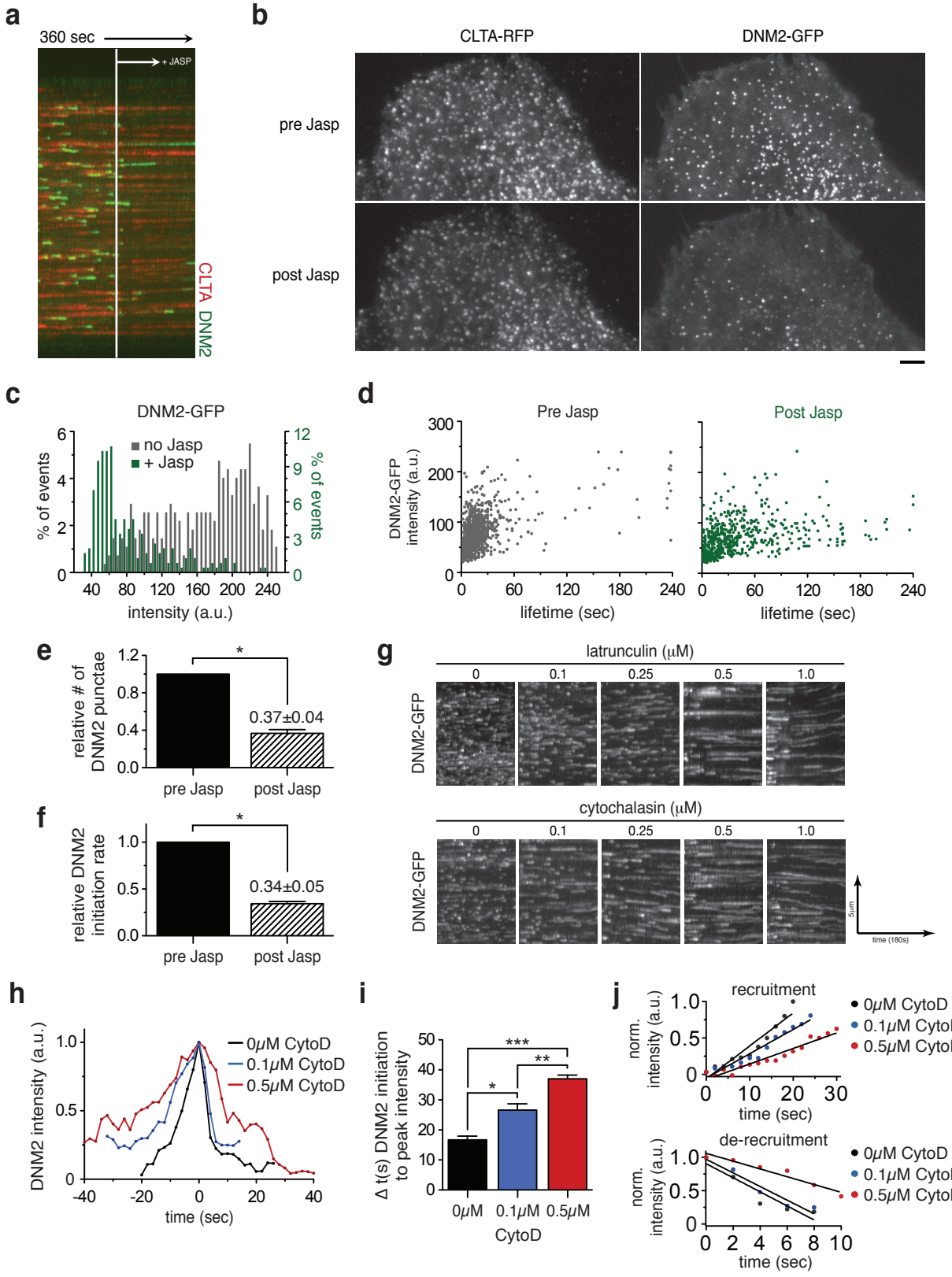
a
360 sec
+ JASP
CLTA DNM2
b
CLTA-RFP
DNM2-GFP
pre Jasp
post Jasp
c
DNM2-GFP
no Jasp
+ Jasp
% of events
% of events
intensity (a.u.)
d
Pre Jasp
Post Jasp
DNM2-GFP intensity (a.u.)
lifetime (sec)
lifetime (sec)
e
relative # of DNM2 punctae
0.37±0.04
pre Jasp
post Jasp
f
relative DNM2 initiation rate
0.34±0.05
pre Jasp
post Jasp
g
latrunculin (μM)
cytochalasin (μM)
DNM2-GFP
DNM2-GFP
5μm
time (180s)
h
DNM2 intensity (a.u.)
0μM CytoD
0.1μM CytoD
0.5μM CytoD
time (sec)
i
Δ t(s) DNM2 initiation to peak intensity
0μM
0.1μM
0.5μM
CytoD
j
recruitment
norm. intensity (a.u.)
time (sec)
0μM CytoD
0.1μM CytoD
0.5μM CytoD
de-recruitment
norm. intensity (a.u.)
time (sec)
0μM CytoD
0.1μM CytoD
0.5μM CytoD

Figure 3.2 The effects of actin inhibitors on dynamin kinetics. (a and b) Representative TIRF-M kymograph analysis (a; Time = 2s/pixel, 360s total) and maximum intensity projection of fluorescence over time (b) of a SK-MEL-2 $hCLTA^{EN}/hDNM2^{EN}$ cell subjected to acute 1μM jasplakinolide exposure. White line in (a) marks time of drug addition. A maximum intensity projection of fluorescence intensity over time (b; of imaging duration = 120s) was generated for each condition ending or beginning 30s prior to or post drug exposure, respectively. # punctae analyzed = 323 and 245, respectively. Scale bar, 2μm. (c) Fluorescence intensity distribution of DNM2-GFP membrane punctae projections displayed in (b), before and after 1μM jasplakinolide exposure. (d) Maximum fluorescence intensity - lifetime dot plot for DNM2-GFP tracks before and after 1μM jasplakinolide exposure. Each dot represents a single DNM2 track (# tracks analyzed = 1017 and 641, respectively). Imaging began 180s prior to drug addition, and terminated 180s after drug addition. Tracks existing within these time frames (pre and post drug addition) were analyzed. (e) Relative number of DNM2-GFP membrane punctae (± S.E.M.), both dim and bright, before and after 1μM jasplakinolide exposure (# punctae analyzed = 369 and 134, respectively; n = 3 cells; *P = 0.0005). (f) Relative DNM2-GFP initiation rate (± S.E.M.) before and after 1μM jasplakinolide exposure (# tracks analyzed = 1150 and 450, respectively; n = 3 cells; *P = 0.0001). (g) Representative TIRF-M kymograph analysis of DNM2-GFP fluorescence over time in SK-MEL-2 $hCLTA^{EN}/hDNM2^{EN}$ cells exposed to varying concentrations (0 - 1.0μM) of latrunculin A or cytochalasin D actin drug. Drug exposure begins at kymograph start and remains throughout entire kymograph. (h-j) Average fluorescence intensity profile (h), average time (± S.E.M.) from initiation to peak intensity (i), and slope of recruitment and de-recruitment of DNM2-GFP (j) in cells subjected to varying concentrations (0 - 1.0μM) of cytochalasin D (cytoD) (tracks = 15; n = 3 cells; *P = 0.0034, **P = 0.0056, and ***P < 0.0001).

Figure 3.3

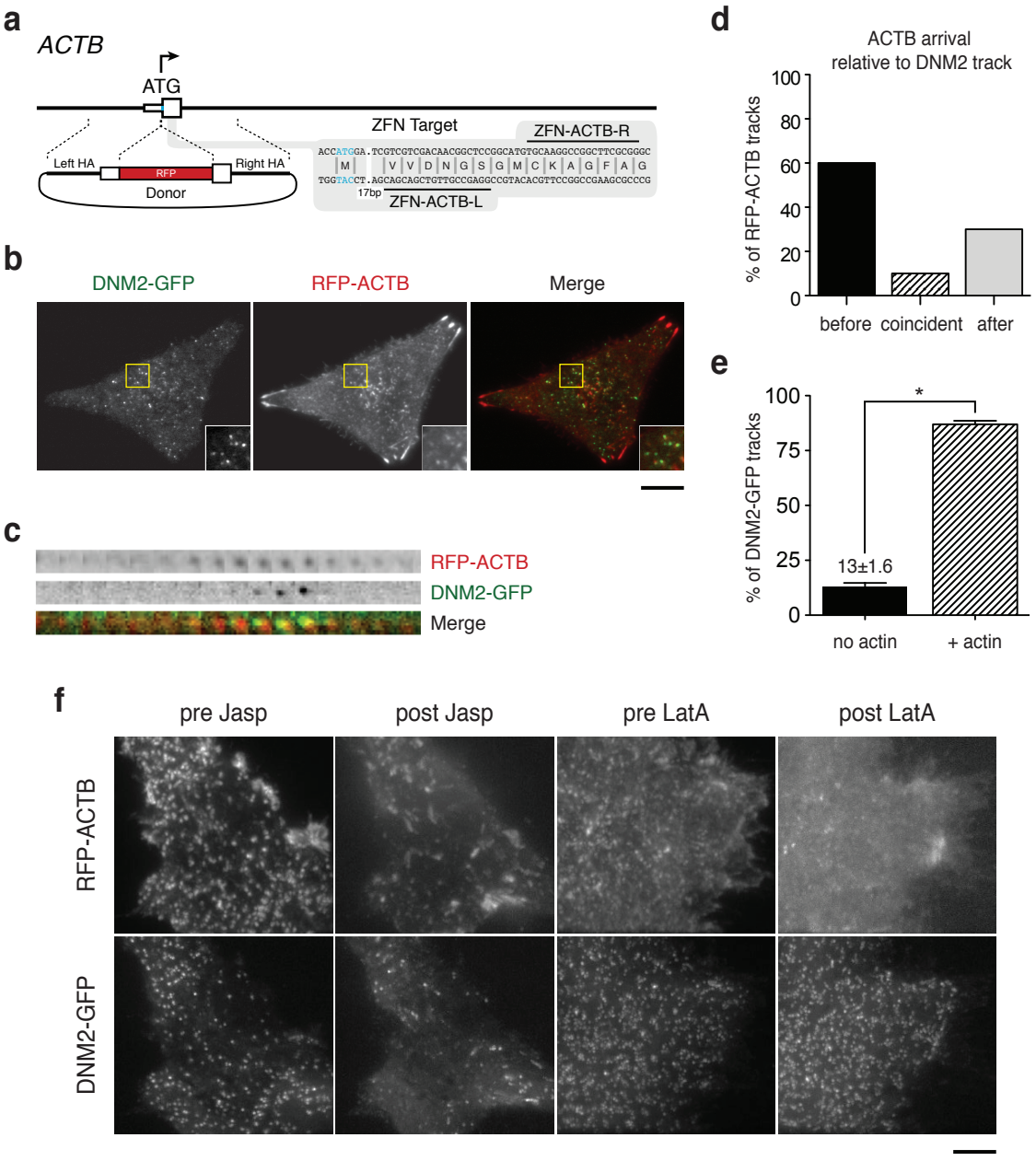
a
ACTB
ATG
ZFN Target
ZFN-ACTB-R
Left HA
RFP
Right HA
Donor
17bp
ZFN-ACTB-L
b
DNM2-GFP
RFP-ACTB
Merge
c
RFP-ACTB
DNM2-GFP
Merge
d
ACTB arrival relative to DNM2 track
% of RFP-ACTB tracks
100
80
60
40
20
0
before
coincident
after
e
% of DNM2-GFP tracks
100
75
50
25
0
*
13±1.6
no actin
+ actin
f
pre Jasp
post Jasp
pre LatA
post LatA
RFP-ACTB
DNM2-GFP

Figure 3.3 Endogenous actin dynamics in genome-edited SK-MEL-2 cells. (a) Schematic overview depicting the targeting strategy for integration of Tag-RFP-t (RFP) at the beta-actin (ACTB) genomic locus. White boxes, exons of CLTA. HA, donor plasmid region of homology to CLTA sequence. Blue letters, start codon. (b) TIRF microscopy image of a representative SK-MEL-2 hDNM2/hACTB^{EN} cell expressing both DNM2-GFP and RFP-ACTB. Yellow box defines inset. Scale bar, 10μm. (c) Representative montage of an endocytic event. (d) Percentage of RFP-ACTB (± S.E.M.) punctae arriving before, coincident, or after DNM2-GFP punctae (# tracks analyzed = 100; n = 3 cells). (e) Percentage of DNM2-GFP punctae (± S.E.M.) displaying RFP-ACTB recruitment (# tracks analyzed = 645; n = 3 cells; *P < 0.0001).(f) TIRF-M image of actin morphology and DNM2-GFP localization in SK-MEL-2 hDNM2/hACTB^{EN} cells pre- and post- 1μM jasplakinolide (Jasp) or latrunculin A (LatA) exposure. Scale bar, 5μm.

Figure 3.4

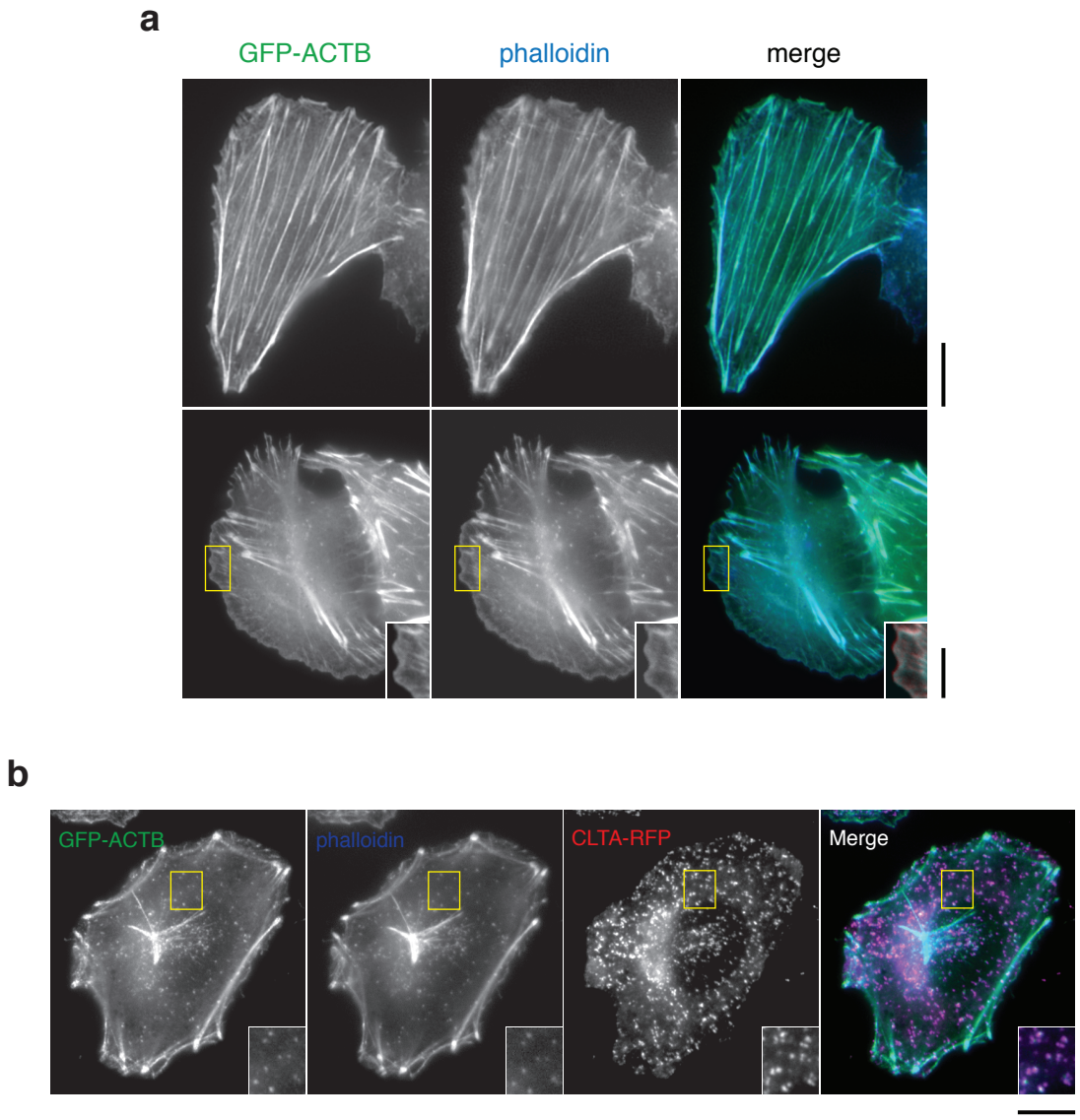

Figure 3.4 Epifluorescence microscopy analysis of genome-edited SK-MEL-2 cells expressing GFP-ACTB. (a) SK-MEL-2 cells display complete GFP-ACTB co-localization with Alexa Fluor 350 conjugated phalloidin-stained actin structures. Yellow boxes demarcate inset regions. Scale bars = 10μm. (b) Genome-edited SK-MEL-2 cells expressing CLTA-RFP and GFP-ACTB (hCLTA^{EN}/hACTB^{EN}) display high degree of co-localization between actin and clathrin plasma membrane punctae. Scale bar = 10μm.

DNM2-GFP punctae showed that ACTB arrives within a similar time frame to DNM2-GFP, which is consistent with previous reports over-expressing DNM2-GFP and (Figure 3.3c; Merrifield *et al.*, 2002; Taylor *et al.*, 2011, 2012). Further analysis of actin dynamics revealed that its arrival at endocytic sites is variable relative to dynamin (Figure 3.3d). Nevertheless, nearly all dynamin-containing endocytic events (87 ± 1.6%) displayed RFP-ACTB recruitment, and in a majority (~60%) of events, RFP-ACTB preceded DNM2-GFP recruitment (Figure 3.3d). Cumulatively, these data provide direct evidence supporting the conclusion that actin and dynamin dynamics are tightly linked.

Since actin-stabilizing and -depolymerizing drugs had differential effects on dynamin behavior, we sought to directly examine how these drugs perturbed actin architecture *in vivo*. Exposure of $hDNM2^{EN}$/$hACTB^{EN}$ cells to jasplakinolide (1μM) caused a striking decrease in both the intensity and density of DNM2-GFP membrane punctae, which is consistent with our drug experiments in $hCLTA^{EN}$/$hDNM2^{EN}$ cells (Figure 3.3f). While some RFP-ACTB punctae disappeared after jasplakinolide treatment, a large proportion remained at the surface as larger RFP-ACTB structures, which presumably grew as a consequence of the stabilizing properties of the drug. In contrast, 1μM LatA treatment resulted in a complete loss of RFP-ACTB membrane punctae but preservation of DNM2-GFP punctae (Figure 3.3f). In sum, these experiments establish that active turnover of actin filaments drives the continued recruitment of dynamin to endocytic sites.

Dynamin recruitment is concentration dependent

While several endocytic proteins have been shown to influence dynamin dynamics, data showing concentration dependence of dynamin recruitment to endocytic sites are lacking (Takei *et al.*, 1999; Taylor *et al*., 2012). We took advantage of the uniform and stable protein expression afforded by endogenous gene tagging to directly examine the dependency of protein function on protein concentration, thereby circumventing traditional methods that require the concurrent siRNA depletion and ectopic over-expression of fluorescent protein fusions. To deplete DNM2-GFP, we delivered siRNA oligos against GFP into cells, and at 3 days post-transfection, collected pools of cells, depleted of DNM2-GFP to varying degrees, by fluorescence-activated cell sorting (Figure 3.5a). Moderate depletion of dynamin caused a decrease in the average maximum intensity of DNM2-GFP punctae, while at the same time prolonging their lifetimes (Figures 3.5b, d, e, and g). Surprisingly, while severe depletion of dynamin additionally depressed the maximum intensity of DNM2-GFP punctae, it did not further extend dynamin punctae lifetime. Rather, DNM2-GFP punctae appeared as exceedingly short bursts, existing on average for only 1-2 acquisition frames (2-4 sec; Figures 3.5c, f, and g). Together, these data illustrate that dynamin recruitment to endocytic sites is strongly influenced by its own concentration.

Figure 3.5

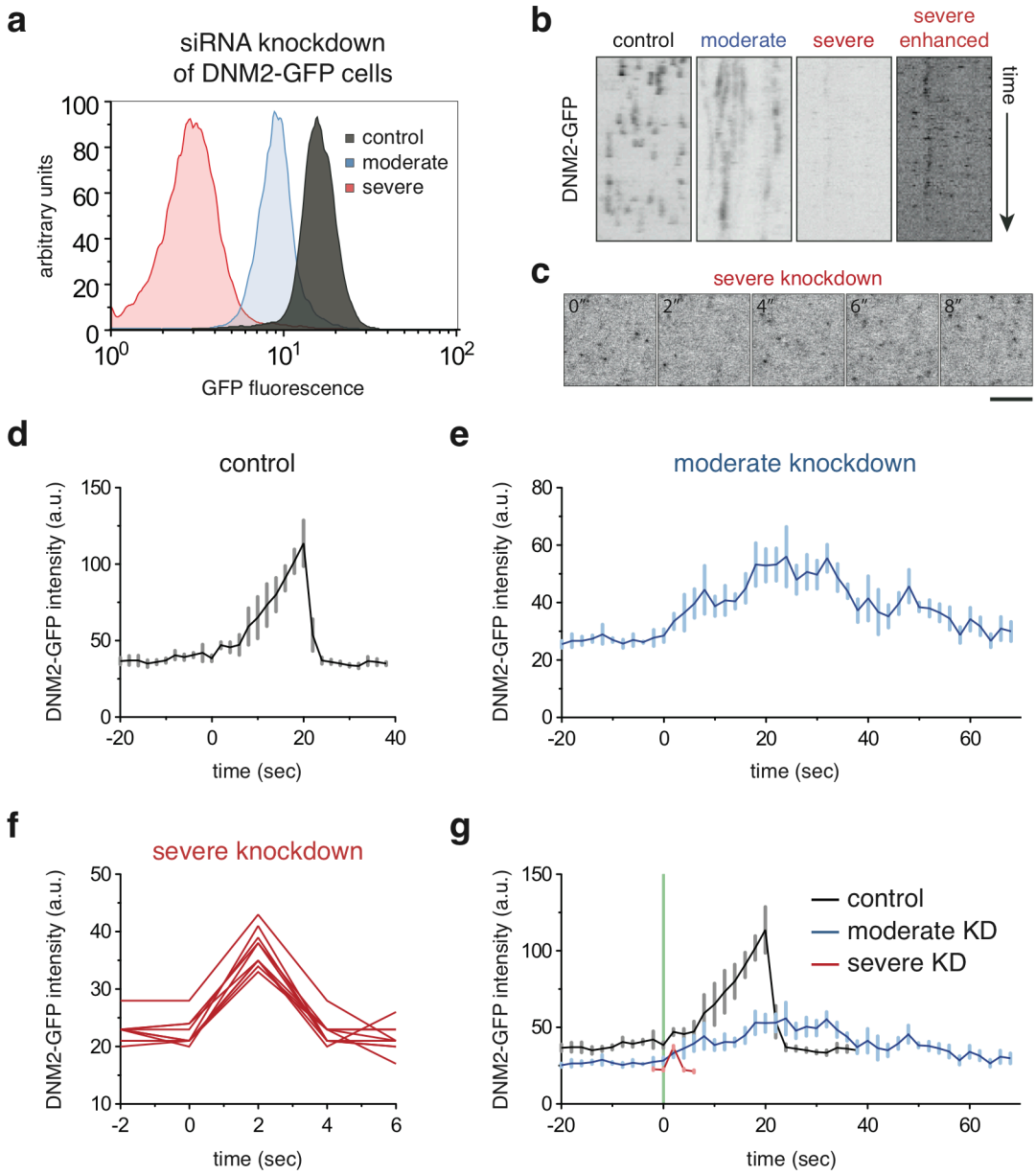
a
siRNA knockdown
of DNM2-GFP cells
arbitrary units
GFP fluorescence
control
moderate
severe
b
control
moderate
severe
severe
enhanced
DNM2-GFP
time
c
severe knockdown
0″
2″
4″
6″
8″
d
control
DNM2-GFP intensity (a.u.)
time (sec)
e
moderate knockdown
DNM2-GFP intensity (a.u.)
time (sec)
f
severe knockdown
DNM2-GFP intensity (a.u.)
time (sec)
g
DNM2-GFP intensity (a.u.)
time (sec)
control
moderate KD
severe KD

Figure 3.5 Concentration dependence of dynamin recruitment to endocytic sites. (a) Histogram plot of GFP fluorescence intensity for cell populations collected by fluorescence-activated cell sorting (FACS). Cells were subjected to mock or siRNA depletion against GFP and sorted 3 days post-treatment by FACS for moderate or severe DNM2-GFP knockdown (# cells analyzed = 24,467 (control), 29,711 (moderate), and 16,286 events (severe)). (b) Representative kymograph analysis of cells subjected to varying degrees (control, moderate, or severe) of DNM2-GFP depletion. Enhanced = increased contrast of severe depletion condition. Time, 180s. (c) Representative montage of a region of cell subjected to severe dynamin depletion. Contrast of images enhanced for better visualization. Time, 2s/frame. Scale bar, 5μm. (d-f) Average DNM2-GFP fluorescence intensity (± S.E.M.) profiles for cells subjected to varying degrees of dynamin depletion. (g) Overlay of (d) - (f). Green line denotes initiation of DNM2-GFP recruitment.

DISCUSSION

Here, we used genome editing technology coupled with quantitative fluorescence microscopy to examine the kinetics of dynamin recruitment to individual endocytic sites in live cells. Detailed analyses revealed that dynamin's recruitment profile is highly regular despite the variability in clathrin lifetimes for associated events. Active turnover and remodeling of actin filaments regulates early dynamin recruitment, whereas actin polymerization is required for vesicle scission and clathrin uncoating, suggesting that actin may contribute to both the regulatory and mechanical function of dynamin in CME. Additionally, modulation of dynamin concentration influences its behavior at endocytic sites, implying that dynamin function is, in part, self-regulating.

Previous reports proposed a rate-liming, mechanistic role for dynamin at early stages of endocytosis (Sever *et al*., 2000; Loerke *et al*., 2009). And recently, Merrifield and colleagues proposed that actin may serve to scaffold the early clathrin bud, thereby stabilizing and promoting dynamin recruitment (Taylor *et al*., 2012). Stabilization of actin filaments with jasplakinolide markedly decreased the fluorescence of dynamin punctae to low levels, similar to those of the initial low-amplitude 'flickering' phase observed by us and others (Sever *et al*., 1999, 2000; Mettlen *et al*., 2009; Loerke *et al*., 2009; Taylor *et al.,* 2012). We believe that this suggests that active actin filament turnover, presumably in remodeling of the proposed actin scaffold, is necessary to support and concentrate dynamin at endocytic sites. Intriguingly, there is precedent for short actin filaments in promoting assembly of dynamin into higher order structures *in vitro* (Gu *et al*., 2010). For future studies, it will be important to see if this mechanism of dynamin assembly is observed *in vivo* and for modulation of endocytosis. Alternatively, the impairment of continued dynamin recruitment may be a consequence of blocking the invagination in such a way in which the CCP topology does not support additional dynamin binding. Another model is that cortical actin meshworks of some cell types may physically impair CCP invagination, as first proposed in the earliest observation of clathrin dynamics (Gaidarov *et al*., 1999); actin-depolymerizing drugs (such as latrunculins) may relax such restrictions. Our observation that dynamin recruitment is impaired when actin is stabilized by jasplakinolide is congruent with this hypothesis.

Even more well documented is dynamin's role in mediating membrane scission and vesicle release (Takei *et al*., 1999; Macia *et al*., 2006; Pucadyil and Schmid, 2008; Loerke *et al*., 2009; Sever *et al*., 1999, 2000; Mettlen *et al*., 2009; Ramachandran *et al*., 2009; Liu *et al*., 2013). We therefore used the signature 'burst' of dynamin recruitment, indicative of a membrane scission, as a marker for endocytic productivity. Nearly all clathrin punctae greater than 20 seconds had this signature, which was near completely absent in punctae less than 20 seconds. Moreover, for clathrin punctae > 20 seconds, dynamin intensity profiles were highly regular regardless of clathrin lifetime. These findings suggest that endocytic pits must mature sufficiently in order for events to proceed irreversibly towards completion. This is congruent with the idea that a minimum threshold (e.g., cargo or otherwise) must be satisfied to avoid CCP abortion and disassembly (Loerke *et al*., 2009). The regularity of dynamin recruitment in these cells is also reminiscent of the regularity displayed during late stages of endocytic invagination

(i.e., the fast, inwardly-motile, and irreversible internalization phase) in budding yeast. The variability in clathrin lifetimes of mammalian cells is also mirrored in budding yeast, where there is heterogeneity in the dynamics of proteins arriving during early stages of endocytosis. These similarities point to a high degree of conservation in the mechanism(s) that drive endocytic internalization in eukaryotes.

Acute actin filament disassembly using depolymerizing latrunculin and cytochalasin drugs caused a dose-dependent impairment of dynamin dynamics at endocytic sites. With increasing drug concentration, the rate of dynamin recruitment and de-recruitment decreased, suggesting that actin polymerization promotes efficient accumulation and disassembly of dynamin. In budding yeast, LatA exposure or deletion of the yeast homologue of the mammalian actin-binding endocytic protein Hip1R, Sla2p, completely blocked endocytic internalization, supporting the conclusion that actin polymerization directly pushes membrane invaginations inward (Kaksonen *et al*., 2003). Indeed, in mammals, cells lacking dynamin (derived from dynamin1/2 double conditional knockout mice) displayed arrested clathrin-coated pits with long tubular necks decorated with actin (Ferguson *et al*., 2009). Perhaps dynamin recruitment to endocytic sites increases concomitantly with the maturation state of pits. For future studies, it would be informative to correlate the observed patterns of protein recruitment with CCP topology, as has been done in yeast (Kukulski *et al*., 2011, 2012). Dynamin GTPase activity has also been shown capable of modulating the recruitment of actin to endocytic sites (Taylor *et al*., 2012). We believe that either mechanism, singly or together, are plausible to promote efficient dynamin accumulation.

Traditional methods for monitoring protein dynamics under depletion conditions require the simultaneous knockdown of the endogenous protein target and the concurrent ectopic over-expression of the fluorescently labeled protein derivative. The heterogeneity in both knockdown and over-expression makes it difficult to perform well-controlled investigations on the effects of protein concentration on protein behavior. The ability to directly integrate a fluorescent marker at genomic sites via ZFNs allowed us to monitor dynamin behavior when expressed at low, moderate, or steady-state protein levels. Structural studies on dynamin have proposed that membrane scission is driven by dynamin tetramerization and higher-order self-assembly into rings on membranes (Ramachandran *et* al., 2007; Chappie *et al.,* 2010; Shnyrova *et al.,* 2013). The prolonged lifetime of dynamin in cells moderately depleted of dynamin protein (Figure 3.5) could partially be due to the slower formation of a productive dynamin spiral. Severe depletion of dynamin resulted in loss of its signature burst of accumulation, and the resulting events were dim and short-lived events. Together with the previous observation that dynamin regulates actin recruitment, we believe this finding suggests that dynamin must be at sufficient levels for it to be efficiently captured at endocytic sites for mediation, via actin, of coated-pit maturation.

The findings presented here illustrate that dynamin function in CME is regulated both by actin and by its own concentration. The major challenges ahead are to unravel the mechanism(s) by which dynamin concentration controls dynamin targeting and to precisely understand how actin remodeling controls dynamin placement and function at sites of endocytosis.

SUMMARY

In mammalian cells, there has been much debate and controversy over the necessity of actin in driving clathrin-mediated endocytosis. In budding yeast, abrogation of actin or actin-binding proteins acutely and completely halts membrane invagination. The role of actin is less clear in mammals, wherein some cell types are sensitive to perturbations by actin drugs, while others are not. The conflicting reports have therefore made it difficult to form a unifying picture of how actin participates in endocytosis.

Here, we utilized genome editing to engineer mammalian cells expressing endogenous levels of proteins belonging to the actin and endocytic machineries with the goal of defining more precisely the roles of dynamin and actin, and their mechanism(s) of interaction, in CME. Accumulating evidence suggests a model wherein at early stages of endocytosis, dynamin is slowly recruited to endocytic sites, and at late stages, dynamin accumulation is rapid, the assembly of which is augmented by actin in a forward-feeding manner, thereby making invagination directional and conclusive. Simultaneous imaging of dynamin and actin and unbiased global analysis of endocytic events revealed that dynamin is only robustly recruited to clathrin punctae having lifetimes greater than 20 seconds. The absence of dynamin localization to these short-lived clathrin punctae suggests that these CCPs do not undergo scission, and are therefore non-productive. This observation lends support to the existence of abortive endocytic sites, as previously proposed, but this is difficult to test, leaving unclear the function of this class of clathrin-associated membrane events. Our study also reveals a role for actin filament turnover in driving dynamin accumulation during early stages of endocytosis, and actin polymerization during late stage CCP maturation and membrane scission. Lastly, proper dynamin function necessitates precise regulation of its concentration; an increasing local concentration of cytosolic dynamin is required with each progressive stage of endocytosis. Collectively, these findings illustrate the intricacy and complexity of this regulated pathway.

MATERIALS AND METHODS

ZFN design. Enhanced obligate heterodimer (eHF) ZFNs (ZFN 55 and 56) designed to target +/- 50 bp of the start codon of ACTB were generously provided by Sigma Life Sciences (St. Louis, MO). ZFNs were prescreened for activity in K562 cells using Surveyor nuclease (Cel-1, Transgenomic, Omaha, NE) to detect for insertions or deletions (Urnov *et al*., 2005). Briefly, Accuprime Taq HiFi (Invitrogen, Carlsbad, CA) was used to amplify a short region surrounding the ZFN- target site in a 28-cycle PCR. Resulting amplicons were denatured, slowly re-annealed, and treated with Cel-1 for 20 min at 42°C, then separated on 10% criterion gels (Bio-Rad, Hercules, CA) and visualized by ethidium bromide staining.

Out-out PCR to detect targeted integration at CLTA and DNM2. PCR was used to screen SK-MEL-2 clones that were RFP-positive after FACS enrichment. For the initial pre-screening of clones, 2 µl of genomic DNA prepared using QuickExtract (Epicentre Biotechnologies, Madison, WI) was amplified in a 35-cycle Accuprime Taq HiFi (Invitrogen, Carlsbad, CA) PCR. An extension time of 10 min was used to minimize bias against the tagged allele(s) of the targeted gene. PCR products were analyzed on 5% criterion gels (Bio-Rad, Hercules, CA) that were run for 3-4 h at 150 V and visualized with ethidium bromide. Positive clones were then reanalyzed independently using genomic DNA prepared with the Masterpure kit (Epicentre Biotechnologies, Madison, WI) in 30-cycle PCRs with 100 ng template DNA. The resulting amplicons were analyzed by PAGE as described above. Clones suitable for further analysis were identified by cloning the out-out PCR products into pCR2.1 TOPO (Invitrogen, Carlsbad, CA) and conventional sequencing.

Cell culture. SK-MEL-2 cells were purchased from the ATCC and hCLTA^{EN}/hDNM2^{EN} and hDNM2^{EN-1} cells were derived as previously described (Doyon *et al*., 2011). All cells were maintained under 5% CO_2 at 37°C in DMEM/F-12 (Invitrogen, Carlsbad, CA) supplemented with 10% FBS (HyClone, Logan, UT).

Donor Design. A donor plasmid carrying Tag-RFP fused to the N-terminus of the ACTB gene (CellBio 770; Sigma Life Sciences, St. Louis, MO) was subjected to site-directed mutagenesis by Quikchange (Agilent Technologies, Santa Clara, CA). Specifically, to confer increased fluorophore photostability, the Tag-RFP marker was mutated to Tag-RFP-t (see Shaner *et al.,* 2008) by mutation of Tag-RFP amino acid position 164 from serine to threonine (AGC->ACC).

Generation of genome-edited cell lines. ZFN and donor plasmids were transfected into cells using a single cuvette Amaxa Nucleofector device (Lonza, Basal, Switzerland), as per the manufacturer's protocol. In brief, cells grown to ~80% confluency were harvested by trypsinization, and 1-1.5 x 10^6 SK-MEL-2 cells were resuspended in Nucleofector solution R and transfected using Nucleofector program T-020. After transfection, cells were transferred to 37ºC, 5% CO_2. Recovered cells were sorted for

RFP-positive or RFP- and GFP-positive signals using a DAKO-Cytomation MoFlo High Speed Sorter directly as single cells into 96-well plates.

Total internal reflection fluorescence (TIRF) microscopy and live-cell imaging. TIRF microscopy images were captured using MetaMorph software on an Olympus IX-81 microscope using a 60x/NA1.49 objective and an ORCA-R2 camera (Hamamatsu, Japan). The system was maintained at 37°C using a WeatherStation chamber and temperature controller (Precision Control, Tacoma, WA). At 16-24 hours prior to imaging, cells were seeded onto uncoated glass coverslips in growth medium. During imaging, cells were maintained in DMEM without phenol red that was supplemented with 5% FBS and 10 mM HEPES. A 488 nm solid-state laser (Melles Griot, Albuquerque, NM) and a 561 nm diode-pumped solid-state laser (Melles Griot, Albuquerque, NM) were used to excite GFP and RFP fluorophores, respectively. For lifetime analysis, images were acquired every 2 s for 3-6 min, with an exposure time of 800 ms. Simultaneous two-color TIRF images were obtained using a DV2 image splitter (MAG Biosystems, Santa Fe, NM) to separate GFP and RFP emission signals.

Drug perturbations. Cells were prepared as described for live-cell imaging. During real-time imaging, a 2-5X concentrated solution of actin drug in DMSO (cytochalasin D (Sigma-Aldrich, St. Louis, MO); jasplakinolide (Sigma-Aldrich, St. Louis, MO); latrunculin A (Sigma-Aldrich, St. Louis, MO) was applied to the imaging apparatus at a volume of 2-5 fold (in imaging media) over that of the starting imaging media volume.

siRNA-mediated knockdown. The day prior to transfection, $5.0x10^5$ cells were plated into each well of 6-well plates. Transfection was performed using Lipofectamine RNAiMax according to manufacturer's instructions (Invitrogen). Briefly, 5µl of transfection reagent was mixed with 250 µl of Opti-MEM (Gibco) for 15min at RT. After incubation, the solution was combined with 200pmole of siRNA previously diluted in 250µl Opti-MEM and incubated further for 15 min at RT. The combined solution was directly added to each well pre-aliquoted with 1.5 mL of growth media. A non-targeting siRNA pool (siRNA control; ON-TARGETplus SMARTpool siRNA #4, Dharmacon Thermo Scientific, Waltham, MA) and Ambion Silencer Select validated siRNA (5'-ACAUCAACACGAACCAUGA-3'; Life technologies, siRNA ID# s4212) against dynamin-2 were used for depletion experiments.

Fluorescence-activated cell sorting of dynamin-2 knockdown cells. Two days post siRNA transfection, cells were harvested by trypsinization and FACS sorted using a DAKO-Cytomation MoFlo High Speed Sorter. For each depletion condition (moderate or severe), at least $1.0x10^5$ cells were sorted for GFP intensity. The following criteria were used: 1) moderate depletion group = GFP intensity of approximately 20-50% relative to control and 2) severe depletion group = GFP intensity of approximately 0-25% relative to control. Cells were directly seeded onto glass coverslip in 6-well plates, maintained at 37°C, 5% CO_2 and imaged by TIRF microscopy 24 hours after sorting (72 hours post transfection).

Fluorescence staining of fixed cells. Cells were grown on glass coverslips in 6-well plates overnight before fixation in 4% paraformaldehyde at room temperature for 20 min. After three washes with PBS, the coverslips were quenched with 1 mg/ml $NaBH_4$ for 15 min twice, and the cells were permeabilized in 0.1% saponin/PBS or 0.1% Triton X-100/PBS. After brief washing with PBS, the coverslips were incubated with Alexa Fluor 350 conjugated phalloidin (Molecular Probes) at 1:1000 dilution for 2 hr at room temperature. After three washes with PBS, the coverslips were mounted on glass slides using ProLong Gold antifade reagent or visualized directly (Invitrogen, Carlsbad, CA).

Particle detection, tracking, and image analysis. Particle detection and tracking were performed using Imaris 7.1 software (Bitplane Scientific, Zurich, Switzerland). Prior to particle detection, images were first subjected to background subtraction. The Spots module of Imaris was then used to automatically detect point-like particles with an estimated spot diameter of 500 nm (~5 pixels). After automatic detection, detected spots were filtered based on satisfying minimum 'intensity standard deviation' and 'quality' control parameters. Only spots with values higher than the set threshold values were considered for analyses. Quality is defined as the intensity at the center of the spot, Gaussian filtered by ¾ of the spot radius. Appropriate threshold values were confirmed by visual inspection of correct particle detection. To trace objects through sequential frames of time data, a Brownian motion particle-tracking algorithm was applied. A maximum search distance of 350 nm was defined to disallow connections between a Spot and a candidate match if the distance between the predicted future position of the Spot and the candidate position exceeded the maximum distance. A gap-closing algorithm was also implemented to link track segment ends to track segment starts to recover punctae that were interrupted by the temporary disappearance of particles. The maximum permissible gap length was set equal to 7 frames. Track outputs were then visually inspected and, as necessary, edited to correct for tracking errors. Only punctae that appeared and disappeared during the lifetime of the acquisition (i.e., 181 frames, 6 minutes) were subjected to lifetime analyses.

Statistical analysis. Paired or un-paired two-tailed t-tests were used to assess for significance. All tests were performed using GraphPad Prism (La Jolla,CA) and data are presented as mean ± standard error of the mean (S.E.M), unless otherwise indicated.

CHAPTER 4:
Pluripotent stem cells as a developmental system for studying endocytosis

INTRODUCTION

Live-cell imaging studies of clathrin-mediated endocytosis (CME) have revealed broad heterogeneity in the lifetimes, mobility, and size of clathrin-coated plasma membrane events (Gaidarov *et al.*, 1999; Merrifield *et al.*, 2002; Ehrlich *et al.*, 2004; Saffarian *et al.*, 2009). African green monkey BSC-1 cells display predominantly canonical clathrin-coated pits (CCPs) that rapidly assemble and internalize, whereas, other cell lines (e.g., SKMEL-2, HeLa) exhibit both CCPs as well as larger and more stable clathrin-coated structures (CCSs)(Ehrlich *et al.*, 2004; Saffarian *et al.*, 2009). While several studies have begun to address the molecular underpinnings of this variability, why different cell lines exhibit varying dynamics and how this is achieved remain unknown (Liu *et al.*, 2009; Boulant *et al.*, 2011; Nunez *et al.*, 2011). Moreover, how disease (e.g., microbial infection, cancer) might alter the endocytic dynamics of normal cells is unclear. Here, I describe an ideal system, one that couples zinc finger nuclease (ZFN) or transcription activator-like effector nuclease (TALEN) genome editing technology with use of human pluripotent cells, to investigate these questions.

This system overcomes two major limitations of current methodologies. First, current gene expression methods in mammalian cells dictate that fluorescent fusion proteins used for live-cell studies be overexpressed from exogenously introduced transgenes. This strategy presents several critical challenges as it (1) fails to preserve protein expression at native levels, which can result in protein mislocalization, aggregation, and altered signaling, and (2) forces overexpression of a single protein isoform, which can result in unintended downregulation of related proteins (Miyama et al., 1999; Luo *et al.*, 2001; Kuma *et al.*, 2007; Knoop *et al.*, 2008; Liu *et al.*, 2008; Ferguson *et al.*, 2009). Indeed, we recently showed that genome-edited somatic cells exhibit enhanced endocytic function, dynamics and efficiency when compared with overexpression-derived cells, indicating that CME is highly sensitive to the levels of its protein components (Doyon *et al.*, 2011). Use of ZFN-mediated genome editing will allow us to create embryonic stem cells that stably express physiological levels of fluorescent protein fusions for study of protein dynamics.

Second, much of our knowledge about CME dynamics has relied on the use of malignant cells (i.e., viral transformed, cancerous, and/or aneuploid)(Gaidarov *et al.*, 1999; Merrifield *et al.*, 2002; Ehrlich *et al.*, 2004; Liu *et al.*, 2009; Saffarian *et al.*, 2009). This is problematic since it is well known that cancer cells have a physiology far removed from that of normal cells in tissue. In fact, the most widely used cell line for studies of CME, BSC-1, carries an average of 60 chromosomes, with 3 copies of clathrin and dynamin genes (Merrifield *et al.*, 2005; Loerke *et al.*, 2009; *Saffarian et al.*, 2009; Liu *et al.*, 2009; Nunez *et al.*, 2011; Boulant *et al.*, 2011; Doyon *et al.*, 2011). Since the effect of these malignancies on the function and regulation of CME remains unresolved, and because defects in endocytosis have been reported to contribute to disease, continued use of these cell lines limits our ability to fully and faithfully understand CME (Conner and Schmid, 2003; Ferguson and De Camilli, 2012).

Human pluripotent stem cells (hPSCs) possess normal karyotype and are unique in their inexhaustible ability to divide and renew, and under the appropriate conditions,

differentiate and change into any cell type. While traditional cell lines are well suited for investigating what cells have in common, the differentiating capacity of pluripotent cells makes their use ideal for addressing questions about cellular diversity (i.e., differences between cell types). This system will enable us to elucidate the dynamics of endocytic proteins, both in pluripotent and differentiated cell states, and will allow us to probe whether different cell types do indeed possess different endocytic behaviors. If endocytic protein dynamics should change upon cellular differentiation, the system will afford the ability to dissect through ontogeny the mechanisms and functional relevance of any changes.

To monitor native endocytic dynamics, I derived both human embryonic stem cell (hESC) and human induced pluripotent stem cell (hiPSC) lines that stably express a C-terminal fluorescent protein fusion of clathrin light chain A (CLTA) from its endogenous locus. I performed real-time total internal fluorescence microscopy (TIRF-M) analyses of these cells in pluripotent and differentiated states. Using this method, I describe how clathrin-mediated endocytosis operates in naïve cells, how this process changes upon cellular differentiation, and elucidate cellular components that in part contribute to these changes.

RESULTS

ZFN-mediated insertion of RFP at the *CLTA* locus in hESCs

To engineer hESCs in which one *CLTA* allele was tagged with red fluorescent protein (RFP), I used ZFNs to introduce double-strand breaks at the 3′-terminus of the human clathrin light chain A gene (CLTA; Figure 4.1a)(Doyon *et al*., 2011). I delivered ZFN expression constructs and corresponding donor plasmids bearing homologous sequences into H9 hESCs (Figure 4.1a)(Thompson *et al*., 1998) by electroporation.

I took advantage of the fluorescent nature of the marker to enrich for cells by fluorescence-activated cell sorting without drug selection. Analysis of ZFN-targeted cells revealed a population of cells, comprising >6% of the total pool, that exhibited RFP fluorescence. This percentage is likely higher as the efficiency of reagent delivery in H9 hESCs is only 50-70% (Figure 4.1b). Notably, as compared to hESCs overexpressing CLTA-RFP, this genome-edited population displayed a distinctly lower degree of variation in CLTA-RFP fluorescence (Figure 4.1b). RFP-positive cells were sorted directly into 96 wells, as single-cells, for clonal derivation. PCR and Sanger sequencing analysis of a RFP-positive clone (henceforth referred to as H9.CLTA-RFP) confirmed precise and accurate integration of the marker at a single CLTA allele (Figures 4.1c, d). Despite these manipulations, this clone remained pluripotent based on expression of the hallmark stem cell nuclear transcription factor, Oct-4 (Figure 4.1e).

ZFN-mediated insertion of RFP at the *CLTA* locus in hiPSCs

To establish the generality of this targeting strategy, I used the same approach as for H9.CLTA-RFP derivation to engineer genome-edited hiPSCs (feeder-dependent #38 line and feeder-independent WT-C line) expressing CLTA-RFP from their endogenous loci. FACS analysis showed that both lines were targeted with similar efficiencies (1-2%), albeit lower than was obtained for H9 hESCs (Figure 4.2a). Employing FACS afforded enrichment by 45-fold, with nearly 90% of isolated clones targeted in one or both alleles, which is similar to targeting efficiencies we achieved in somatic cells (Figure 4.2b and Table 4.1). Lastly, sequencing confirmed accurate and precise addition of the marker (Figure 4.2c). Collectively, these data demonstrate the feasibility of this strategy for genome manipulation in human pluripotent stem cells.

Endocytic dynamics of CLTA-RFP in H9.CLTA-RFP hESCs

As a first step towards determining the dynamics of endocytosis in pluripotent stem cells, I used wide-field fluorescence microscopy to examine the localization and distribution of CLTA-RFP in the H9.CLTA-RFP clone. As expected, CLTA-RFP displayed punctate plasma membrane and perinuclear distribution, indicating that the endogenously tagged CLTA is correctly incorporated into clathrin-coated pits (CCPs)(Figure 4.3a). Moreover, ESC colonies displayed RFP fluorescence in all cells, suggesting that CLTA tagging is not sufficiently detrimental to endocytic function to warrant selective pressure for its exclusion (Figure 4.3b).

I next used total internal reflection fluorescence microscopy (TIRF-M), a highly sensitive method for visualization of ventral plasma membrane events, to monitor the

Figure 4.1

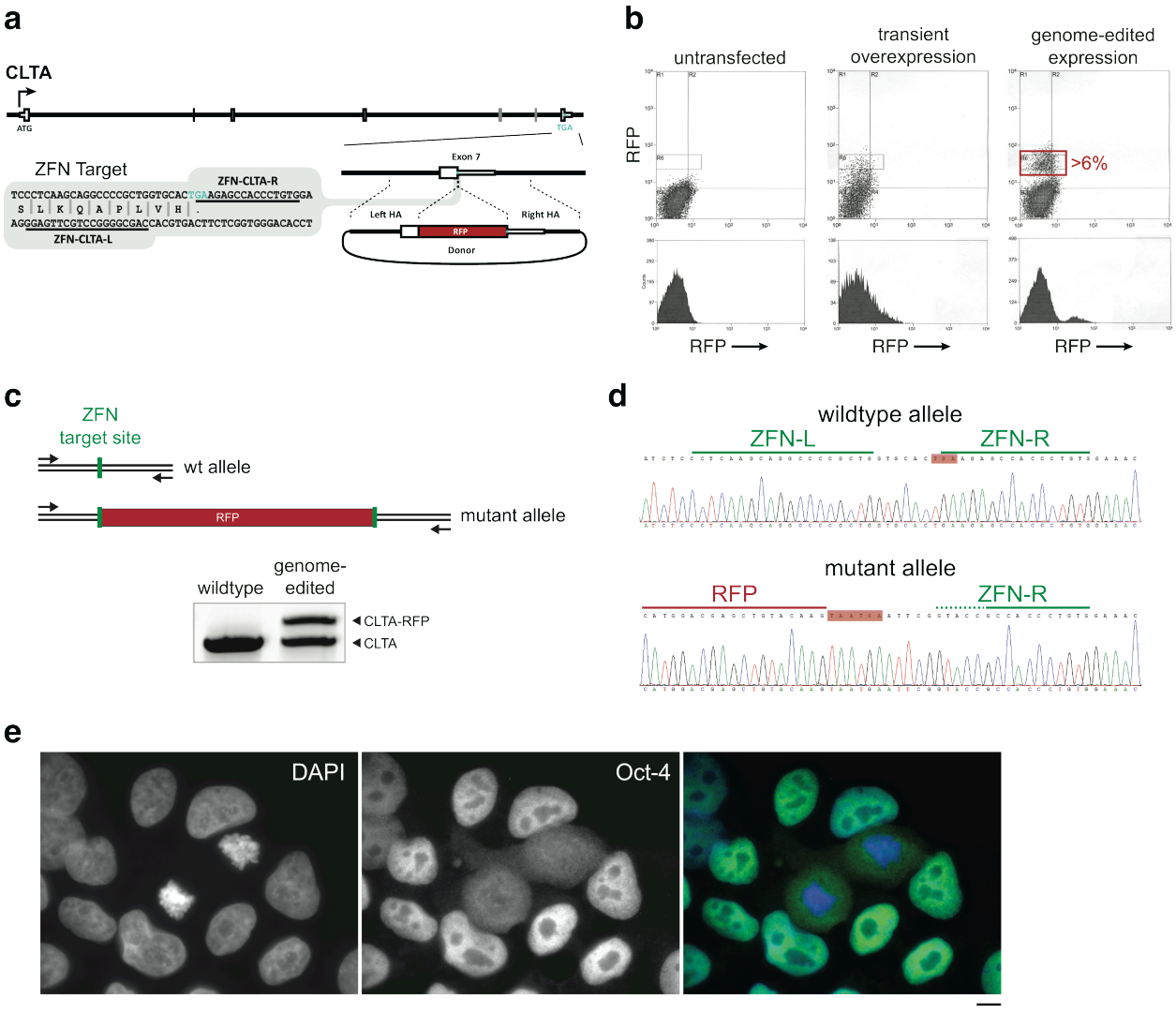

Figure 4.1 Editing of CLTA using ZFNs in hESCs. (a) Schematic overview depicting the targeting strategy for integration of RFP at the CLTA locus. White boxes, exons of CLTA. HA, donor plasmid region of homology to CLTA sequence. Blue letters, stop codon. (b) FACS analysis of ZFN-targeted H9 hESCs illustrating a distinct RFP-positive genome-edited hESC population. (c) Schematic of out-out PCR genotyping assay (above) and genotype of H9.CLTARFP clone (below). Arrows indicate primers; Wildtype, parental cell line; genome-edited, single-allele tagged H9.CLTA-RFP hESC clone. (d) Representative H9.CLTA-RFP hESC sequence genotyping of the *CLTA* alleles. Red boxes, stop codon. (e) Immunostaining analysis of the H9.CLTARFP clone. Fixed cells were stained for octamer-binding transcription factor 4 (Oct-4) and DNA (using DAPI) and visualized by epi-fluorescence microscopy. Scale bar, 10 μm.

Figure 4.2

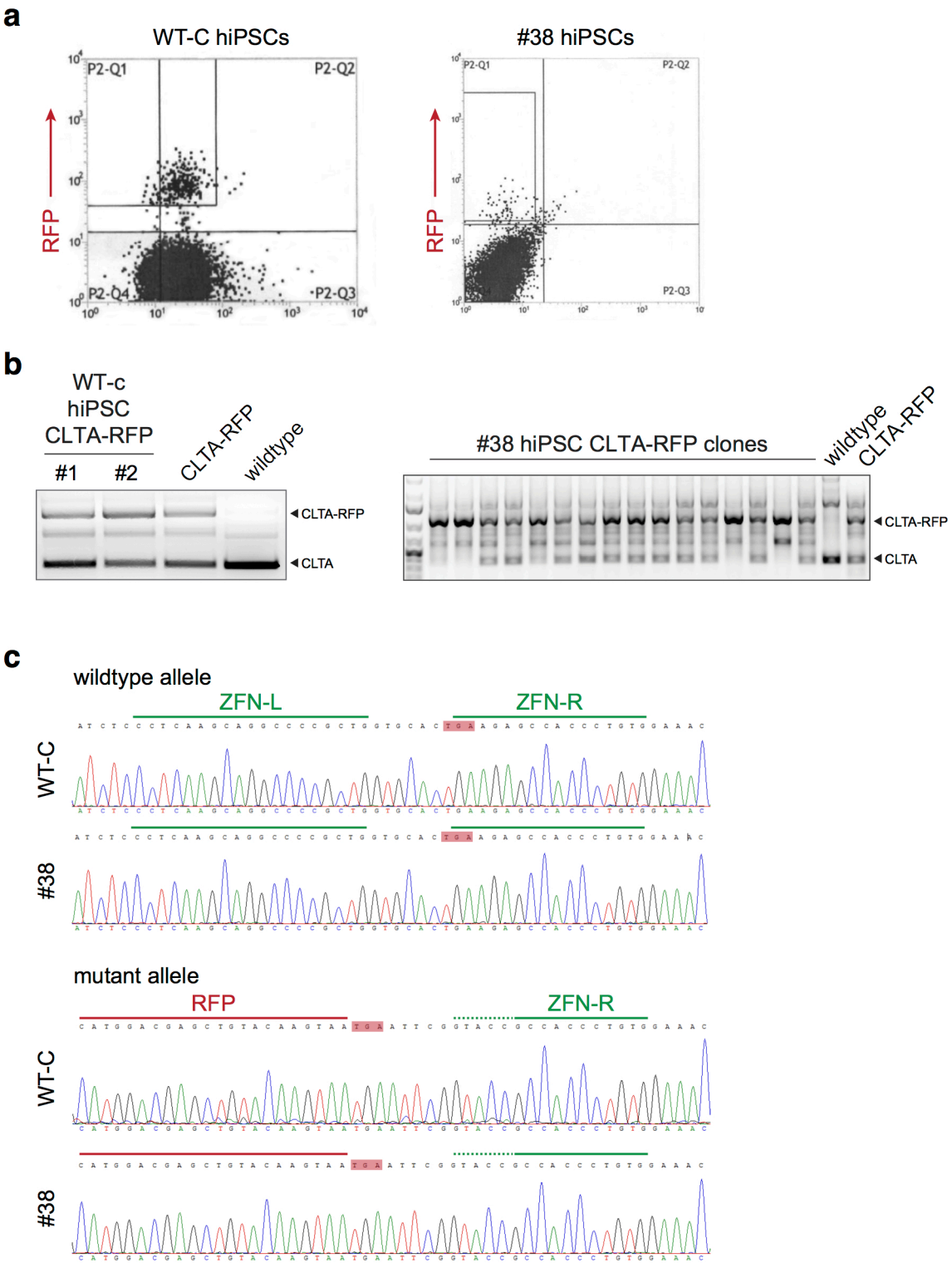
a
WT-C hiPSCs
#38 hiPSCs
P2-Q1
P2-Q2
P2-Q3
P2-Q4
RFP
b
WT-c hiPSC CLTA-RFP
#1
#2
CLTA-RFP
wildtype
CLTA-RFP
CLTA
#38 hiPSC CLTA-RFP clones
wildtype
CLTA-RFP
CLTA-RFP
CLTA
c
wildtype allele
ZFN-L
ZFN-R
WT-C
#38
mutant allele
RFP
ZFN-R
WT-C
#38

Figure 4.2 Editing of CLTA using ZFNs in hiPSCs. (a) FACS analysis of ZFN-targeted hiPSCs (#38 and WT-C lines). (b) Representative editing efficiency using FACS enrichment. hiPSCs were enriched by FACS and individual clones were selected from colonies in 6-well or 96-well plates. Clones were isolated by out-out PCR for CLTA using the oligos listed in Table 2.5 as “Cel-1”. Two isolated WT-C clones (left) and 16 randomly isolated #38 clones of the total 35 that were genotyped are shown. (c) Representative hiPSC sequence genotyping of the *CLTA* alleles. Red boxes, stop codon.

Table 4.1

#38 hiPS cells

Genotype	# of clones	% of total clones
wild-type	4/35	11
transheterozygote	24/35	69
homozygous mutant	7/35	20

SK-MEL-2 cells

Genotype	# of clones	% of total clones
wild-type	8/35	16
transheterozygote	28/50	56
homozygous mutant	14/50	28

Table 4.1 Targeting efficiency of pluripotent versus somatic cells post-FACS enrichment

Figure 4.3

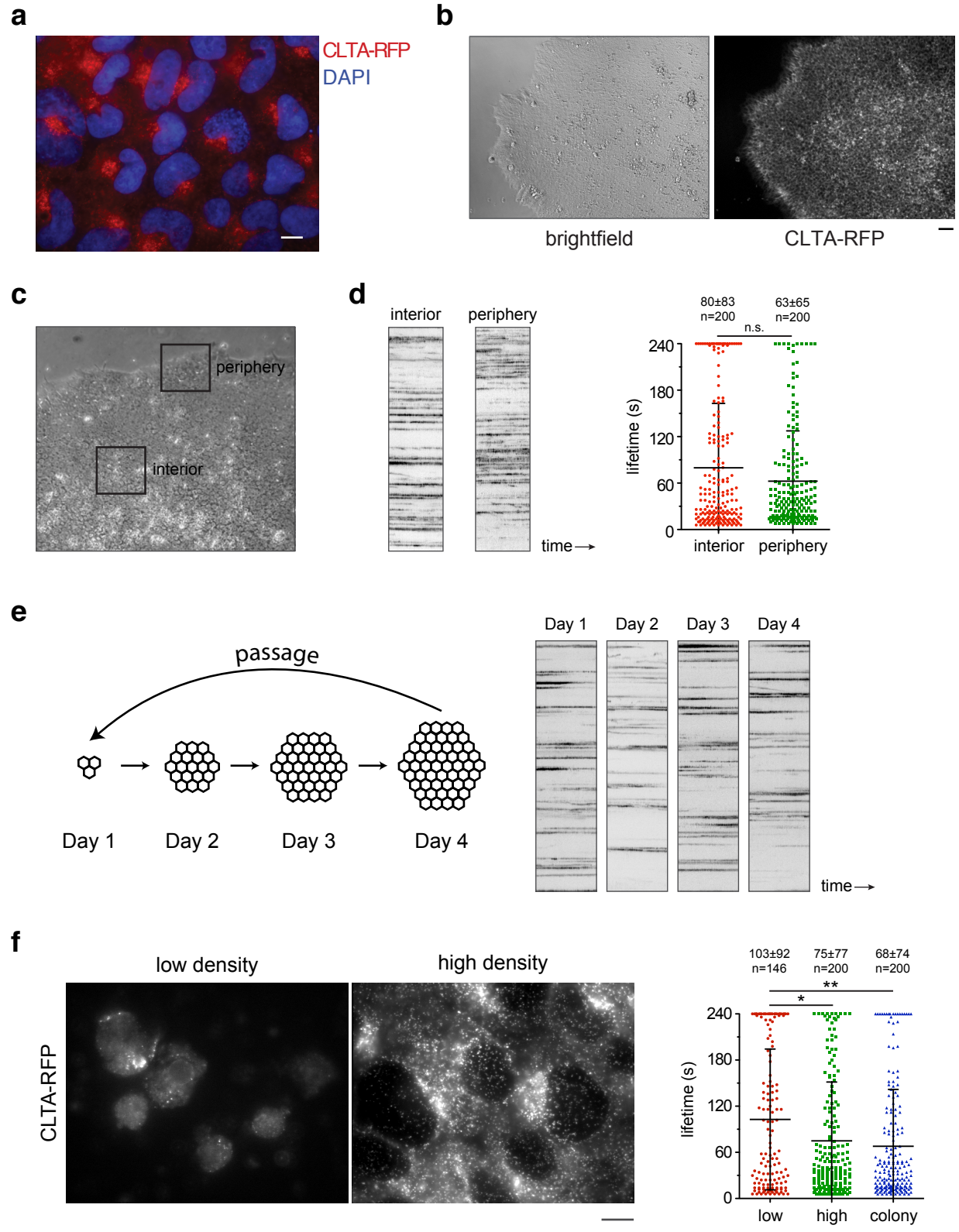
a
CLTA-RFP
DAPI
b
brightfield
CLTA-RFP
c
periphery
interior
d
interior
periphery
time
80±83
n=200
63±65
n=200
n.s.
lifetime (s)
240
180
120
60
0
interior
periphery
e
passage
Day 1
Day 2
Day 3
Day 4
time
f
low density
high density
CLTA-RFP
103±92
n=146
75±77
n=200
68±74
n=200
**
*
lifetime (s)
low
high
colony

Figure 4.3 Fluorescence microscopy analysis of the H9.CLTA-RFP hESC line. (a and b) Epifluorescence image of (a) cells or (b) stem cell colony expressing endogenous CLTA-RFP. Scale bar, 10 μm or 50 μm, respectively. (c) Brightfield microscopy image of a representative stem cell colony with interior or periphery regions demarcated in black. (d) CLTA-RFP kymograph analyses (left panel) and scatter plot of lifetime for individual CLTA-RFP events in cells at the colony interior or periphery (right panel). Time, 240 s. Each dataset represents mean ± s.d. ($P = 0.5368$). *n*, number of events analyzed. n.s., no statistical significance. (e) Schematic of passaging regime (left panel) and kymograph analyses of CLTA-RFP in cells at days 1-4 post-passaging (right panel). Time, 240 s. (f) Epifluorescence image of cells dissociated to single-cell suspension and seeded at low or high density (left panel) and scatter plot of lifetime for individual CLTA-RFP events in cells seeded at low or high density or as an ESC colony (right panel). Each dataset represents mean ± s.d. ($*P < 0.05$, $**P < 0.005$). *n*, number of events analyzed. Scale bar, 10 μm.

dynamics of CLTA-RFP. Surprisingly, CLTA-RFP punctae displayed a high degree of heterogeneity, displaying both CCPs (diffraction-limited punctae which rapidly assemble and internalize) and CCSs (larger, sometimes displaying as clusters, and long-lived (typically over >120s), a characteristic reminiscent of many cancer cell lines (Figure 4.3d). Moreover, many endocytic sites were long-lived (>200sec), with 7% of the total population displaying lifetimes exceeding the length of imaging (time = 240s; Figure 4.3d). Why cells display such persistent CLTA-RFP membrane localization is unclear.

H9 hESCs grow tightly together as a monolayer, forming a cell colony. As such, I wondered whether the endocytic dynamics of cells at the periphery of colonies might differ from those more interior (Figure 4.3c). Global analysis of CLTA-RFP punctae in different cells revealed long-lived events with no significant difference in lifetime between interior and peripheral cells (80 ± 83 sec and 63 ± 65 sec, respectively, n = 200, P = 0.54; Figure 4.3d).

Routine propagation of hESCs requires the breakdown of large colonies into smaller clumps that, upon substrate attachment, expand radially outward with time. To investigate whether endocytic dynamics might change depending on colony size, I examined CLTA-RFP dynamics at days 1-4 post-passaging (Figure 4.3e, left panel). Regardless of colony size, cells showed no significant change in CLTA-RFP lifetime (Figure 4.3e, right panel). Collectively, these data suggest that the location of a cell within an ESC colony and colony size, at least at steady state, does not influence endocytic behavior.

The overwhelming majority of studies on endocytic dynamics have been performed on individual cells sparsely populated on a substrate (Kirchhausen, 2009; Loerke *et al.,* 2009; Boulant *et al.,* 2011; Doyon *et al*., 2012; Taylor *et al*., 2012). As such, I wondered whether the high cell density of ESC colonies might be a contributing factor to the observed prolonged CLTA-RFP lifetimes. To investigate this, I dispersed H9.CLTA-RFP colonies into single cells and seeded them at low or high density for imaging (Figure 4.3f). While the CLTA-RFP lifetimes of cells seeded at high density were not significantly different than cells within intact ESC colonies (75 ± 77 sec and 68 ± 74 sec, respectively; n = 200, P = 0.33), the CLTA-RFP lifetimes of cells seeded at low density (103 ± 92 sec; n = 146) were significantly longer than cells seeded at high density seed or in ESC colonies ($P < 0.05$ and $P < 0.005$, respectively). This illustrates that simply seeding cells sparsely does not decrease endocytic lifetime, and suggests that the prolonged CLTA-RFP lifetimes observed in the H9.CLTARFP clone may be an intrinsic property of pluripotent cells (Figure 4.3f). It will be important to derive additional H9.CLTARFP clones as well as perform analysis on the hiPS CLTA-RFP clones to test this hypothesis.

Substrate dependency of CLTA-RFP dynamics in hESCs

Certain cell types require specialized substrates to facilitate attachment for optimal growth and proliferation. Matrigel®, a gelatinous protein mixture derived from Englebreth-Holm-Swarm mouse tumor cells and comprised largely of laminin, collagen IV, and enactin, is used to support feeder-independent propagation of many stem cell lines, including the H9 line (Orkin *et al*., 1977; Ludwig *et* al., 2006; Hughes *et al*., 2010).

In contrast, cell lines traditionally used to study endocytic dynamics are seeded directly onto glass for imaging (Figure 4.4a). As such, I wondered whether Matrigel might influence CLTA-RFP behavior and contribute to the observed long-lived nature of these punctae. Unfortunately, the requirement of Matrigel for feeder-independent growth of ES cells, and the induction of apoptosis in its absence, precluded me from imaging H9.CLTA-RFP cells seeded directly on glass. I therefore sought to perform the inverse experiment to test whether endocytic dynamics of a genome-edited CLTA-RFP somatic cell line (SK-MEL-2 hCLTA^{EN-1}), would change upon growth on Matrigel (Doyon *et al*., 2011). Interestingly, CLTA-RFP lifetimes for cells seeded on Matrigel were significantly shorter than those seeded on glass (48 ± 63 sec or 59 ± 74 sec, respectively, $n = 200$, $P < 0.05$). We believe the gelatin-based substrate may have decreased the amount of tension imposed on the cell membrane, thus resulting in decreased CLTA lifetime, which is consistent with previous reports (Liu *et al.*, 2009; Batchelder and Yarar, 2010; Boulant *et al*., 2011). This shows that a Matrigel substrate alone does not directly increase CLTA-RFP lifetimes, and lends further support to the hypothesis that the prolonged nature of the endocytic sites in the H9.CLTA-RFP clone may be an intrinsic property of pluripotent cells (Figure 4.3b).

Actin-adhesion complexes contribute to CLTA-RFP dynamics in hESCs

There is increasing evidence supporting a role for actin in endocytosis (Kaksonen *et al*., 2005; Yarar *et al*., 2005; Saffarian *et al*, 2009; Boulant *et al*., 2011; Taylor *et al*., 2012). Reports have documented the presence of actin at endocytic sites, and the use of actin-perturbing drugs has revealed that actin acts at multiple steps in CME (see Chapter 3; Yarar *et al*., 2005; Taylor *et al*., 2012). There is also evidence to support the conclusion that long-lived CCSs are more dependent on actin for its internalization (Saffarian *et al*., 2009). Studies have also established a link between CME dynamics and adhesion structures. Localized modulation of cortical tension by fibronectin-patterned substrates have shown that endocytic dynamics increases in areas of increased adhesion density (Liu *et al*., 2009; Batchelder and Yarar, 2010). CME has also been directly implicated in the turnover of membrane adhesion complexes (Ezratty *et al*., 2006, 2009). These observations, collectively, led me to ask whether the long-lived CLTA-RFP structures of hESCs might be contributed by actin and/or membrane adhesions. Indeed, using immunostaining, I found that paxillin localizes in close proximity to these sites (Figure 4.4c).

Endocytic dynamics in cells differentiated from hESCs

Studies investigating endocytic dynamics have revealed variability in the behavior of endocytic proteins among different cell lines, suggesting that different cell types may adopt different cellular components to mediate CME (Kirchhausen, 2009; Loerke *et al.,* 2009; Boulant *et al.,* 2011; Doyon *et al*., 2012; Taylor *et al*., 2012). Unfortunately, the derived nature and use of traditional cancer cell lines precludes investigation of this hypothesis. To directly investigate if different cell types do indeed display different endocytic behaviors, I harnessed the differentiating capacity of hESCs to examine CLTA-RFP dynamics in cells differentiated from the H9.CLTA-RFP clone. Strikingly,

Figure 4.4

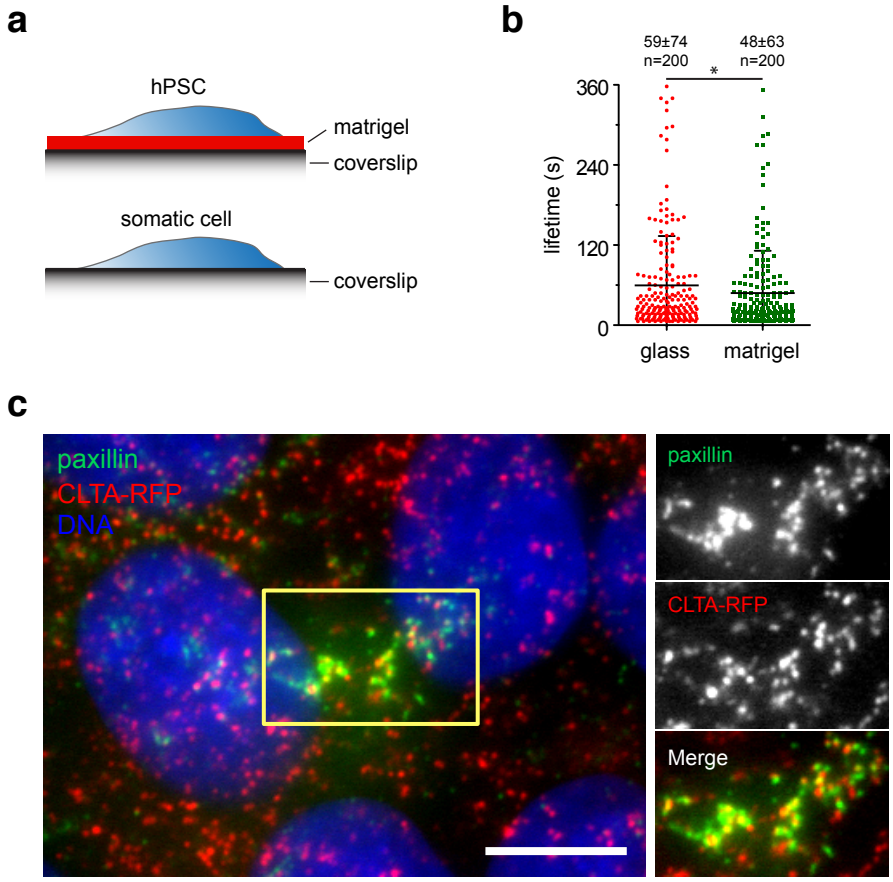

Figure 4.4 Substrate dependency of CLTA-RFP dynamics in hESCs. (a) Schematic representation of imaging modality highlighting differences in substrate preparation between hESC and somatic cell types. (b) Scatter plot of lifetime for individual CLTA-RFP events of SK-MEL-2 hCLTA^{EN} (Doyon *et al.,* 2011) cells grown on glass or Matrigel-coated coverslips. Each dataset represents mean ± s.d. (*= $P < 0.05$). *n*, number of events analyzed. (c) Epifluorescence microscopy image of H9.CLTA-RFP cells immunostained for the adhesion protein paxillin. Scale bar, 10 µm.

Figure 4.5

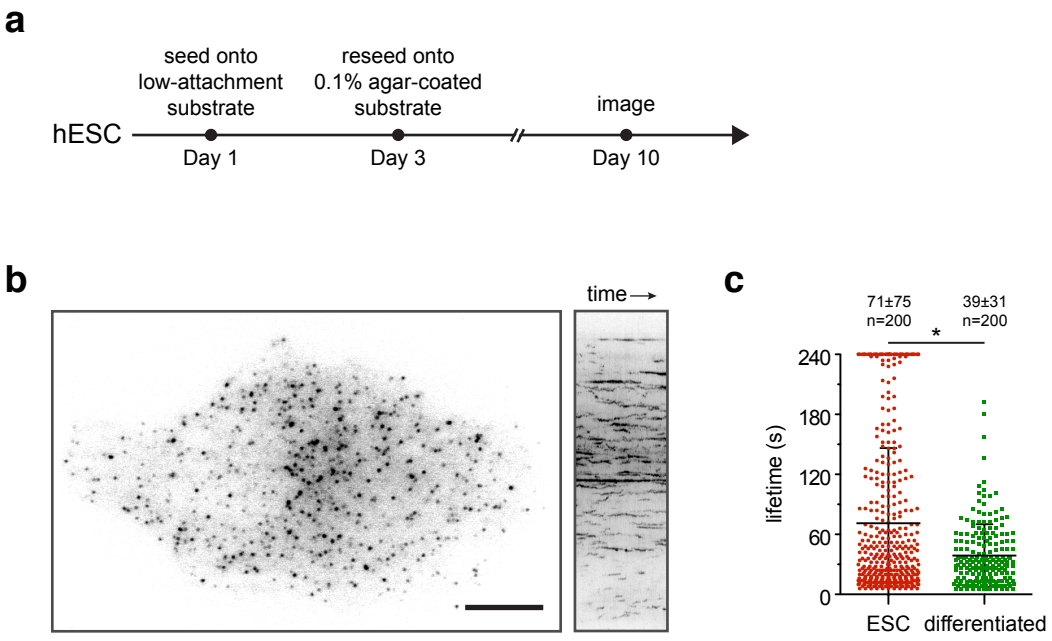

Figure 4.5 Endocytic dynamics of hESCs upon differentiation. (a) Schematic timeline of differentiation protocol. (b) TIRF microscopy image and kymograph analysis of CLTA-RFP in fibroblast-like cells differentiated from H9.CLTA-RFP hESCs. Scale bar, 10 µm. Time, 240 s. (c) Scatter plot of lifetime for individual CLTA-RFP events for H9.CLTA-RFP hESCs in ESC (embryonic stem cell) or differentiated cell states. Each dataset represents mean ± s.d. (*= $P < 0.001$). *n*, number of events analyzed.

fibroblast-like cells differentiated from hESC-derived embryoid body intermediates displayed highly dynamic CCPs with CLTA-RFP lifetimes significantly shorter than of their pluripotent counterpart (39 ± 31 sec and 71 ± 75 sec, respectively, $n = 200$, $P < 0.001$; Figure 4.5b, c).

DISCUSSION

Clathrin-mediated endocytosis is an exceedingly complex and dynamic process, one that requires the careful choreography of >50 molecular players at high spatiotemporal resolution. Its study, therefore, poses particular challenges for following the life history of individual events. Fortunately, through use of fluorescent proteins and live-cell microscopy, the field has made tremendous progress towards illuminating the key components and towards understanding the fundamental mechanisms that underlie this pathway. CME coordinates a range of activities (e.g., regulates the surface expression of proteins, samples the cells' environment for growth and guidance cues, and regulates signaling pathways) that together dictate cell function and fate. But how this pathway adapts in order to specify different cell types, and how it is altered when cells become diseased, is unclear.

In this study, I employed genome editing in pluripotent stem cells to establish a cell-culture system that would allow for investigation of endocytic dynamics in different cell types. I used fluorescence microscopy to monitor endocytosis in real-time and found that pluripotent cells display endocytic sites that are comparatively long-lived, relative to those observed in traditional cell culture lines, and that reside in close proximity to adhesions. While neither ES cell density, ES cell localization within a colony, nor growth substrate contributed to this phenotype, differentiation of ESCs into fibroblast-like cells caused a dramatic increase in the rate of endocytosis. Why are endocytic sites long-lived in pluripotent stem cells and why might their dynamics change upon cellular differentiation?

It has been shown that clathrin lifetime correlates positively with clathrin pit size (Ehrlich *et al*., 2004; Saffarian *et al*., 2009). A large body of work, moreover, has documented variation in the size of clathrin-coated pits, both across and within species. The smallest pits, at 35-60nm in diameter, are observed in yeast and plant cells (Dhonukshe *et al*., 2007; Smaczynska-de Rooij *et al*., 2010). In contrast, mammalian fibroblasts have clathrin-coated pits (CCPs) as large as 300nm (in diameter), with flat areas linked to deeply invaginated pits (Heuser and Anderson, 1989, Miller *et al*., 1991 and Rappoport *et al.,* 2004). Nevertheless, these large and sometimes seemingly static structures appear to be endocytically active, as clathrin punctae have been observed to separate from these structures (Gaidarov *et al.,* 1999; Blanpied *et al*., 2002; Rappoport *et al*., 2003, 2004; Merrifield *et al*., 2005; Yarar *et al*., 2005).

The existence of long-lived clathrin structures might reflect differences in the number and types of receptor-cargo interactions displayed by diverse cell types. The fact that mammalian cells have such large pits might reflect the need to internalize specialized materials absent in yeast and plants. Indeed, human LDL bound to its receptor has a diameter exceeding the capacity of a yeast or plant CCP (Perry and Gilbert 1979; Ehrlich *et al*., 2004). Consistent with this model, G protein-coupled receptors (GPCRs) and epidermal growth factor receptors (EGFRs) do not require de novo formation of CCPs for their internalization, but rather, are recruited to stable, pre-existing clathrin-coated structures (CCSs) (Santini *et al.,* 2002; Scott *et al*., 2002; Benesch *et al*., 2005). Moreover, for these events, CCP maturation is delayed until a

cargo threshold is satisfied (Cao *et al.,* 1998, Puri *et al.,* 2005; Tosoni *et al.,* 2005; Puthenveedu and von Zastrow, 2006; Henry *et al.,* 2012). Since pluripotent cells depend on sensing of extracellular cues for differentiation, the long-lived clathrin structures observed in H9.CLTA-RFP cells may reflect sites that are subject to cargo-dependent control of endocytosis, the degree of which may be lessened upon cellular differentiation.

Such cell-specific variation in CME might also reflect differences in the repertoire of endocytic proteins expressed by different cell types. Some components, such as clathrin, dynamin, and AP-2, appear to be part of a core machinery common to all cell types, as their loss results in embryonic lethality (Mitsunari *et al*., 2005; Ferguson *et al*., 2009; Chen *et al*., 2009). Other proteins appear to be cell-specific accessory proteins that are candidates to give rise to variation in CME (Mousavi *et al*., 2004). For example, adaptor proteins (e.g., autosomal recessive hypercholesterolaemia (ARH), disabled-2 (Dab-2), Numb, and β-arrestin) can provide cargo specificity (McMahon and Boucrot, 2011). Also, there appears to be variation in a role for actin in endocytosis. For example, in contrast to fibroblasts, neuronal terminals are insensitive to actin perturbation (Gad *et al.,* 1998; Merrifield *et al*., 2005; Yarar *et al.,* 2005). And even within the same cell, CME can show remarkably different properties. The apical surface of polarized epithelial cells is sensitive to actin drugs, while CME at the basolateral membrane is not (Boulant *et al*., 2011). Comprehensive genomic and proteomic analyses, comparing pluripotent cells with cells differentiated from hPSCs, coupled with live-cell study of endocytic dynamics, should provide information useful for elucidating the mechanisms that allow for modulation of endocytosis.

Why do long-lived clathrin structures reside in close proximity to sites of adhesion? Interestingly, larger long-lived clathrin structures have been documented only on the ventral (or adherent, coverslip proximal) surfaces of cells, suggesting that the underlying substrate may influence clathrin-mediated endocytic behavior. Indeed, recent studies examining the effect of cell-substrate adhesion on clathrin membrane dynamics have shown that clathrin lifetimes are extended and CME rates reduced in areas of increased membrane adhesion (Liu *et al*., 2009; Saffarian *et al*., 2009; Batchelder *et al*., 2010; Boulant *et al*., 2011). Moreover, blocking actin polymerization in these cells, with the actin monomer sequestering drug Latrunculin A, severely inhibited CCP endocytosis and preferentially increased CCP density at sites of substrate contact, indicating that actin assembly plays not only a role in efficient coated vesicle formation, but is preferentially required for CME in regions of membrane adhesion. Consistent with these observations, the Kirchhausen group demonstrated that local remodeling of actin filaments is essential for the formation, inward movement, and dissolution of large CCSs (Saffarian *et al*., 2009). CME has also been directly implicated in the turnover of integrins from focal adhesion complexes (Ezratty *et al*., 2006, 2009). Specifically, disassembly of membrane adhesions was dependent on clathrin-mediated endocytosis, in an ARH and Dab2 adaptor-dependent manner (Ezratty *et al*., 2009). Whether the long-lived CCSs of pluripotent cells are compositionally similar to the CCSs reported in somatic cells and whether they function to regulate pluripotent cell adhesion remains to be explored.

My goal in this study was to gain insight into if and how clathrin-mediated endocytosis, a complex pathway with far-reaching roles in cellular physiology, adapts to accommodate the fundamental needs of different cell types. My data show that endocytic dynamics can and do change upon cellular differentiation and implicate the actin-adhesion network in contributing towards this plasticity.

SUMMARY

Our understanding of cell behavior and physiology has been greatly advanced by the use of cell lines amenable to laboratory culture. Unfortunately, while their ability to readily propagate has made their use commonplace, cell lines have a physiology removed from that of normal cells.

Since the first description of 'coated pits' in 1964, there has been intense investigation using cell lines to understand the molecular machinery that underlies CME. Cellular, biochemical, and structural approaches have defined the molecular properties of clathrin and many of its associated proteins (Conner *et al.*, 2003; Fontin *et al.*, 2004; Merrifield *et al.*, 2005; Miwako and Schmid, 2006). But biochemical and structural approaches, however powerful, provide only snapshots or ensemble-averaged information about the properties of objects within a heterogeneous population; they are not sufficient to resolve highly transient steps in vesicle formation and uncoating. Fortunately, the advent of GFP and live-cell fluorescence microscopy has allowed for monitoring of dynamic cellular processes in real-time.

Live-cell imaging studies of clathrin-mediated endocytosis (CME) have revealed broad heterogeneity in the lifetimes, mobility, and size of clathrin-coated plasma membrane events among different cell lines (Gaidarov *et al.*, 1999; Merrifield *et al.*, 2002; Ehrlich *et al.*, 2004; Saffarian *et al.*, 2009). Why different cell lines exhibit varying dynamics and how this is achieved remain unknown.

Here, I employed zinc finger nuclease-mediated genome editing in human pluripotent stem cells (hPSCs) to monitor a key component of the endocytic machinery, clathrin light chain A. Using live-cell fluorescence microscopy, I found that hPSCs exhibit punctate but persistent CLTA-RFP membrane dynamics reminiscent of long-lived clathrin-coated structures or plaques. Strikingly, upon cellular differentiation, CLTA-RFP becomes highly dynamic, resembling canonical clathrin-coated pits. The persistent CLTA-RFP structures of hESCs co-localize to high degree with the cell adhesion protein paxillin, suggesting that components of the membrane adhesion complex and/or the actin network that it engages influence clathrin dynamics. I believe that continued study of endocytic protein dynamics in this system will allow us to gain new insights into the mechanisms and regulation of CME, reveal molecular regulators that govern cell fate decisions, and provide information crucial for the eventual development of stem cell-based therapies against diseases that result from endocytic defects.

MATERIALS AND METHODS

ZFN design, screening, and characterization. The ZFNs used in this study, targeting clathrin light chain A (CLTA) were previously described (Chapter 1; Doyon *et al*., 2011). In brief, ZFNs were designed to target +/- 50 bp of the stop codons of CLTA using an archive of pre-validated zinc finger modules (Isalan *et al*., 2001; Urnov *et al*., 2005; DeKelver *et al*., 2010). All ZFNs carried enhanced obligate heterodimer (eHF) alleles of the FokI endonuclease: Q486E/I499L/N496D and E490K/I538K/H537R (Doyon *et al*., 2011). ZFNs were prescreened for activity in K562 and SK-MEL-2 cells using Surveyor nuclease (Cel-1, Transgenomic, Omaha, NE) to detect indels (Urnov *et al*., 2005). Briefly, Accuprime Taq HiFi (Invitrogen, Carlsbad, CA) was used with the Cel-1 primers listed in Table 2.5 to amplify a short region surrounding the ZFN- target site in a 28-cycle PCR. Resulting amplicons were denatured, slowly re-annealed, and treated with Cel-1 for 20 min at 42°C, then separated on 10% criterion gels (Bio-Rad, Hercules, CA) and visualized by ethidium bromide staining.

Out-out PCR to detect targeted integration at CLTA locus. PCR was used to screen H9 hESC clones that were RFP-positive after FACS enrichment. For screening of positive clones, 100ng of genomic DNA prepared using the DNeasy Blood and Tissue Kit (Qiagen, Valencia, CA) was amplified in 30-cycle PCRs using Accuprime Taq HiFi (Invitrogen, Carlsbad, CA) with the TI primers listed in Table 2.5. An extension time of 10 min was used to minimize bias against the tagged allele(s) of the targeted gene. PCR products were analyzed on 5% criterion gels (Bio-Rad, Hercules, CA) that were run for 3-4 h at 150 V and visualized with ethidium bromide. Clones suitable for further analysis were identified by cloning the out-out PCR products into pCR2.1 TOPO (Invitrogen, Carlsbad, CA) and conventional sequencing.

Cell culture. H9 (WA-09) hESCs were purchased from WiCell Bank (Madison, WI). #38 hiPSC and WT-C hiPSC lines were kind gifts from the laboratories of D. Hockemeyer (UC Berkeley, CA) and B. Conklin (Gladstone Institute for Cardiovascular Disease, CA), respectively. Feeder-independent cell lines (H9 and WT-C) were maintained on dishes coated with Matrigel (BD Biosciences) in mTeSR1 media (Stem Cell Technologies, Vancouver, Canada). Feeder-dependent #38 hiPSCs were maintained on mitomycin C inactivated mouse embryonic fibroblast (MEF) feeder layers in hPSC medium [DMEM/F12 (Invitrogen, Carlsbad, CA) supplemented with 15% fetal bovine serum (FBS)(Hyclone, Logan, UT), 5% KnockOut^{TM} Serum Replacement (Invitrogen), 1 mM glutamine (Invitrogen), 1% nonessential amino acids (Invitrogen), 0.1 mM β-mercaptoethanol (Sigma) and 4 ng/ml FGF2 (R&D systems)]. hPSC cultures were passaged every 3 to 7 days either enzymatically with StemPro Accutase (Invitrogen), Dispase (Stem Cell Technologies; 1mg/ml), or collagenase type IV (Invitrogen; 1.5 mg/ml). SK-MEL-2 hCLTA^{EN} cells were derived as previously described (Doyon *et al*., 2011) and maintained in DMEM/F-12 + Glutamax (Invitrogen) supplemented with 10% FBS (HyClone). All cells were maintained under 5% CO_2 at 37°C.

Donor Design. Approximately 1.5 kb of genomic DNA sequence surrounding the human CLTA stop codon was amplified using the "HA" primers listed in Table 2.5 and cloned into pCR8-TOPO (Invitrogen, Carlsbad, CA). Next, a unique KpnI site was introduced via Quikchange (Agilent Technologies, Santa Clara, CA) site-directed mutagenesis with the "QC" primers. Finally, Tag-RFP-t (Shaner *et al.,* 2008) was amplified using the "KpnI" primers, which encode an N-terminal GTSGGS linker and cloned into the KpnI site of the CLTA homology arm constructs.

Generation of genome-edited cell lines. For H9 hESCs or WT-C hiPSCs, 2 μg of each ZFN encoding plasmid and 20 μg of donor plasmid were transfected into cells using a single cuvette Amaxa Nucleofector device (Lonza, Basal, Switzerland), as per the manufacturer's protocol. In brief, cells were harvested by Accutase treatment, and 1.5 – 2.0 x 10^6 cells were resuspended in Nucleofector Stem Cell Solution 1 and transfected using Nucleofector program A-023. Cells were returned to pre-coated matrigel dishes in mTESR1 supplemented with 10μM Rho-Kinase inhibitor (Y-27632; Calbiochem). #38 hiPSCs were cultured in 10μM Rho Kinase (ROCK)-inhibitor (Calbiochem; Y-27632) 24 hours prior to electroporation. Cell were harvested using 0.25% trypsin/EDTA solution (Invitrogen) and 1 x 10^7 cells resuspended in phosphate buffered saline (PBS) were electroporated with 40 μg of donor plasmid and 5 μg of each ZFN encoding plasmid (Gene Pulser Xcell System, Bio-Rad: 250 V, 500μ F, 0.4 cm cuvettes). Cells were subsequently plated on MEF feeder layers in hESC medium supplemented with ROCK-inhibitor (10μM) for the first 24 hours. Individual colonies were picked and expanded after puromycin selection (0.5 μg/ml) 10 to 14 days after electroporation. At 5- 7 days post transfection, cells were sorted for RFP-positive signals, using a DAKO-Cytomation MoFlo High Speed Sorter, directly into 96-well plates.

Total internal reflection fluorescence (TIRF) microscopy and live-cell imaging. Images were captured using Metamorph software on an Olympus IX-81 microscope using a 60x/NA1.49 objective and an ORCA-R2 camera (Hamamatsu, Japan). The system was maintained at 37°C using a WeatherStation chamber and temperature controller (PrecisionControl, Tacoma, WA). At 16-24 hours prior to imaging, cells were seeded onto Matrigel-coated glass coverslips in mTeSR1 (for hPSCs) or glass (for SK-MEL-2 hCLTA^{EN} cells). During imaging, cells were maintained in DMEM without phenol red that was supplemented with 5% FBS and 10 mM HEPES. A 488 nm solid-state laser (Melles Griot, Albuquerque, NM) and a 561 nm diode-pumped solid-state laser (Melles Griot, Albuquerque, NM) were used to excite GFP and RFP fluorophores, respectively. For matrigel experiments, matrigel was thawed and diluted as per manufacturer's protocol, dispensed directly onto plastic or glass coverslips at a concentration of 8.8 $\mu g/cm^2$, and incubated for 1hr at room temperature prior to immediate use (or stored at 4°C for future use). For lifetime analysis, images were acquired every 2 s, with an exposure time of 800 ms. Simultaneous two-color TIRF images were obtained using a DV2 image splitter (MAG Biosystems, Santa Fe, NM) to separate GFP and RFP emission signals.

Fibroblast differentiation of H9.CLTA-RFP hESCs
For embryoid-body (EB) induced differentiation, hESC colonies were harvested by 1mg/ml dispase (Stem Cell Technologies) as clumps and cultured for 7 days on low-attachment culture dishes (Corning) in mTESR1 for the first 2 days, before replacement of the media with DMEM supplemented with 15% fetal bovine serum, for the remaining 5 days. EBs were subsequently plated onto 0.1% gelatin-coated tissue culture dishes for propagation.

Immunofluorescence staining. Cells were grown on coverslips as for imaging, in 6-well plates overnight, before fixation in 4% PFA at room temperature for 20 min. After three washes with PBS, the coverslips were quenched with 1 mg/ml $NaBH_4$ for 15 min twice, and the cells were permeabilized in 0.1% saponin/PBS or 0.1% Triton X-100/PBS. After brief washing with PBS, the coverslips were incubated with mouse monoclonal anti-Oct3/4 antibody (Santa Cruz Biotechnology) or anti-paxillin antibody (BD Transduction Laboratories) overnight at 4ºC. The coverslips were then washed with PBS for 15 min before incubation with anti-mouse secondary antibody conjugated to Alexa Fluor 488 (A21202, Invitrogen) at 1:1000 dilution for 2 hr at room temperature. After three washes with PBS, the coverslips were mounted on glass slides using ProLong Gold + DAPI antifade reagent (Invitrogen, Carlsbad, CA).

Particle detection, tracking, and image analysis. Particle detection and tracking were performed using Imaris 7.1 software (Bitplane Scientific, Zurich, Switzerland). Prior to particle detection, images were first subjected to background subtraction. The Spots module of Imaris was then used to automatically detect point-like particles with an estimated spot diameter of 500 nm (~5 pixels). After automatic detection, detected spots were filtered based on satisfying minimum 'intensity standard deviation' and 'quality' control parameters. Only spots with values higher than the set threshold values were considered for analyses. Quality is defined as the intensity at the center of the spot, Gaussian filtered by ¾ of the spot radius. Appropriate threshold values were confirmed by visual inspection of correct particle detection. To trace objects through sequential frames of time data, a Brownian motion particle-tracking algorithm was applied. A maximum search distance of 350 nm was defined to disallow connections between a Spot and a candidate match if the distance between the predicted future position of the Spot and the candidate position exceeded the maximum distance. A gap-closing algorithm was also implemented to link track segment ends to track segment starts to recover tracks that were interrupted by the temporary disappearance of particles. The maximum permissible gap length was set equal to 7 frames. Track outputs were then visually inspected and, as necessary, edited to correct for tracking errors. Only punctae that appeared and disappeared during the lifetime of the acquisition and greater or equal to 6 seconds were subjected to lifetime analyses.

Statistical analysis. A non-parametric Mann-Whitney test was used to assess the significance for the effect of various parameters on the lifetime of CLTA-RFP at the

plasma membrane. All tests were performed and the data illustrated using Prism 5 (GraphPad Software, La Jolla, CA). Data are presented as mean ± S.D.

CHAPTER 5:
Conclusions and Future Directions

My dissertation focused on demonstrating the feasibility and utility of nuclease-mediated genome editing for studies of clathrin-mediated endocytosis. While the field of genome editing is still in its infancy, there have been significant advances in the technology that now make the design and assembly of the nucleases accessible to most laboratories. I believe this is a game changer, and I am excited and anxious to see how researchers will utilize genome modification to address once intractable biological questions.

The future of genome editing

Over just the last few years, new tools have been developed that add to the repertoire of nucleases that can mediate genome modification. Since the first description of zinc finger nucleases (ZFNs), and since our demonstration of the utility of ZFNs for study of protein dynamics, intense efforts have brought forth *Xanthamonas*-derived transcription activator-like effector nucleases (TALENs; Miller *et al*., 2011). I have successfully designed and assembled several TALEN pairs (n=5) for genome editing, and have achieved a 100% success rate in inducing both DNA cleavage and homology-directed repair (unpublished data). In the hands of an experienced researcher, a series of TALEN pairs can be designed, assembled, and tested for activity *in vivo* in just 7-10 days, at very low cost. This is a significant improvement over the time required to assemble and screen ZFNs. Overall, I consider TALENs to be as robust a tool as ZFNs, and believe their ease of engineering, in contrast to ZFNs, will allow for their more widespread use by the scientific community. In just the last few months, a bacterial-derived RNA-guided DNA endonuclease termed the CRISPR-Cas system was shown to stimulate similar genome alterations (Mali *et al*., 2013; Cong *et al.,* 2013*;* Jinek *et al.,* 2013). This system holds much promise as it utilizes Watson-Crick interactions to confer DNA binding specificity, which should allow for rapid synthesis of RNA guides. Currently, the activity of Cas/CRISPR complexes are overall low relative to TALENs and ZFNs, so continued improvements in the protein architecture and in the delivery of these reagents will be necessary before they are more generally adapted. Moreover, neither TALENs nor the Cas/CRISPR system has been validated for genome specificity to the same extent as ZFNs.

Novel strategies for probing endocytosis

In this dissertation, I used ZFNs to integrate fluorescent markers at specified genomic sites, with the aim of creating cells expressing endogenous levels of fluorescent protein fusions. It is worth noting, however, that this method of homology-directed repair need not be limited to integrations of fluorescent transgenes. Indeed, I have made efforts to develop a protein based mis-localization system to enable acute and inducible subcellular protein mis-localization in mammalian cells. Traditional methods for protein re-routing (and thereby inactivation) required that the endogenous protein be concurrently depleted while the protein fusions were ectopically overexpressed; an incomplete knockdown diminishes the effect of protein inactivation. Genome editing is an ideal tool to use for rapid inactivation of proteins because it enables one to fuse transgenes expressing mis-localization protein components (e.g.,

FKBP and FRB or CIBN and CRY2) to all alleles of the target gene, thereby allowing one to completely inactivate the target protein (Robinson *et al*., 2010; Idevall-Hagren *et al*., 2012). To date, we have successfully generated constructs bearing such fusions to an endocytic component, dynamin. For future studies, it is necessary to demonstrate the effectiveness of this strategy.

Actin in mammalian clathrin-mediated endocytosis

Our findings show that dynamin recruitment to endocytic sites is dependent on both actin and on the dynamin concentration. For future studies, it will be important to determine which additional factors contribute to dynamin recruitment prior to the formation of a constricted invagination and to precisely understand the mechanism(s) by which actin directs dynamin accumulation to the endocytic pit. It will also be important to correlate the observed patterns of protein recruitment to dynamic changes in CCS topology. Further, super-resolution microscopy methods that employ PALM, STORM, and related strategies should help resolve how actin and dynamin are distributed at various stages around the endocytic pit, and to provide insight into how these two machineries interact to drive coated-pit invagination and membrane scission. Since dynamin has been postulated to have two main functions in endocytosis, a regulatory GTPase role and a mechanoenzyme role, it will be important to unravel whether dynamin is localized to regions of the pit other than at the neck, as this will provide clues to the mechanism(s) underlying its functions. Xiaowei Zhuang's group recently achieved high spatiotemporal resolution (30nm x-y, 50nm z, 0.5s/frame) of budding clathrin events in real-time and directly visualized clathrin-coated membrane budding events (Jones *et al*., 2011). Extending this type of analysis to other components would be invaluable.

Clathrin-mediated endocytosis in different cell types

Analysis of cells expressing CLTA-RFP, in both undifferentiated and differentiated states, revealed that clathrin exists as long-lived membrane punctae in stem cells, the behavior of which can dramatically change upon differentiation. This observation indicates that endocytic behavior is capable of changing during differentiation, and that factor(s) (either intrinsic or extrinsic) contribute to this change. Over the course of my dissertation work, I was able to derive and validate several hESC and hiPSC lines. These lines are now ripe for investigation. I believe the two most interesting questions to probe are 1) what causes endocytic dynamics change, and 2) what is the physiological relevance of this change. To address the first question, I believe use of technologies that enable dissection of genomic and/or proteomic expression will be valuable to elucidate the contributing factors. By comparing expression patterns of undifferentiated and differentiated cells (of a specific cell type), one should be able to identify proteins or protein networks that influence endocytic dynamics. There is growing evidence that cargo type can influence the rate of CCP maturation. In line with the phrase 'you are what you eat', the stem cell system would be conducive to direct investigation of whether the repertoire of cargo internalized by endocytosis is modulated depending on cell type.

REFERENCES

Attree, O., Olivos, I.M., Okabe, I., Bailey, L.C., Nelson, D.L., Lewis, R.A., McInnes, R.R., and R.L. Nussbaum. 1992. The Lowe's oculocerebrorenal syndrome gene encodes a protein highly homologous to inositol polyphosphate-5-phosphatase. *Nature* 358(6383):239-42.

Baldassarre, M., Pompeo, A., Beznoussenko, G., Castaldi, C., Cortellino, S., McNiven, M.A., Luini, A., and R. Buccione. 2003. Dynamin participates in focal extracellular matrix degradation by invasive cells. *Molecular Biology of the Cell* 14:1074–1084.

Batchelder, E.M., and D. Yarar. 2010. Differential requirements for clathrin-dependent endocytosis at sites of cell-substrate adhesion. *Molecular Biology of the Cell* 21(17):3070-9.

Benesch, S., Polo, S., Lai, F.P., Anderson, K.I., Stradal, T.E.B., Wehland, J., and K. Rottner. 2005. N-WASP deficiency impairs EGF internalization and actin assembly at clathrin-coated pits. *Journal of Cell Science* 118(14):3103-3115.

Boll, W., Ohno, H., Songyang, Z., Rapoport, I., Cantley, L.C., Bonifacino, J.S., and T. Kirchhausen. 1996. Sequence requirements for the recognition of tyrosin-based endocytic signals by clathrin AP-2 complexes. *The EMBO Journal* 15(21):5789-95.

Boulant, S., Kural, C., Zeeh, J.C., Ubelmann, F., and T. Kirchhausen. 2011. Actin dynamics counteract membrane tension during clathrin-mediated endocytosis. *Nature Cell Biology* 13:1124-31.

Brodsky, F.M., Chen, C.Y., Knuehl, C., Towler, M.C. and D.E. Wakeham. 2001. Biological basket weaving: formation and function of clathrin-coated vesicles. *Annual Review of Cell and Developmental Biology* 17:517–568.

Cao, T.C., Mays, R.W., and M. von Zastrow. 1998. Regulated endocytosis of G protein-coupled receptors by a biochemically and functionally distinct subpopulation of clathrin-coated pits. *Journal of Biological Chemistry* 273:24592–24602.

Carroll, D. 2008. Progress and prospects: zinc-finger nucleases as gene therapy agents. *Gene Therapy* 15:1463–1468.

Chalfie, M., Tu, U., Euskirchen, G., Ward, W.W., and D.C. Prasher. 1994. Green fluorescent protein as a marker for gene expression. *Science* 263(5148):802-5.

Chen, H., Ko, G., Zatti, A., Di Giacomo, G., Liu, L., Raiteri, E., Perucco, E., Collesi, C., Min, W., Zeiss, C., De Camilli, P., and O. Cremona. 2009. Embryonic arrest at midgestation and disruption of Notch signaling produced by the absence of both epsin 1 and epsin 2 in mice. *PNAS USA* 106:13838–13843.

Clément, S., Krause, U., Desmedt, F., Tanti, J.F., Behrends, J., Pesesse, X., Sasaki, T., Penninger, J., Doherty, M., Malaisse, W., Dumont, J.E., Le Marchand-Brustel, Y., Erneux, C., Hue, L., and S. Schurmans. 2001. The lipid phosphatase SHIP2 controls insulin sensitivity. *Nature* 409(6816):92-7.

Cong, L., Ran, F.A., Cox, D., Lin, S., Barretto, R., Habib, N., Hsu, P.D., Wu, X., Jiang, W., Marraffini, L.A., and F. Zhang. 2013. Multiplex genome engineering using CRISPR/Cas systems. *Science* 339(6121):819-23.

Conner, S.D., and S.L. Schmid. 2002. Identification of an adaptor-associated kinase, AAK1, as a regulator of clathrin-mediated endocytosis. *Journal of Cell Biology* 156:921-929.

Conner, S.D., and S.L. Schmid. 2003. Regulated portals of entry into the cell. *Nature* 422:37-44.

Dalgliesh, G.L. *et al.* 2010. Systematic sequencing of renal carcinoma reveals inactivation of histone modifying genes. *Nature* 463:360-3.

DeKelver, R.C., Choi V.M., Moehle, E.A., Paschon, D.E., HOckemeyer, D., Meijsing, S.H. Sancak, Y., Cui, X., Steine, E.J., Miller, J.C., Tam, P., Bartsevich, V.V., Meng, X., Rupniewski, I., Gopalan, S.M., Sun, H.C., Pitz, K.J., Rock, J.M., Zhang, L., Davis, G.D., Rebar, E.J., Cheeseman I.M., Yamamoto, K.R., Sabatini, D.M., Jaenisch, R., Gregory, P.D., and F.D. Urnov. 2010. Functional genomics, proteomics, and regulatory DNA analysisin isogenic settings using zinc finger nuclease-driven transgenesis into a safe harbor locus in the human genome. *Genome Research* 20: 1133–1142.

Dhonukshe, P., Aniento, F., Hwang, I., Robinson, D.G., Mravec, J., Stierhof, Y.D., and J. Friml. 2007. Clathrin-mediated constitutive endocytosis of PIN auxin efflux carriers in Arabidopsis. *Current Biology* 17:520‑527.

Doyon, Y. McCammon, J.M., Miller, J.C., Faraji, F., Ngo, C., Katibah, G.E., Amora, R., Hocking, T.D., Zhang, L., Rebar, E.J., Gregory, P.D., Urnov, F.D., and S.L. Amacher. 2008. Heritable targeted gene disruption in zebrafish using designed zinc-finger nucleases. *Nature Biotechnology* 26:702–708.

Doyon, Y., Choi, V.M., Xia, D.F., Vo, T.D., Gregory P.D., and M.C. Holmes. 2010. Transient cold shock enhances zinc-finger nuclease-mediated gene disruption. *Nature Methods* 7:459–460.

Doyon, Y., Vo, T.D., Mendel, M.C., Greenberg, S.G., Wang, J., Xia, DF., Miller J.C., Urnov, F.D., Gregory, P.D., and M.C. Holmes. 2011. Enhancing zinc-finger-nuclease activity with improved obligate heterodimeric architectures. *Nature Methods* 8:74–79.

Doyon, J.B., Zeitler, B., Cheng, J., Cheng, A.T., Cherone, J.M., Santiago, Y., Lee, A.H., Vo, T.D., Doyon, Y., Miller, J.C., Paschon, D.E., Zhang, L., Rebar, E.J., Gregory, P.D., Urnov, F.D., and D.G. Drubin. 2011. Rapid and efficienc clathrin-mediated endocytosis revealed in genome-edited mammalian cells. *Nature Cell Biology* 13(3): 331-7.

Eden, E.R., Sun, X.M., Patel, D.D., and A.K. Soutar. 2007. Adaptor protein disabled-2 modulates low density lipoprotein receptor synthesis in fibroblasts from patients with autosomal recessive hypercholesterolaemia. *Human Molecular Genetics* 16:2751-2759.

Eden, E.R., Patel, D.D., Sun, X., Burden, J.J., Themis, M., Edwards, M., Lee, P., Neuwirth, C., Naoumova, R.P. and A.K. Soutar. 2002. Restoration of LDL receptor function in cells from patients with autosomal recessive hypercholesterolemia by retroviral expression of ARH1. *Journal of Clinical Investigation* 11:1695-1702.

Ehrlich, M., Boll, W., Van Oijen, A., Hariharan, R., Chandran, K., Nibert, M.L., and T. Kirchhausen. 2004. Endocytosis by random initiation and stabilization of clathrin-coated pits. *Cell* 118:591–605.

Engqvist-Goldstein, A.E., Zhang, C.X., Carreno, S., Barroso, C., Jeuser, J.E., and D.G. Drubin. 2004. RNAi-mediated Hip1R silencing results in stable association between the endocytic machinery and the actin assembly machinery. *Molecular Biology of the Cell* 15(4):1666-79.

Ezratty, E.J., Partridge, M.A., and G.G. Gundersen. 2005. Microtubule-induced focal adhesion disassembly is mediated by dynamin and focal adhesion kinase. *Nature Cell Biology* 7(6):581-90.

Ezratty, E.J., Bertaux, C., Marcantonio, E.E., and G.G. 2009. Gundersen. Clathrin mediates integrin endocytosis for focal adhesion disassembly in migrating cells. *Journal of Cell Biology* 187(5):733-47.

Ferguson, S.M., Raimondi, A., Paradise, S., Shen, H., Mesaki, K., Ferguson, A., Destaing, O., Ko, G., Takasaki, J., Cremona, O., O'Toole, E., and P. De Camilli. 2009. Coordinated actions of actin and BAR proteins upstream of dynamin at endocytic clathrin-coated pits. *Developmental Cell* 17:811-22.

Ferguson, S.M., and P. De Camilli. 2012. Dynamin, a membrane-remodelling GTPase. *Nature Review Molecular Cell Biology* 13(2):75-88.

Ford, M.G., Pearse, B.M., Higgins, M.K., Vallis, Y., Owen, D.J., Gibson, A., Hopkins, C.R., Evans, P.R., and H.T. McMahon. 2001. Simultaneous binding of PtdIns(4,5)P_2 and clathrin by AP180 in the nucleation of clathrin lattices on membranes. *Science* 291:1051-1055.

Ford, M.G., Mills, I.G., Peter, B.J., Vallis, Y., Praefcke, G.J.K., Evans, P.R. and H.T. McMahon. 2002. Curvature of clathrin-coated pits driven by epsin. *Nature* 419: 361-366.

Fotin, A., Cheng, Y., Sliz, P., Grigorieff, N., Harrison S.C., Kirchhausen, T., and T. Walz. 2004. Molecular model for a compete clathrin lattice from electron cryomicroscopy. *Nature* 432:573-9.

Fujimoto, L.M., Roth, R., Heuser, J.E., and S.L. Schmid. 2000. Actin assembly plays a variable, but not obligatory role in receptor-mediated endocytosis in mammalian cells. *Traffic* 1(2):161-71.

Gad, H., Low, P., Zotova, E., Brodin, L., and O. Shupliakov. 1998. Dissociation between Ca2+-triggered synaptic vesicle exocytosis and clathrin-mediated endocytosis at a central synapse. *Neuron* 21:607–616.

Gaidarov, I., Santini, F., Warren, R.A., and J.H. Keen. 1999. Spatial control of coated-pit dynamics in living cells. *Nature Cell Biology* 1:1–7.

Geurts, A.M. *et al*. 2009. Knockout rats via embryo microinjection of zinc-finger nucleases. *Science* 325:433.

Goldstein, J.L. and M.S. Brown. 1977. The low-density lipoprotein pathway and its relation to atherosclerosis. *Annual Review of Biochemistry* 46:897–930.

Gu, C., Yaddanapudi, S., Weins, A., Osborn, T., Reiser, J., Pollak, M., Hartwig, J., and S. Sever. 2010. Direct dynamin-actin interactions regulate the actin cytoskeleton. *EMBO Journal* 29(21):3593-606.

He, G., Gupta, P., Michaely, H., Hobbs, H., and J.C. Cohen. 2002. ARH is a modular adaptor protein that interacts with the LDL receptor, clathrin and AP-2. *Journal of Biological Chemistry* 277:44044-44049.

Henne, W.M., Boucrot, E., Meinecke, M., Evergren, E., Vallis, Y., Mittal, R., and H.T. McMahon. 2010. FCHO proteins are nucleators of clathrin ‐ mediated endocytosis. *Science* 328:1281‐1284.

Henry, A.G., Hislop, J.N., Grove, J., Thorn, K., Marsh, M., and M. von Zastrow. 2012. Regulation of endocytic clathrin dynamics by cargo ubiquitination. *Developmental Cell* 23(3):519-32.

Heuser, J.E. and R.G. Anderson. 1989. Hypertonic media inhibit receptor-mediated endocytosis by blocking clathrin-coated pit formation. *Journal of Cell Biology* 108(2):389-400.

Heuser, J. 1980. Three-dimensional visualization of coated vesicle formation in fibroblasts. *Journal of Cell Biology* 84(3):560-583.

Hinshaw, J.E. and S.L. Schmid. 1995. Dynamin self assembles into rings suggesting a mechanism for coated vesicle budding. *Nature* 374:190-192.

Hockemeyer, D., Soldner, F., Beard, C., Gao, Q., Mitalipova, M., DeKelver, R.C., Katibah, G.E., Amora, R., Boydston, E.A., Zeitler, B., Meng X., Miller J.C., Zhang, L., Rebar, E.J., Gregory, P.D., Urnov, F.D., and R. Jaenisch. 2009. Efficient targeting of expressed and silent genes in human ESCs and iPSCs using zinc-finger nucleases. *Nature Biotechnology* 27:851–857.

Huang, F., Khvorova, A., Marshall, W. and A. Sorkin. 2004. Analysis of clathrin-mediated endocytosis of epidermal growth factor receptor by RNA interference. *Journal of Biological Chemistry* 279:16657–16661.

Hughes, C.S., Postovit, L.M., and G.A. Lajoie. 2010. Matrigel: A complex protein mixture required for optimal growth of cell culture. *Proteomics* 10:1886-1890.

Idevall-Hagren O, Dickson EJ, Hille B, Toomre DK, De Camilli P. 2012. Optogenetic control of phosphoinositide metabolism. *PNAS USA* 109(35):E2316-23.

Isalan, M., Klug, A., and Y. Choo. 2001. A rapid, generally applicable method to engineer zinc fingers illustrated by targeting the HIV-1 promotor. *Nature Biotechnology* 19:656–660.

Inouye, S., and F.I. Tsuji. 1994. *Aequorea* green fluorescent protein: Expression of the gene and fluorescence characteristics of the recombinant protein. *FEBS Letters* 341:277-280.

Jensen, T.J., Loo, M.A., Pind, S., Williams, D.B., Goldberg, A.L., and J.R. Riordan. 1995. Multiple proteolytic systems, including the proteasome, contribute to CFTR processing. *Cell* 83:129–135.

Jinek, M., East, A., Cheng, A., Lin, S., Ma, E., and J. Doudna. 2013. RNA-programmed genome editing in human cells. *Elife* 2:e00471.

Jones SA, Shim SH, He J, Zhuang X. 2011. Fast, three-dimensional super-resolution imaging of live cells. *Nature Methods* 8(6):499-508.

Kaksonen, M., Sun, Y. and D.G. Drubin. 2003. A Pathway for Association of Receptors, Adaptors, and Actin during Endocytic Internalization. *Cell* 115(4):475-487.

Kaksonen, M., Toret, C.P. and D.G. Drubin. 2005. A modular design for the clathrin- and actin-mediated endocytosis machinery. *Cell* 123:305–320.

Kaksonen, M., Toret, C.P., and D.G. Drubin. 2006. Harnessing actin dynamics for clathrin-mediated endocytosis. *Nature Reviews Molecular Cell Biology* 7:404-414.

Kirchhausen, T. 2009. Imaging endocytic clathrin structures in living cells. *Trends in Cell Biology* 19:596–605.

Knoops, L., Hornakova, T., Royer, Y., Constantinescu, S. N. and J.C. Renauld. 2008. JAK kinases overexpression promotes in vitro cell transformation. *Oncogene* 27:1511–1519.

Koh, T.W., Verstreken, P., and H.J. Bellen. 2004. Dap160/intersectin acts as a stabilizing scaffold required for synaptic development and vesicle endocytosis. *Neuron* 43:193–205.

Krueger, E.W., Orth, J.D., Cao, H., and M.A. McNiven. 2003. A dynamin-cortactin-Arp2/3 complex mediates actin reorganization in growth factor-stimulated cells. *Molecular Biology of the Cell* 14:1085–1096.

Kukulski, W., Schorb, M., Welsch, S., Picco, A., Kaksonen, M., and J.A. Briggs. 2011. Correlated fluorescence and 3D electron microscopy with high sensitivity and spatial precision. *Journal of Cell Biology* 192(1):111-9.

Kukulski, W., Schorb, M., Kaksonen, M., and J.A. Briggs. 2012. Plasma membrane reshaping during endocytosis is revealed by time-resolved electron tomography. *Cell* 150(3):508-20.

Kuma, A., Matsui, M. and N. Mizushima. 2007. LC3, an autophagosome marker, can be incor- porated into protein aggregates independent of autophagy: caution in the interpretation of LC3 localization. *Autophagy* 3:323–328.

Lamaze, C., Fujimoto, L.M., Yin, H.L., and S.L. Schmid. 1997. The actin cytoskeleton is required for receptor-mediated endocytosis in mammalian cells. *Journal of Biological Chemistry* 272(33):20332-5.

Le Clainche, C., Pauly, B.S., Zhang C.X., Engqvist-Goldstein A.E., Cunningham K., and D.G. Drubin. 2007. A Hip1R-cortactin complex negatively regulates actin assembly associated with endocytosis. *EMBO Journal* 26:1199–1210.

Liu, A.P., Loerke, D., Schmid, S.L., and G. Danuser. 2009. Global and local regulation of clathrin-coated pit dynamics detected on patterned substrates. *Biophysical Journal* 97:103-47.

Liu, Y.W., Surka, M.C., Schroeter, T., Lukiyanchuk, V. and S.L. Schmid. 2008. Isoform and splice-variant specific functions of dynamin-2 revealed by analysis of conditional knock- out cells. *Molecular Biology of the Cell* 19:5347–5359.

Liu, Y.W., Mattila, J.P., and S.L. Schmid. 2013. Dynamin-catalyzed membrane fission requires coordinated GTP hydrolysis. *PLoS One* 8(1):e55691.

Loerke, D., Mettlen, M., Yarar, D., Jaqaman, K., Jaqaman, H., Danuser, G., and S.L. Schmid. 2009. Cargo and dynamin regulate clathrin-coated pit maturation. *PLoS Biology* 7:628–639.

Lombardo, A., Genovese. P., Beausejour, C.M., Colleoni, S., Lee, Y.L., Kim, K.A., Ando, D., Urnov, F.D., Galli, C., Gregory, P.D., Holmes, M.C., and L. Naldini. 2007.

Gene editing in human stem cells using zinc finger nucleases and integrase-defective lentiviral vector delivery. *Nature Biotechnology* 25:1298–1306.

Ludwig, T.E., Levenstein, M.E., Jones, J.M., Berggren, W.T., Mitchen, E.R., Frane, J.L., Crandall, L.J., Daigh, C.A., Conard, K.R., Piekarczyk, M.S., Llanas, R.A., and J.A. Thomson. 2006. Derivation of human embryonic stem cells in defined conditions. *Nature Biotechnology* 24(2):185-7.

Luo, T., Matsuo-Takasaki, M. and T.D Sargent. 2001. Distinct roles for Distal-less genes Dlx3 and Dlx5 in regulating ectodermal development in Xenopus. *Molecular Reproductive Development* 60:331–337.

Macia, E., Ehrlich, M., Massol, R., Boucrot, E., Brunner, C., and T. Kirchhausen. 2006. Dynasore, a cell-permeable inhibitor of dynamin. *Developmental Cell* 10(6):839-50.

Mali, P., Yang, L., Esvelt, K.M., Aach, J., Guell, M., DiCarlo, J.E., Norville, J.E., and G.M. Church. 2013. RNA-guided human genome engineering via Cas9. *Science* 339(6121):823-6.

McMahon, H.T., and E. Boucrot. 2011. Molecular mechanism and physiological functions of clathrin-mediated endocytosis. *Nature Reviews Molecular Cell Biology* 12(8):517-33.

Merrifield, C.J., Feldman, M.E., Wan, L. and W. Almers. 2002. Imaging actin and dynamin recruitment during invagination of single clathrin-coated pits. *Nature Cell Biology* 4:691– 698.

Merrifield, C.J., Qualmann, B., Kessels, M.M. and W. Almers. 2004. Neural Wiskott Aldrich Syndrome Protein (N-WASP) and the Arp2/3 complex are recruited to sites of clathrin-mediated endocytosis in cultured fibroblasts. *European Journal of Cell Biology* 83:13–18.

Merrifield, C.J., Perrais, D. and D. Zenisek. 2005. Coupling between clathrin-coated-pit invagination, cortactin recruitment and membrane scission observed in live cells. *Cell* 121:593–606.

Mettlen, M., Stoeber, M., Loerke, D., Antonescu, C.N., Danuser, G., and S.L. Schmid. 2009. Endocytic accessory proteins are functionally distinguished by their differential effects on the maturation of clathrin-coated pits. *Molecular Biology of the Cell*. 20:3251– 3260.

Mettlen, M., Pucadyil, T., Ramachandran, R. and S.L. Schmid. 2009. Dissecting dynamin's role in clathrin-mediated endocytosis. *Biochemical Society Trans*actions 37:1022–1026.

Mettlen, M., Loerke, D., Yarar, D., Danuser, G. and S.L. Schmid. 2010. Cargo and adaptor-specific mechanisms regulate clathrin-mediated endocytosis. *Journal of Cell Biology* 188:919–933.

Miller, K., Shipman, M., Trowbridge, I.S., and C.R. Hopkins. 1991. Transferrin receptors promote the formation of clathrin lattices. *Cell* 65:621–632.

Miller, J.C., Tan, S., Qiao, G., Barlow, K.A., Wang, J., Xia, D.F., Meng, X., Paschon, D.E., Leung, E., Hinkley, S.J., Dulay, G.P., Hua, K.L., Ankoudinova, I., Cost, G.J., Urnov, F.D., Zhang, H.S., Holmes, M.C., Zhang, L., Gregory, P.D., and E.J.

Rebar. 2011. A TALE nuclease architecture for efficient genome editing. *Nature Biotechnology* 29(2):143-8.

Mitsunari, T., Nakatsu, F., Shioda, N., Love, P.E., Grinberg, A., Bonifacino, J.S., and H. Ohno. 2005. Clathrin adaptor AP-2 is essential for early embryonal development. *Molecular Cell Biology* 25:9318–9323.

Miwako, I., and S.L. Schmid. 2006. A cell-free biochemical complementation assay reveals complex and redundant cytosolic requirements for LRP endocytosis. *Experimental Cell Research* 312(8):1335-44.

Miyama, K., Yamada, G., Yamamoto, T.S., Takagi, C., Miyado, K., Sakai, M., Ueno, N., and H. Shibuya. 1999. A BMP-inducible gene, dlx5, regulates osteoblast differentiation and mesoderm induction. *Developmental Biology* 208:123–133.

Moehle, E.A., Rock, J.M., Lee, Y.L., Jouvenot, Y., DeKelver, R.C., Gregory, P.D., Urnov, F.D., and M.C. Holmes. 2007. Targeted gene addition into a specified location in the human genome using designed zinc finger nucleases. *PNAS* 104:3055–3060.

Mooren, O.L., Kotova, T.I., Moore, A.J., and D.A. Schafer. 2009. Dynamin2 GTPase and cortactin remodel actin filaments. *Journal of Biological Chemistry* 284(36):23995-4005.

Mousavi, S.A., Malerod, L., Berg, T., and R. Kjeken. 2004. Clathrin-dependent endocytosis. *Biochemical Journal* 377:1–16.

Moradpour, D., Penin, F. and C.M. Rice. 2007. Replication of hepatitis C virus. *Nature Reviews Microbiology* 5:453–463.

Nunez, D., Antonescu, C., Mettlen, M., Liu, A., Schmid, S.L., Loerke, D., and G. Danuser. 2011. Hotspots organize clathrin-mediated endocytosis by efficient recruitment and retention of nucleating resources. *Traffic* 12(12):1868-78.

Orkin, R..W., Gehron, P., McGoodwin, E.B., Martin, G.R., Valentine, T., and R. Swarm. 1977. A murine tumor producing a matrix of basement membrane. *Journal of Experimental* Medicine 145:204-220.

Pennington, K., Beasley, C.L., Dicker, P., Fagan, A., English, J., Pariante, C.M., Wait, R., Dunn, M.J., and D.R. Cotter. 2008. Prominent synaptic and metabolic abnormalities revealed by proteomic analysis of the dorsolateral prefrontal cortex in schizophrenia and bipolar disorder. *Molecular Psychiatry* 13(12):1102-17.

Perrias, D., and C.J. Merrifield. 2005. Dynamics of Endocytic Vesicle Creation. *Developmental Cell* 9(5):581-592.

Perry, M.M. and A.B. Gilbert. 1979. Yolk transport in the ovarian follicle of the hen (Gallus domesticus): lipoprotein-like particles at the periphery of the oocyte in the rapid growth phase. *Journal of Cell Science* 39:257–272.

Pines, J. 1995. GFP in mammalian cells. *Trends in Genetics* 11(8)326-7.

Pucadyil, T.J. and S.L. Schmid. 2008. Real-time visualization of dynamin-catalyzed membrane fission and vesicle release. *Cell* 135:1263–1275.

Puri, C., Tosoni, D., Comai, R., Rabellino, A., Segat, D., Caneva, F., Luzzi, P., Di Fiore, P.P. and C. Tacchetti. 2005. Relationships between EGFR signaling-competent and endocytosis-competent membrane microdomains. *Molecular Biology of the Cell* 16:2704–2718.

Puthenveedu, M.A., and M. von Zastrow. 2006. Cargo regulates clathrin-coated pit dynamics. *Cell* 127(1):113-24.

Ramachandran, R., Surka, M., Chappie, J.S., Fowler, D.M., Foss, T.R., Song, B.D., and S.L. Schmid. 2007. The dynamin middle domain is critical for tetramerization and higher-order self-assembly. *EMBO Journal* 26(2):559-66.

Ramachandran, R., Pucadyil, T.J., Liu, Y.W., Acharya, S., Leonard, M., Lukiyanchuk, V., and S.L. Schmid. 2009. Membrane insertion of the pleckstrin homology domain variable loop 1 is critical for dynamin-catalyzed vesicle scission. *Molecular Biology of the Cell* 20(22):4630-9.

Rappoport, J.Z., Kemal, S., Benmerah, A. and S.M. Simon. 2006. Dynamics of clathrin and adaptor proteins during endocytosis. *American Journal of Physiology* 291:C1072–C1081.

Robinson MS, Sahlender DA, Foster SD. 2010. Rapid inactivation of proteins by rapamycin-induced rerouting to mitochondria. *Developmental Cell* 18(2):324-31.

Roth, T.F. and K.R. Porter. 1964. Yolk protein uptake in the oocyte of the mosquito *Aedes Aegypti*. *Journal of Cell Biology* 20:313–332.

Roux, A., Uyhazi, K., Frost, A. and P. De Camilli. 2006. GTP-dependent twisting of dynamin implicates constriction and tension in membrane fission. *Nature* 441:528–531.

Saffarian, S., Cocucci, E. and T. Kirchhausen. 2009. Distinct dynamics of endocytic clathrin-coated pits and coated plaques. *PLoS Biology* 7:e1000191.

Santini, F., Gaidarov, I., and J.H. Keen. 2002. G protein-coupled receptor/arrestin3 modulation of the endocytic machinery. *Journal of Cell Biology* 156:665-676.

Santolini, E., Puri, C., Salcini, A.E., Gagliani, M.C., Pelicii, PG., Tacchetti, C., and P.P. Di Fiore. 2000. Numb is an endocytic protein. *Journal of Cell Biology* 151:1345-1351.

Schlunck, G., Damke, H., Kiosses, W.B., Rusk, N., Symons, M.H., Waterman-Storer, C.M., Schmid, S.L., and M.A. Schwartz. 2004. Modulation of Rac localization and function by dynamin. *Molecular Biology of the Cell* 15:256–267.

Schmid, E.M., Ford, M.G., Burtey, A., Praefcke, G.J., Peak-Chew, S.Y., Mills, I.G., Benmerah, A., and H.T. McMahon. 2006. Role of the AP2 beta-appendage hub in recruiting partners for clathrin-coated vesicle assembly. *PLoS Biology* 4:e262.

Shnyrova, A.V., Bashkirov, P.V., Akimov, S.A., Pucadyil, T.J., Zimmerberg, J., Schmid, S.L., and V.A. Frolov. 2013. Geometric catalysis of membrane fission driven by flexible dynamin rings. *Science* 339(6126):1433-6.

Scott, M.G., Benmerah, A., Muntaner, O., and S. Marullo. 2002. Recruitment of activated G protein-coupled receptors to pre-existing clathrin-coated pits in living cells. *Journal of Biological Chemistry* 277(5):3552-9.

Sever, S., Muhlberg, A.B., and S.L. Schmid. 1999. Impairment of dynamin's GAP domain stimulates receptor-mediated endocytosis. *Nature* 398(6727):481-6.

Sever, S., Damke, H., and S.L. Schmid. 2000. Dynamin:GTP controls the formation of constricted coated pits, the rate limiting step in clathrin-mediated endocytosis. *Journal of Cell Biology* 150(5):1137-48.

Shaner, N.C., Lin, M.Z., McKeown, M.R., Steinbach, P.A., Hazelwood, K.L., Davidson, M.W., and R.Y. Tsien. 2008. Improving the photostability of bright monomeric orange and red fluorescent proteins. *Nature Methods* 5:545–551.

Shukla, V.K. *et al*. 2009. Precise genome modification in the crop species Zea mays using zinc-finger nucleases. *Nature* 459:437–441.

Smaczynska-de Rooij, I.I., Allwood, E.G., Aghamohammadzadeh, S., Hettema, E.H., Goldberg, M.W., and K.R. Ayscough. 2010. A role for the dynamin-like protein Vps1 during endocytosis in yeast. J. Cell Sci. 123, 3496–3506.

Soulet, F., Yarar, D., Leonard, M. and S.L. Schmid. 2005. SNX9 regulates dynamin assembly and is required for efficient clathrin-mediated endocytosis. *Molecular Biology of the Cell* 16:2058–2067.

Stearns, T. 1995. Green Fluorescent Protein: The green revolution. *Current Biology* 5(3):262-264.

Stimpson, H.E., Toret, C.P., Cheng, A.T., Pauly, B.S. and D.G. Drubin. 2009. Early-arriving Syp1p and Ede1p function in endocytic site placement and formation in budding yeast. *Molecular Biology of the Cell* 20:4640–4651.

Sweitzer, S., and J. Hinshaw. 1998. Dynamin undergoes a GTP-dependent conformational change causing vesiculation. *Cell* 93:1021-1029.

Takahashi, K., Tanabe, K., Ohnuki, M., Narita, M., Ichisaka, T., Tomoda, K., and S. Yamanaka. 2007. Induction of Pluripotent Stem Cells from Adult Human Fibroblasts by Defined Factors. *Cell* 131(5):861-872.

Takei, K., Slepnev, V.I., Haucke, V., and P. de Camilli. 1999. Functional partnership between amphiphysin and dynamin in clathrin-mediated endocytosis. *Nature Cell Biology* 1:33–39.

Taylor, M.J., Perrais, D., and C.J. Merrifield. 2011. A high precision survey of the molecular dynamics of mammalian clathrin-mediated endocytosis. *PLoS Biology* 9(3):e1000604.

Taylor, M.J., Lampe, M., and C.J. Merrifield. 2012. A feedback loop between dynamin and actin recruitment during clathrin-mediated endocytosis. *PLoS Biology* 10(4):e1001302.

Thomson, J.A., Itskovitz-Eldor, J., Shapiro, S.S., Waknitz, M.A., Swiergiel, J.J., Marshall, V.S., and J.M. Jones. 1998. Embryonic stem cell lines derived from human blastocysts. *Science* 282(5391):1145-1147.

Tosoni, D., Puri, C., Confalonieri, S., Salcini, A.E., De Camilli, P., Tacchetti, C., and P.P. Di Fiore. 2005. TTP specifically regulates the internalization of the transferrin receptor. *Cell* 123: 875–888.

Traub, L.M. 2009. Tickets to ride: selecting cargo for clathrin-regulated internalization. *Nature Review Molecular Cell Biology* 10:583–596.

Urnov, F.D., Miller, J.C., Lee, Y.L., Beausejour, C.M., Rock, J.M., Augustus, S., Jamieson, A.C., Porteus, M.H., Gregory, P.D., and M.C. Holmes. 2005. Highly efficient endogenous human gene correction using designed zinc-finger nucleases. *Nature* 435:646–651.

Urnov, F.D., Rebar, E.J., Holmes, M.C., Zhang, H.S. and P.D. Gregory. 2010. Genome editing with engineered zinc finger nucleases. *Nature Reviews Genetics* 11: 636–646.

Ward, C.L., Omura, S. and R.R. Kopito. 1995. Degradation of CFTR by the ubiquitin-proteasome pathway. *Cell* 83:121–127.

Wu, X., Zhao, X., Baylor, L., Kaushal, S., Eisenberg, E., and L.E. Greene. 2001. Clathrin exchange during clathrin-mediated endocytosis. *Journal of Cell Biology* 155:291–300.

Yarar, D., Waterman-Storer, C.M., and S.L. Schimd. 2005. A dynamic actin cytoskeleton functions at multiple stages of clathrin-mediated endocytosis. *Molecular Biology of the Cell* 16(2):964-75.

Yu, J., Vodyanik, M.A., Smuga-Otto, K., Antosiewicz-Bourget, J., Frane, J.L., Tian, S., Nie, J., Jonsdottir, G.A., Ruotti, V., Stewart, R., Slukvin. I.I., and J.A. Thomson. 2007. Induced pluripotent stem cell lines derived from human somatic cells. *Science* 318(5858):1917-20.

Zuchner, S., Noureddine, M., Kennerson, M., Verhoeven, K., Claeys, K., De Jonghe, P., Merory, J., Oliveira, S.A., Speer, M.C., Stenger, J.E., Walizada, G., Zhu, D., Pericak-Vance, M.A., Nicholson, G., Timmerman, V., and J.M. Vance. 2005. Mutations in the pleckstrin homology domain of dynamin 2 cause dominant intermediate Charcot-Marie-Tooth disease. *Nature Genetics* 37: 289–294.